

**Survey of creep properties of
copper intended for nuclear
waste disposal**

Henrik C M Andersson-Östling
Swerea KIMAB

Rolf Sandström
Materials Science and Engineering, KTH

December 2009

Svensk Kärnbränslehantering AB

Swedish Nuclear Fuel
and Waste Management Co

Box 250, SE-101 24 Stockholm
Phone +46 8 459 84 00



Survey of creep properties of copper intended for nuclear waste disposal

Henrik C M Andersson-Östling
Swerea KIMAB

Rolf Sandström
Materials Science and Engineering, KTH

December 2009

This report concerns a study which was conducted for SKB. The conclusions and viewpoints presented in the report are those of the authors. SKB may draw modified conclusions, based on additional literature sources and/or expert opinions.

A pdf version of this document can be downloaded from www.skb.se.

Abstract

Creep in copper for application in canisters for nuclear waste disposal is surveyed. The importance of phosphorus doping to obtain adequate properties is demonstrated experimentally as well as explained theoretically. Creep tests results for electron beam and friction stir welds are compared. The latter type of welds has properties that are close to those of parent metal. The relation between slow strain rate tensile and creep is described. Fundamental constitutive equations are presented that are suitable for finite element modelling. These equations are used to simulate creep deformation in canisters.

Contents

1	Background	7
2	Research at KIMAB and KTH	9
2.1	How it started	9
2.2	Timeline of research	9
3	Creep testing techniques	11
3.1	Materials sampling	11
3.2	Test procedures	11
3.3	Testing – plastic strain on loading	14
3.4	Testing – resets	15
3.5	Testing – geometrical considerations	15
3.6	Temperature	15
4	Creep of oxygen free high conductivity copper	17
5	Creep of phosphorus doped copper, Cu-OFP	21
5.1	High temperature testing	21
5.2	Influence of grain size, sulphur and phosphorus content	25
5.3	Creep testing at low stresses	27
5.4	Electron beam and friction stir welds	27
5.5	Weld reduction factors	30
6	Influence of cold work on creep	33
6.1	Background	33
6.2	Creep tests	33
6.3	Effect of indentations	34
7	Slow strain rate tensile tests	37
8	Modelling of creep ductility	41
8.1	Experimental background	41
8.2	Cavity nucleation	41
8.3	Cavity growth	42
8.4	Rupture predictions	43
9	Creep equations	47
9.1	Stationary state, Cu-OF	47
9.2	Stationary state, Cu-OFP	48
9.3	Primary creep, empirical model	50
9.4	Primary creep, fundamental model	53
9.5	Uncertainties in the constitutive equation for creep strain in Cu-OFP	56
9.5.1	Background	56
9.5.2	Variation of parameters in the model	56
9.5.3	Parameters in the model for secondary creep	57
9.5.4	Primary creep	58
9.5.5	Agglomerated effect	59
10	Constitutive equations	61
10.1	Background	61
10.2	Multiaxial models	61
10.2.1	Approach A	61
10.2.2	Approach B	62
10.3	Notched specimens	63
11	Creep deformation in canister	65
11.1	Modelling parameters	65
11.2	Deformations in the canister	66
11.3	Stresses and strains in slits and their role in copper canister integrity	69
11.4	Effects of uneven swelling pressure on the canister	73

12	Conclusions	77
13	Acknowledgements	79
14	Tables	81
15	References	93

1 Background

Copper is a most interesting metal. It is one of the earliest known to man, and also one of the most used. The first known use of copper is as material for weapons. Copper weapons were found to be more durable than edged stone weapons and also possible to resharpen when dulled by use. Body armour could also be made from copper and in both of these uses the ductility of pure copper was the key property. Later copper was used to make among other things nails for shipbuilding, cooking pots and personal jewellery. The properties used here were in addition to the ductility, the toughness, the high thermal conductivity and the ability to be polished to a high sheen. Today the most important use for copper is in electrical appliances where the high electrical conductivity is the main material property.

An early use for copper was also as a protective sheeting material for ship hulls. Initially the use was to stop the growth of seaweeds and other biomaterial by using the slight biotoxic nature of copper. However, it was noted that the copper also resisted corrosion to a great extent. A good quality copper sheeted hull could remain intact for several decades. Copper is a relatively inert metal in most environments and more specifically in water. Only if the water is fast flowing, the corrosion process is accelerated. The good properties in water, make it an ideal material to make corrosion protective containers from.

Copper has since the beginning of modern science been used as a model material for experiments. One of the properties studied was creep of metals and much of the early knowledge of dislocation movements and grain boundary sliding comes from studies of copper specimens /1/. These early studies of copper creep behaviour were incorporated in the deformation map published by Frost and Ashby /2/ in 1983.

The operation of nuclear power plants produces radioactive waste that has to be treated and disposed in such a way that it does not harm the environment. Spent nuclear fuel remains highly radioactive for more than 100,000 years. A safe way must be found to dispose of this waste and the planned method in Sweden is the so-called KBS-3 concept, where the spent nuclear fuel is placed in canisters, Figure 1-1, that are deposited at 400 to 700 m down in the bedrock, Figure 1-2.

The canisters have an inner load carrying insert made in nodular cast iron with quadratic channels where the nuclear fuel elements are placed. The cast iron inserts are then placed inside thick walled, 50 mm, copper shells that are sealed by welding. Copper is chosen because it is immune against corrosion under reducing conditions in the bedrock and also because of its high ductility. The waste packages are placed in drilled holes in the bedrock and are embedded by a bentonite clay buffer. The surrounding ground water



Figure 1-1. Nuclear waste disposal canisters of the Swedish design. (SKB).

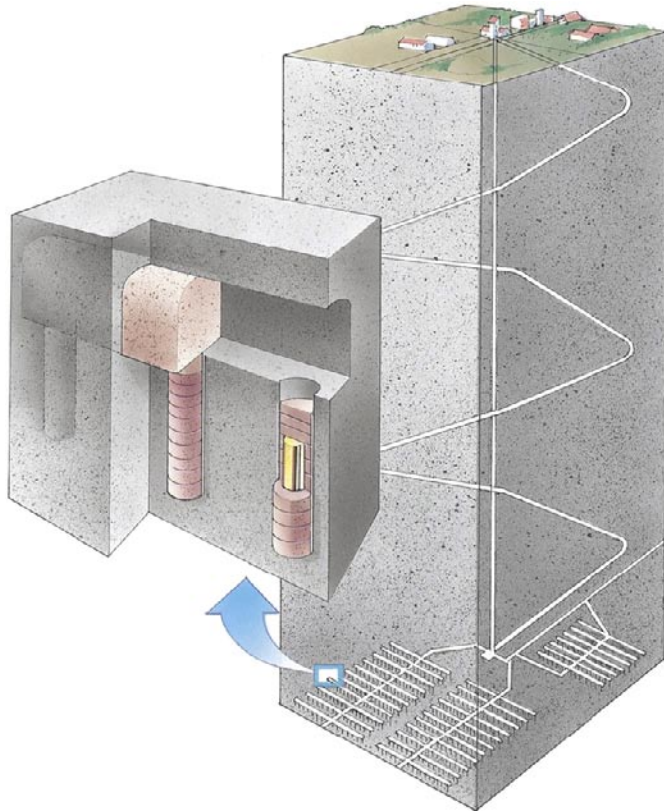


Figure 1-2. *The Swedish proposed method of canister repository. (SKB).*

will seep into the buffer over a period of many years, the bentonite will swell and increase the hydrostatic pressure. Due to this pressure the canister will plastically deform by creep. The deformation will continue until the existing gap between the copper shell and the cast iron insert is closed. The purpose of the present paper is to survey creep studies of copper related to nuclear waste disposal.

2 Research at KIMAB and KTH

2.1 How it started

Research in Sweden on the waste package for used nuclear fuel started in the mid 1970'ties. It was soon decided that a package with an outer shell of copper should be the main option. The reason was that safe corrosion properties could be anticipated due to the thermodynamic stability of copper in the repository. Creep properties of copper were not an issue initially. It was not until the public enquiry about the disposal concept in 1983 that the first discussions about creep took place. Such a public enquiry has taken place every third year since then.

During the 1970'ties it had been discovered that failures in structures and plants exposed to creep mainly take place in weldments. During this period a vast number of creep cracks and failures were observed in fossil fired power plants. There are three reasons for this. First the creep properties vary across the welds, since the weld metal, the heat affected zone, and the parent metal almost invariably have different creep properties and this gives rise to stress concentrations. Second, the creep ductility and strength are often lower for welds than for parent material. Third, the creep properties were rarely taken into account in design in those days.

In the beginning of 1980'ties, the Swedish Institute for Metals Research (now Swerea KIMAB) was together with British CEBG the internationally leading organisations in the study of creep in weldments. Tests were performed on uniaxial specimens as well as tubes under internal pressure. The experiments were successfully combined with FEM-modelling /3/. It was therefore proposed to SKB to study weldments in the copper canisters. Pure copper had been used extensively as a model material for creep studies on materials aspects as well as on design. Although most of these investigations were at temperatures of 300°C and above and thus well outside typical design temperatures for copper, no one anticipated the serious problem with the extremely low creep ductility that would appear later.

2.2 Timeline of research

A timeline for work on creep in copper at Swerea KIMAB and KTH is presented in Table 2-1. Work on creep in copper at Swerea KIMAB started in 1984 with a literature study /4/. This was followed in 1988 by a pilot creep study on a standard high purity copper material Cu-OF /5–7/. In 1992 a creep program was started on phosphorus doped copper Cu-OFP /8, 9/. Further studies on the same material were reported in 1995 when creep crack propagation studies, tensile tests and the effect of specimen size on the creep results were included. The first extrapolation efforts were also reported this year /10–13/. In 1996 further work on creep in Cu-OFP was presented /14, 15/. In 1998 a thorough analysis of creep ductility results on Cu-OF was published /16/. In 1999 the first slow rate tensile tests were performed at KTH for cold worked Cu-OFP /17/.

At the same time the optimal composition had been decided and a new programme was initiated that creep tested extruded bars with different phosphorus and sulphur levels as well as grain sizes /18, 19/. A new method for extrapolation of creep strain data was developed /20/. From 2004 the focus of the creep tests has been on welds. Both electron beam (EBW) and friction stir welds (FSW) were studied /21, 22/. New creep crack propagation tests were also performed at this time /23/. The work progressed and new results were published in 2007 /24, 25/.

Chemical composition and as received conditions for most of the above studies are given in Table 14-1 and Table 14-2 at the end of the report.

Cu-OF has consistently shown lower creep ductility than phosphorus doped Cu-OFP. In 2007 an explanation of this effect based on models for creep cavity nucleation and growth was presented /26/. Phosphorus has also a strong effect on the creep strength. The origin of the effect was analysed /27/. Fundamental models for the creep rate have been published recently /28, 29/. These constitutive equations have been applied to simulate the creep deformation in copper canisters. First only secondary creep was taken into account /30/. Later primary creep has also been considered /31, 32/. Slow strain rate test for annealed Cu-OFP were carried out. A fundamental model for these and other related flow curves has been successfully developed /33/. Experiments on the effect of cold deformation have been performed in 2009 /34, 35/. Furthermore, investigations on multiaxial stress state creep and creep crack growth on extruded material are ongoing /36/.

Table 2-1. A timeline of work on creep in copper for nuclear waste disposal at Swerea KIMAB and KTH.

1984 Literature survey
1988 Creep study of Cu-OF at 75 to 145°C
1992 Creep study of Cu-OF at 180 to 250°C
1992 Creep study of Cu-OFP at 200 to 350°C
1995 Creep study of Cu-OFP at high temperatures
1995 Initial creep crack growth studies
1995 Specimen size studies
1996 Creep test series 600, 700 and 800
1999 Extruded copper studies at 175°C. <i>P</i> , <i>S</i> and grain size effect
1999 Extrapolation of creep strain data
1999 Hot working investigations
1999 Slow strain rate tensile tests of cold work material
2001 FSW tool material development literature survey
2004 Initial weld studies, EBW and FSW
2005 Second creep crack growth investigation
2005 Creep loading procedure studies
2007 Creep investigations on extruded material welds
2007 Modelling of creep ductility on the basis of creep cavity nucleation and growth
2007 Modelling the effect of phosphorus on copper creep
2007 Fundamental constitutive equations for creep during power-law breakdown
2007 Slow strain rate tensile tests of annealed copper
2007 FEM-modelling of creep in copper canisters taking secondary creep into account
2008 Effect of hydrogen in Cu
2008 Fundamental model for slow strain rate flow curves
2008 FEM-modelling of creep in copper canisters taking primary creep into account
2009 The effect of cold deformation on creep in copper
2009 Extremely slow creep loading of copper
2009 Studies on the role of multiaxial stress state during creep
2009 Third creep crack growth studies

3 Creep testing techniques

3.1 Materials sampling

All materials to be creep tested have to be extracted from the larger delivered pieces. Uniaxial creep tests are performed with plain cylindrical tests specimens. The smaller specimen has a gauge length of 50 mm and a gauge diameter of 5 mm, the larger specimen a gauge length of 75 mm and a gauge diameter of 10 mm, Figure 3-1.

To be able to manufacture specimens the blanks cut from the copper pieces have to be bigger than the final dimensions of the specimens, 9×9×90 mm and 17×17×180 mm, respectively.

The placement of the specimens is important. If the material has a texture due to rolling or extrusion, specimens are usually taken along the working direction. If the material contains a weld, specimens can be taken from either the weld metal, the base metal, the heat affected zone (HAZ), or in a cross-weld position. An example of the extraction of specimens from a weld is shown in Figure 3-2.

Specimens from either the weld constituents or the base metal give information on the properties of homogenous material. Cross weld specimens tend to accentuate the part of the weld that is weakest. They cannot be used for ductility estimation since the gauge length is undetermined if only a part of the specimen is straining during testing.

3.2 Test procedures

All creep tests performed up to 2008 were conducted on standard dead weight, lever creep test rigs. All test rigs work in a similar manner even if the individual design varies. A schematic drawing of the principle is given in Figure 3-3. Swerea KIMAB has over 70 of these test rigs of different configurations all equipped with high temperature furnaces, Figure 3-4.

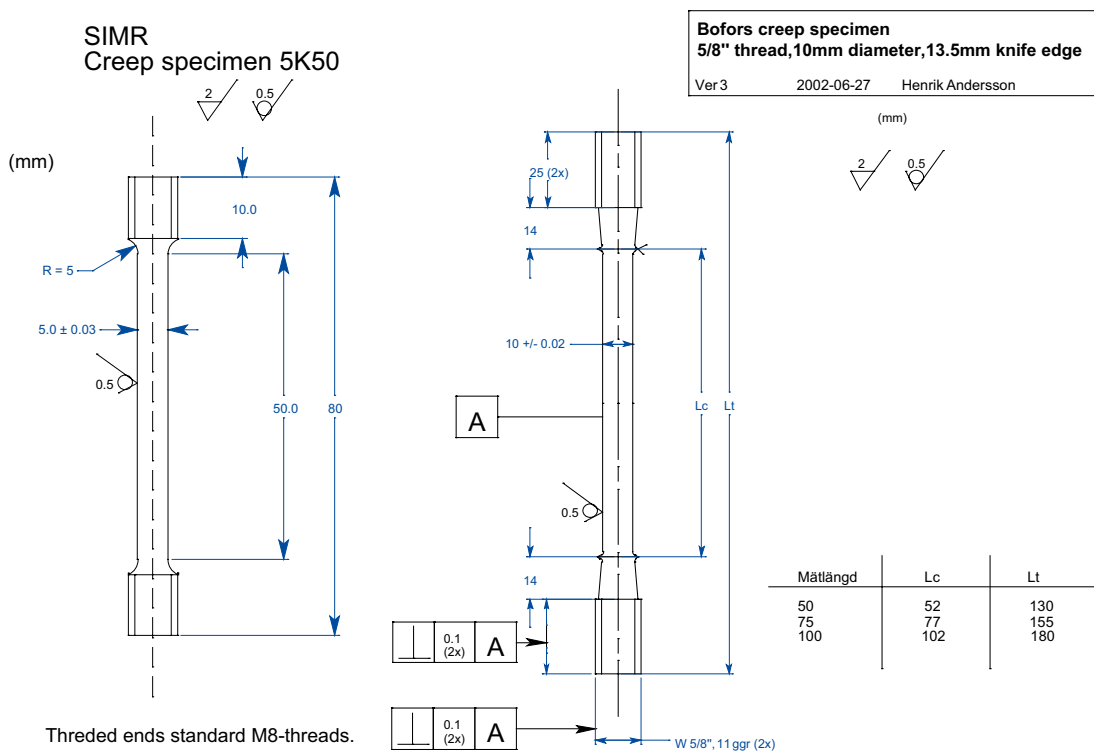


Figure 3-1. a) Creep specimen type 5K50. The same specimen design is used in a similar specimen called 5K25 where the gauge length is 25 mm. b) Creep specimen type Bofors. The same design is used with gauge lengths from 50 to 100 mm by altering the distance between the knife edges.

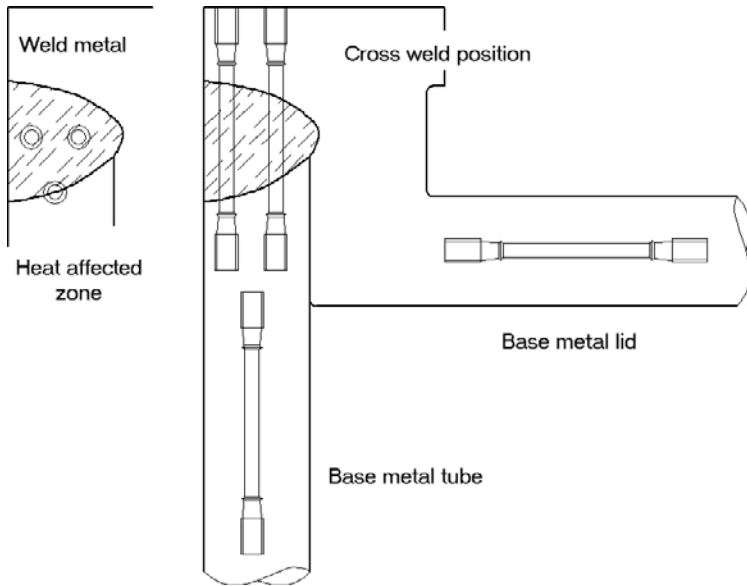


Figure 3-2. An example of the extraction of specimens from a friction stir weld. Specimens from the base metal lid and tube as well as the cross-weld, weld metal and heat affected zone specimens are marked in the image. Taken from the 2007 study of friction stir welds at 75°C /24/.

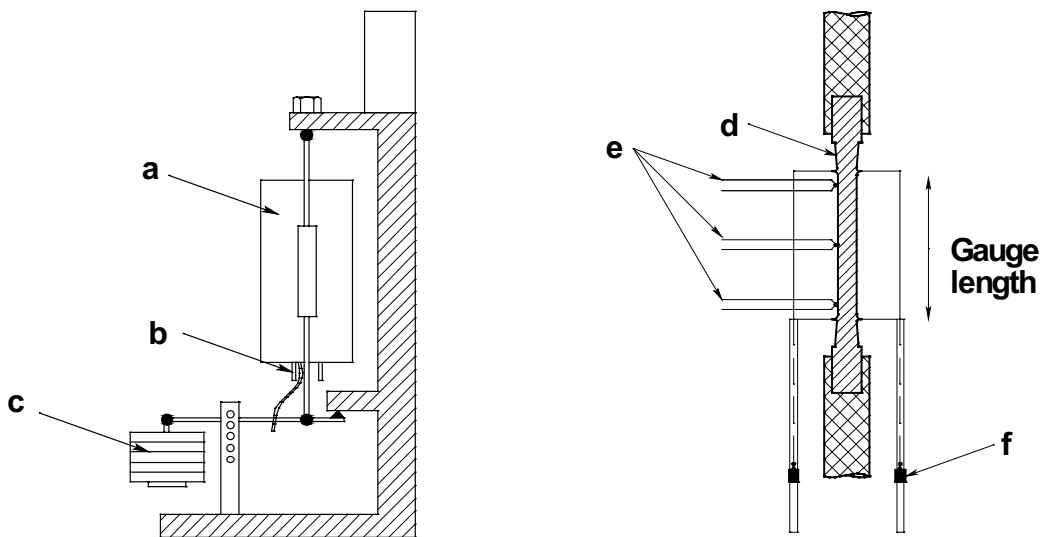


Figure 3-3. The principle of creep testing. At the left is a schematic drawing of a creep test rig, and on the right a creep specimen. a: furnace with specimen, b: extensometer transducer, c: weights and lever arm, d: specimen, e: thermocouples, f: transducer. The gauge length is marked in the right image.



Figure 3-4. The creep laboratory with creep rigs visible. Insert: a close-up on the lever arm.

The set-up of a creep test is as follows. The load train is calibrated by placing a calibrated load cell in the test rig instead of the specimen. Lever arms have a ratio of 1:16, 1:20 or 1:25 but by using the actual lever arm and load with actual weights until the correct reading is reached on the load cell, an individually correct load is obtained for each test. The weights are then removed until later. The specimen is placed inside the furnace and preloaded with the empty lever arm, yielding a load of approximately 100 N. Thermocouples are tied to the gauge length and the specimen is heated to test temperature.

The thermocouples, known as type S (Pt/PtRd wires) are made from certified metals and new metal is used for the thermal junction for each new test. After a soaking time of at least 2 h during which the temperature gradient is adjusted and minimised, the previously calibrated weights are loaded onto the lever arm and the test started. The maximum tolerances allowed are $\pm 1^\circ\text{C}$ for temperature stability and $\pm 2^\circ\text{C}$ axial gradient. The load is, for all tests up to 2006, applied within 2 minutes.

If the creep strain in the specimen is sufficiently large, the lever arm must be reset to ensure that it has an approximately horizontal position. During the reset the specimen is temporarily unloaded by insertion of a manual lever arm between the fulcrum and the weights. The weights are lifted and the nut on the top of the load train adjusted until the angle of the lever arm again is $+ 5^\circ$. The weights are lowered and the load slowly reapplied to the specimen. The specimen temperature is not changed during this operation.

Strain and temperature are logged automatically using extensometers mounted on the knife edges just outside the gauge length on the specimens, Figure 3-3. In the case of the small specimen, Figure 3-1, the knife edges are mounted on the adapters in which the specimens are mounted. The extensometer rods are fed to capacitive transducers that measure the strain in the specimen. Usually two transducers are used for each test. The signals from the transducers are logged along with the specimen temperature and the ambient temperature by a computerized logging system. The logging interval can be individually adjusted. The standard interval is 1 hour. As a backup system the measurements are noted on paper protocols once every workday.

The main attractive feature of capacitive transducers is their inherent ability to avoid the signal to drift from the correct measurement. The signal only depends on the dielectric properties of the medium between the electrodes, in the current application laboratory air.

The creep laboratory is climate controlled and kept at a constant temperature and humidity, meaning that the signals from the transducers are also constant apart from strain measurement. They are also linear and the accuracy is in theory 10 nm, but 100 nm is the practical limit. If a mechanical malfunction occurs it usually only affects one of the two transducers which can be removed and repaired while the test is monitored by the other transducer.

One drawback of the dead weight lever creep testing is that it is not compensated for the lever arm movement. The horizontal distance between the fulcrum and the load application point depends on the angle of the arm. This error can with confidence be neglected for small angle shifts and the used testing machines allow $\max \pm 5^\circ$ arm travel. The standard procedure is thus to start the test with the arm at the top limit and to reset the arm as the angle reaches the bottom limit. In practice this means a maximum travel of 5 mm at the specimen end of the lever. Depending on gauge length the test has to be reset every 5 or 10% engineering strain. In 2007 newly developed test machines were put into operation where the load is applied using a step motor connected to a gearbox. The equipment allows for 35 mm travel of the load arm without the need for unloading of the specimen. The load can also be applied very slowly. In the repository, the load is applied over a period of many years, and the testing performed in the new test rigs is aimed at emulating this slow loading process.

3.3 Testing – plastic strain on loading

A creep experiment is started by placing the specimen in the furnace and heating it to the test temperature. The load is then applied as smoothly as possible until the desired stress has been reached on the specimen. During the loading process the specimen is strained by the load. This is not really true creep strain since the timescale is several minutes rather than hundreds of hours. Early experiments did not distinguish between this plastic strain and the subsequent creep strain. Most testing at the creep laboratories up to this point had been made on ferritic steels where the initial strain is low, typically below 2%. In the case of copper, and especially annealed copper, the initial plastic strain can be as much as 15%, and thus a substantial part of the total strain. Later experiments recorded the initial strain but it was not included in the reported creep strain. This means that early and late creep results are not fully comparable, and the later results from 1999 and forward are conservative with respect to ductility.

In the repository, the canister is exposed to a hydrostatic pressure from the ground water. At a depth of 500 m the hydrostatic pressure is 5 MPa. In addition there is a swelling pressure from the bentonite. When it is fully soaked with water, the pressure is 5 to 13 MPa. Thus, the total pressure on the canister can reach 10 to 18 MPa. Depending on the hydraulic conductivity of rock and the associated rate of the water inflow, it can take up to one hundred years before the bentonite is fully soaked.

During the loading phase the stresses in the canisters will be so low that the secondary creep rate is negligible. Not until a pressure of about 15 MPa has been reached, the secondary creep is of importance. However, the strain on loading and the primary creep can still be significant. Tests are presently carried out to study the creep deformation during gradual increase of the load.

3.4 Testing – resets

Nearly all of the test rigs that have been used for creep testing of copper work according to the dead weight lever principle. Standard practice is to keep the arm $\pm 5^\circ$ from the horizontal. As a result of this allows a maximum amount of strain before the lever arm has to be raised to keep it off the floor. The strain can be either 5% or 10% depending on test rig. Since the total strain in many copper creep tests is 40% or more, the lever arm has to be reset several times. Some tests have been reset as many as five times. Annealed or close to annealed copper exhibits a creep tests curve that consists of almost exclusively primary and tertiary creep with almost no steady state secondary creep in between. The behaviour during a reset is that if the material is in a primary or early tertiary stage, new primary creep is initiated. This shows up as a series of bumps on the creep curves. A probable cause for this phenomenon is that during the reset the specimen is temporarily unloaded, and the dislocation substructure is relaxed. When the load is then reapplied a new dislocation substructure is created, yielding a new primary stress redistribution stage. If the specimen is reset well into the tertiary stage an accelerated tertiary stage is developed and the specimen rupture is accelerated.

Since so many of the tests have been reset several times it is imperative to know the effect of the unloading/reloading on the creep properties. It can be argued that the continuous unloading/reloading introduces a hot deformation into the specimen and the creep life is increased. But it could just as easily be argued that the unloading/reloading shortens the creep life by fatigue action on the specimen. In both cases modelling of the creep behaviour is made more difficult by this. For instance it is not clear as to which curve a model should be applied. The unbumped one that is not complete, or the envelope of the bumped curve. In the not yet completed study on extremely slow creep loading the newly developed test rigs does not need to be reset. Creep tests can thus be allowed to continue uninterrupted to rupture even if the creep strain approaches 100%. Modelling of the results and extrapolations of the results should be made easier by this approach. As a general recommendation the number of resets should always be kept to a minimum.

3.5 Testing – geometrical considerations

Creep testing of copper has been performed using two different types of specimens. The early experiments concentrated on the 5 mm diameter specimen shown in Figure 3-1. The gauge length has varied but usually a gauge length of 50 mm was used. Later experiments had predominately used standard Bofors 10 mm diameter specimens with a gauge length of 50 to 80 mm. The difference between these two specimen designs is in the manufacturing of the specimens. When a slender 5 mm specimen is turned on the lathe, work hardening can result from the vibration of the specimen when the cutting tool is applied to the surface. The 10 mm specimens are much bulkier and resistant to vibration. The end result is that the 5 mm specimens are slightly cold worked and exhibits a longer creep life than 10 mm specimens even if they are made from the same block of material. This was shown by a series of experiments in /12/. When the 5 mm specimens were annealed for 5 minutes at 600°C followed by a water quench, the creep results became similar to the 10 mm specimens. The 10 mm specimens were tested as-machined. The recommendation for future testing is to use 10 mm specimens when possible and to anneal all 5 mm specimens before testing.

3.6 Temperature

In the creep testing performed at the institute test temperatures in the copper creep tests have varied from a maximum of 600°C to a minimum of 75°C. In the real repository the temperature may be as high as 125°C in the cast insert and about 100°C in the copper shells for the initial years and then slowly decrease to room temperature over many hundred of years. It is therefore interesting to creep

test copper at the temperatures that is relevant to the repository. Copper is known to creep at room temperature and above, but for practical reasons test times must be kept to a reasonable length and the creep test has to be accelerated. There is two possible ways to accelerate a test, increase temperature or increase applied load. Both have been used in the investigations referred in this work. The earlier testing concentrated on increasing temperature to 175–250°C. This produced creep lives that could be fitted into the project timeframe. When the temperature is increased above the intended service temperature there is always a risk of having the test results exhibiting a creep damage accumulation behaviour that is different from the one at service temperatures. Partly for this reason the later work moved towards temperatures around 75°C that is a reasonable average of the temperature of the copper over the first years in the repository.

The resulting creep strain curves and the creep ductility at rupture were similar for the test series at higher and the lower temperatures. This does not apply to the Norton exponent, which is the slope of the strain rate versus stress curve. As the temperature decreases the Norton exponent rises, which is referred to as power-law breakdown. Physically this means that dislocation glide controls the creep rate, rather than climb. It also means that extrapolation to longer creep times is more difficult. A slope of 3–5 that is typical in power-law creep makes it easier to extrapolate data to longer times than a slope of 50 or 70. A small mistake or scatter in the results gives a very big change in the extrapolated rupture time results. Power-law breakdown is the dominating creep mechanism in the repository. At very low stresses below 40 MPa where the secondary creep rate is totally negligible, some contribution to the primary creep can still be obtained. Below 40 MPa the creep exponent can be estimated to 3 to 6, which is in the power-law regime. The creep models that have been developed and that are presented later in the report can handle both the power-law and power-law breakdown regimes. Climb and glide of dislocations are controlling the deformation also at very low stresses.

4 Creep of oxygen free high conductivity copper

A literature survey was carried out before selection of material for creep testing. Published literature data from 1945 to 1982 were surveyed and creep data extracted. It was concluded that most data were from short term creep tests that had not reached the secondary creep stage. The temperatures ranged from 0 to 300°C. The materials were usually annealed before testing. Nevertheless, modelling of the limited data was performed and constitutive relations identified. The average value of the Norton exponent n in the power law Equation 4-1 was found to be 2.5 and the activation energy for creep Q 1.0×10^5 J/mol.

$$\dot{\epsilon} = A_0 \exp\left(-\frac{Q}{RT}\right) \sigma^n \quad 4-1$$

None of these results are consistent with later test results.

The first creep tests were performed on Oxygen Free High Conductivity copper (Cu-OF) delivered by Outokumpu /5, 6/. The chemical composition is not reported, but was probably according to EN 1976 Cu-OF1 specification. Base metal, weld metal, cross-weld and simulated heat affected zone (HAZ) specimens were tested for electron beam welds. The best match for the real heat affected zone was found to be 800°C for one hour and then air cooling. A total of 30 creep tests were conducted and 29 of these ruptured. The standard 5K50-specimen with 50 mm gauge length and 5 mm diameter was used, Figure 3-1. The results from the testing can be found in Table 14-3 and Figure 4-1 and the Norton plot for the same results in Figure 4-2.

It can be observed that the Norton exponents are between 10 and 27, indicating a power-law breakdown behaviour. Measured elongation for the creep tests was strongly dependent on the applied stress with higher ductility for higher stresses, Figure 4-3. The simulated HAZ showed the lowest ductility values. Low elongation values of about 5% were obtained at stresses below 100 MPa. The authors comment that there was large variation in the creep response for different parts of the weld and from the base metal.

In 1992–94 the results from the next creep tests on Cu-OF were published /7/. Oxygen free copper was studied both in forged (000-series), extruded (200-series), and electron beam welded (100-series) state.

The results from the creep testing are given in Table 14-4 and Figure 4-4 and the Norton plot can be found in Figure 4-5. The extruded material had significantly longer creep life than the forged material. Norton exponents were between 4 and 7, which is in the power-law regime. Rupture elongation is given in Figure 4-6 and it is evident that the forged material has almost no creep ductility. This has dramatic consequences because this makes Cu-OF unacceptable as materials for nuclear waste canisters. The extruded material has a modest creep ductility of about 10%.

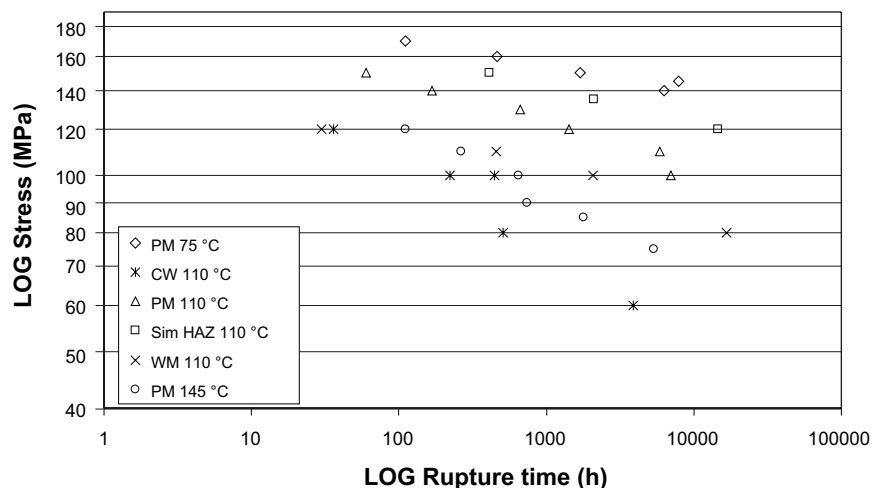


Figure 4-1. Influence of applied stress on creep rupture time for Cu-OF at 75 to 145°C /5/. PM parent metal, CW cross weld, Sim HAZ simulated HAZ, WM weld metal.

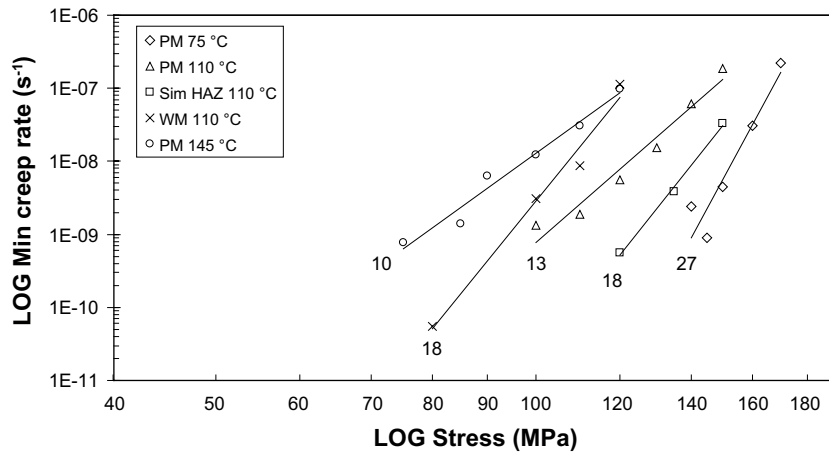


Figure 4-2. Norton plot for Cu-OF at 75 to 145°C /5/. The Norton exponents are marked in the graph.

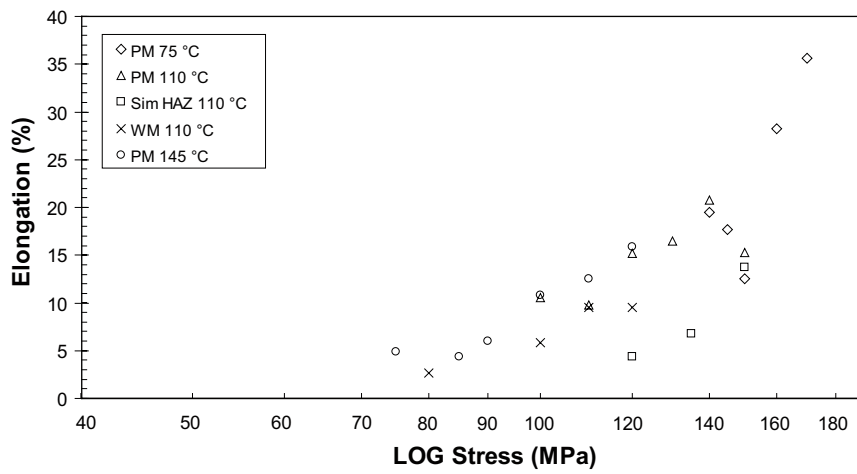


Figure 4-3. Rupture elongation versus creep stress for Cu-OF at 75 to 145°C /5/.

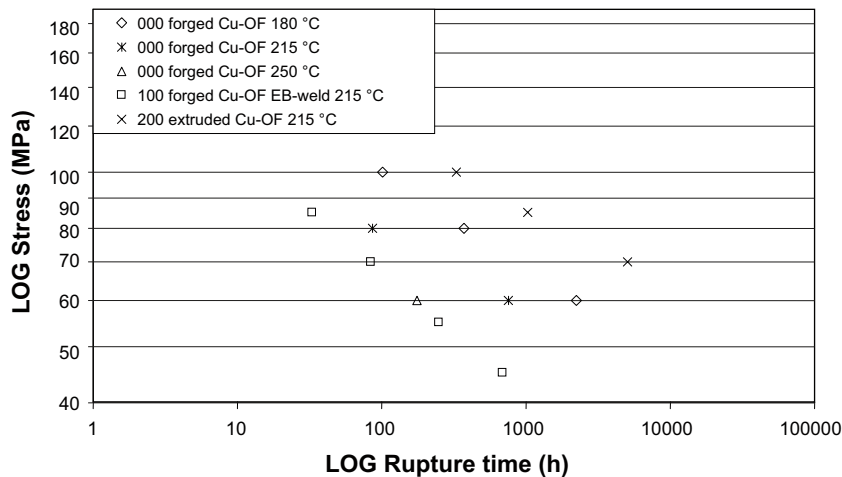


Figure 4-4. Influence of applied stress on creep rupture time for Cu-OF at 180 to 250°C /7/.

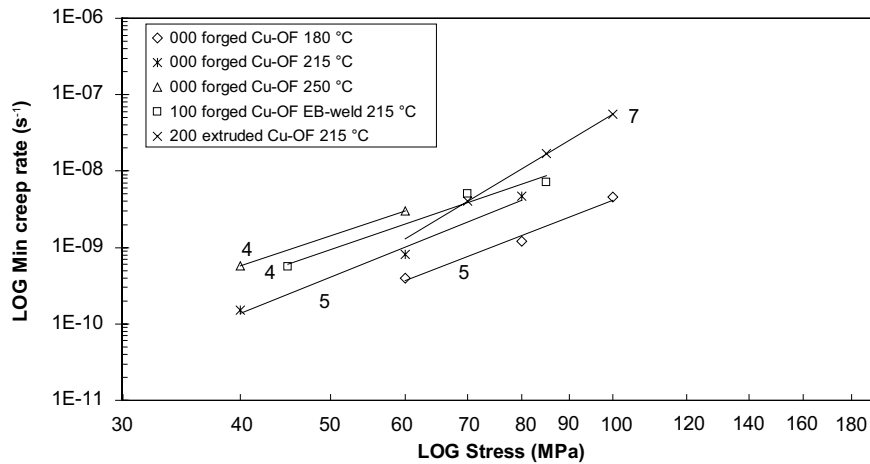


Figure 4-5. Norton plot for Cu-OF at temperatures from 180 to 250°C /7/. The Norton exponents calculated are marked in the graph.

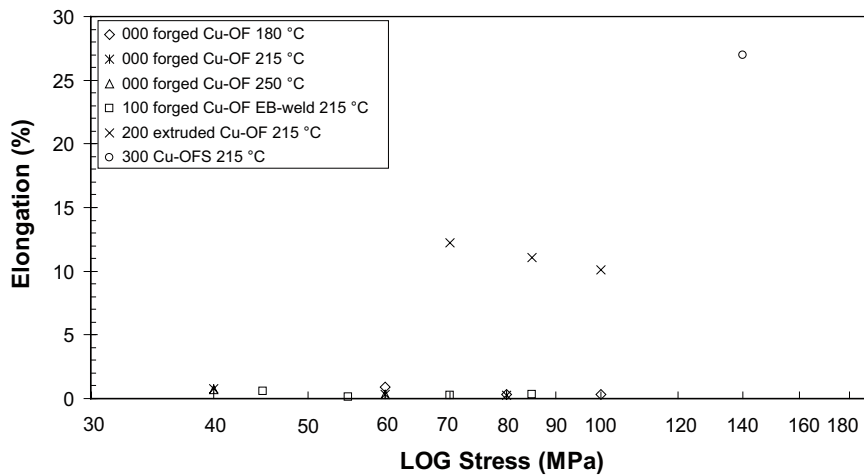


Figure 4-6. Influence of creep stress on rupture elongation for Cu-OF at temperatures from 180 to 250°C /7/.

In the discussion of the results it is mentioned that the grain size affects the creep ductility of copper. Results from the published literature indicate that maximum ductility is obtained with a grain size of 50–100 μm , and the authors did not find anything in their results that contradicts these findings.

The effect of sulphur is also discussed, and it is stated that sulphur has a detrimental effect on the creep ductility. Auger microscopy has shown that the sulphur migrates to grain boundaries and is found on the inside faces of cavities, possibly contributing to the formation of cavities.

Raj and Langdon published creep rate data for Cu-OF in 1989 /37/. The lowest test temperature was 350°C. Thus, there is no overlap with the results presented above. In Chapter 9.1 a model for the creep rate is used to the different sets of data.

In the 600-series electron beam welded (EB-welded) specimens were cut from a Cu-OF block /13, 14/. All 600-series specimens are from the weld metal taken either longitudinally along the weld or transverse through the weld depth. The results from the testing can be found in Table 14-6 and in Figure 4-7 and Figure 4-8, respectively. No significant difference could be measured for longitudinal and transverse specimens, but compared to previously tested materials both creep life and ductility were considerably lower. In the same graphs the results from testing of catalytically deposited copper are given (series 800). The directions, longitudinal and transverse, do not signify a special grain orientation as in the weld specimens but rather specimens taken in two different directions in the received slab. The results were poor and no further testing was performed on catalytically deposited copper.

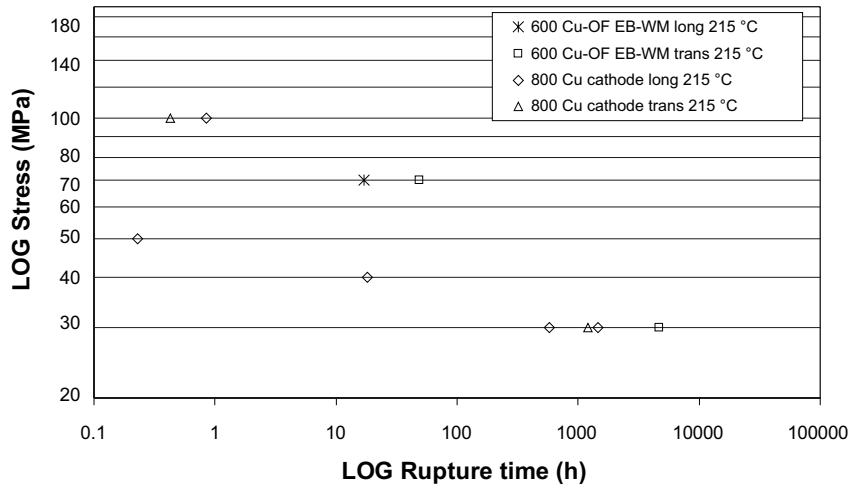


Figure 4-7. Influence of applied stress on creep rupture time for EB-welds and cathode deposits for Cu-OF /13, 14/.

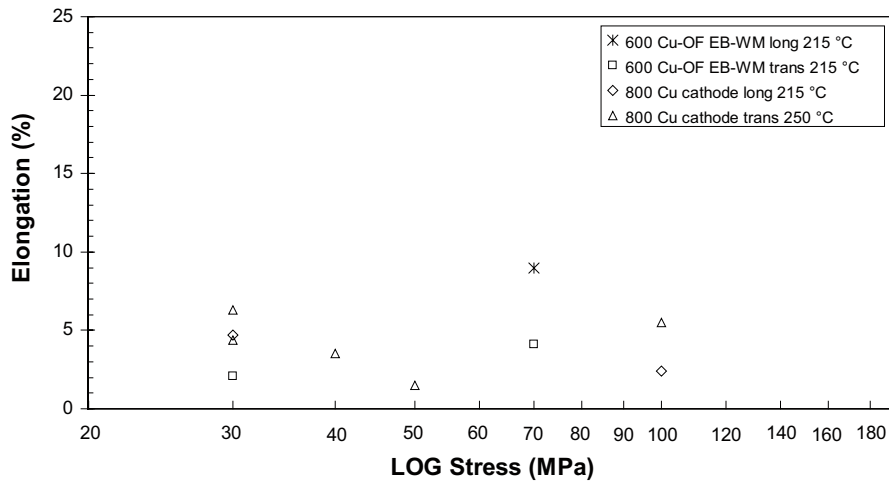


Figure 4-8. Rupture elongation for EB-welds and cathode deposits for Cu-OF /13, 14/.

5 Creep of phosphorus doped copper, Cu-OFP

5.1 High temperature testing

Extensive creep testing on Cu-OFP was performed for two batches named 400 and 500 /10/. The chemical compositions of the copper tested together with other batches are found in Table 14-1. The product forms used are summarised in Table 14-2. The material tested was extruded Cu-OFP and the temperatures varied from 200 to 450°C. The prime purpose of the testing was to demonstrate that the low creep ductility found for Cu-OF was not present in Cu-OFP. In Figure 5-1 to Figure 5-2 the results are given in graphical form and in Table 14-5 in tabulated form.

The creep strength of Cu-OFP is much higher than that of Cu-OF, cf. Figure 4-4. The variation in strength between the 400 and 500 series is pronounced, in spite of the fact that the materials have quite similar composition. Noteworthy is the strong dependence on temperature for both series 400 and series 500. The Norton exponent falls between 5 and 17 for both series, Figure 5-3 and Figure 5-4.

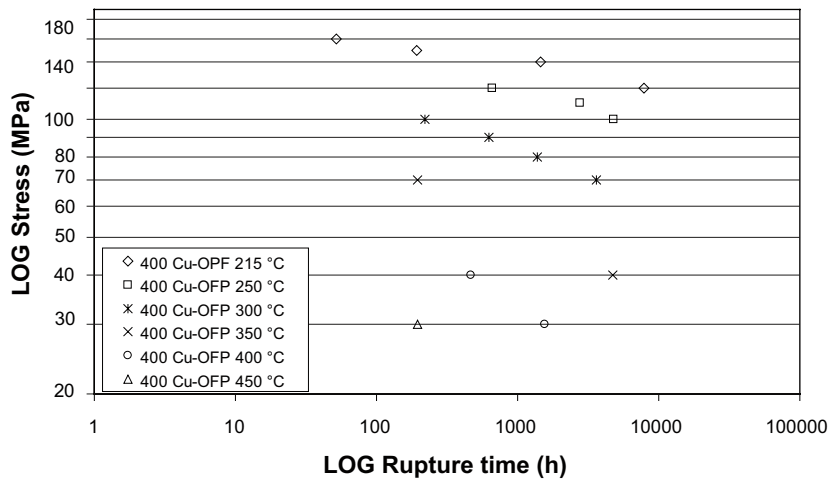


Figure 5-1. Influence of applied stress on creep rupture time for Cu-OFP (400 series) /10/.

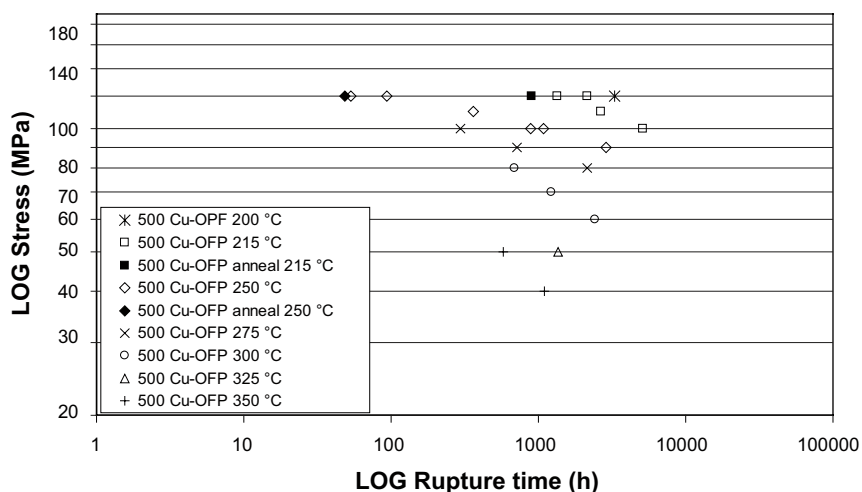


Figure 5-2. Influence of applied stress on creep rupture time for Cu-OFP (500 series) /10/.

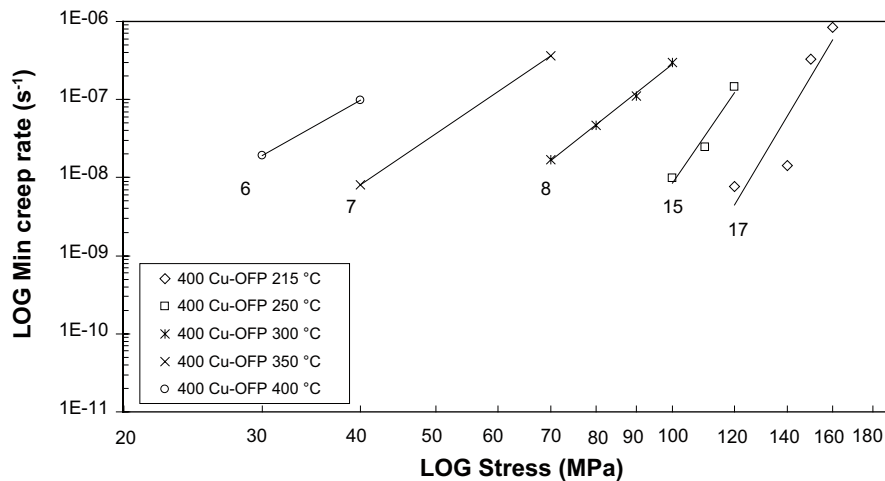


Figure 5-3. Norton plot for the 400 creep test series (Cu-OFP) /10/. The Norton exponents are marked in the graph.

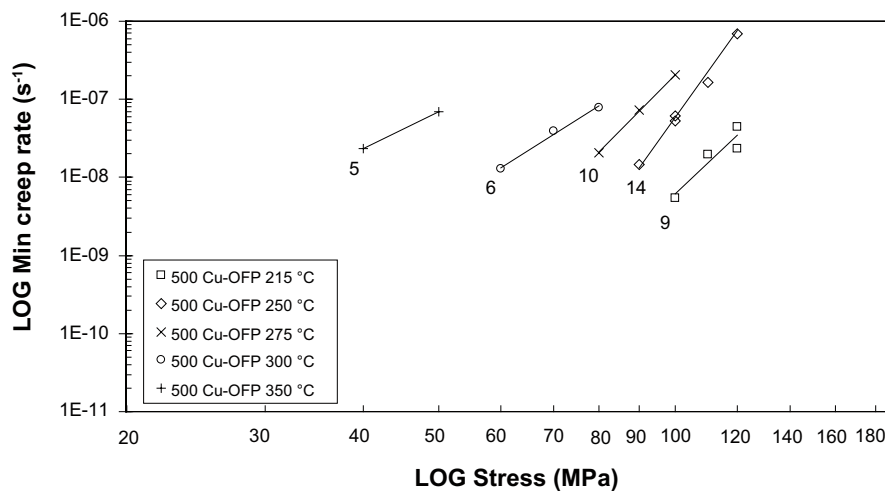


Figure 5-4. Norton plot for the 500 creep test series (Cu-OFP) /10/. The Norton exponents are marked in the graph.

The lower Norton exponents were obtained at the higher temperatures indicating that at temperatures over 300°C the creep mechanism is predominately power-law creep, and at lower temperatures the creep shows progressively more and more power-law breakdown behaviour. Creep ductility was found to be dependent on applied stress for series 500 and to some extent for series 400, with higher ductility for higher stresses, Figure 5-5 and Figure 5-6. In all cases the creep elongation was above 10%. Below 300°C the creep elongation exceeded 30% which is very satisfactory. For the 500 series two specimens were annealed for 5 minutes at 600°C and, probably, air cooled /13/. The annealed specimens have similar creep lives as the unannealed ones, but show a marked increase in ductility, Figure 5-6. When examined metallographically a slight increase in grain size was found but this is not considered enough to explain the higher ductility.

Five specimens were tested at 600°C, Figure 5-7. Two of these ruptured and the others were stopped before failure. The ductility measured for the ruptured specimens was between 10 and 15%, Figure 5-8. The purpose of these tests that were carried out a very low stress was to check whether the creep deformation was diffusion controlled (Nabarro-Herring creep) which the Frost-Ashby deformation maps suggest. The creep exponents found were however 2 to 3, which rules out Nabarro-Herring creep that is associated with a creep exponent of unity.

A conclusion from the work is that the addition of 50 ppm phosphorus increased creep ductility from 0 to 10% for Cu-OF to 30–50% for Cu-OFP below 300°C at longer testing times. The addition also increased creep life significantly.

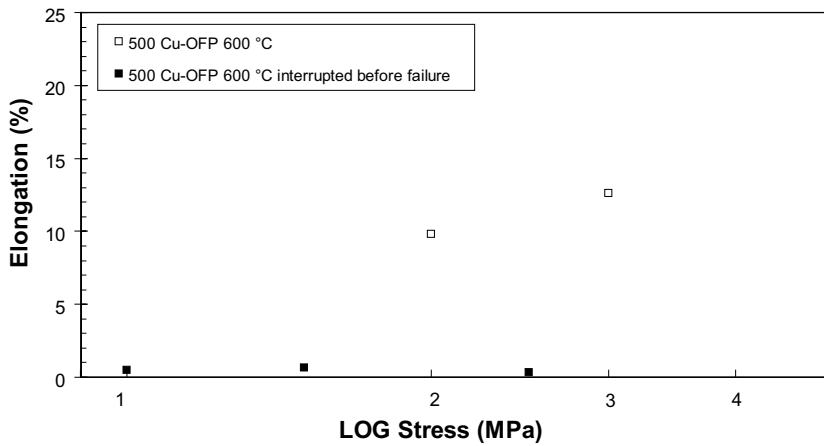


Figure 5-8. Rupture elongation the 500 creep test series tested at 600°C /10/.

The 700 series is divided into two parts, 700 and 720 series, where both are electron beam welds made from OFP copper /13, 14/. In the 700 series longitudinal and cross-weld specimens were tested. The cross weld specimens were taken from different heights in the weld as can be seen in Table 14-6 but since no significant variation was measured they are presented as one cross-weld series in Figure 5-9. The 720 series comprised specimens cut from a weld made to simulate a lid weld made from Cu-OFP. Longitudinal, transverse and cross-weld specimens were tested and the results overlap the 700-series with the transverse specimens exhibiting lower creep strength. Creep ductility was modest at lower stresses, Figure 5-10.

The dependence on specimen size and annealing before testing is investigated in /12/. Specimens with a 10 mm diameter have been compared to specimens with a 5 mm diameter, both annealed and as-machined. The annealing process was chosen as 5 min at 600°C followed by a water quench. The conclusion is that annealed 5 mm specimens give similar results as as-machined 10 mm specimens. As-machined 5 mm specimens show lower ductility measurements and longer creep lives. Tensile tests are affected in a similar manner. The reason for the lower ductility in as-machined 5 mm specimens is attributed to cold work during the machining process. The recommendation is to use annealing on 5 mm specimen for creep studies, or to use 5 mm specimens and view the results as inherently conservative in ductility.

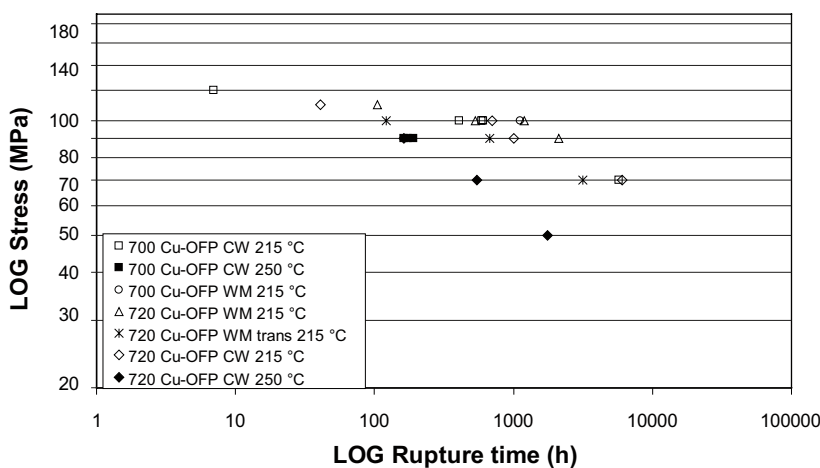


Figure 5-9. Creep rupture time plotted against applied stress for the 700 and 720 creep test series /13, 14/.

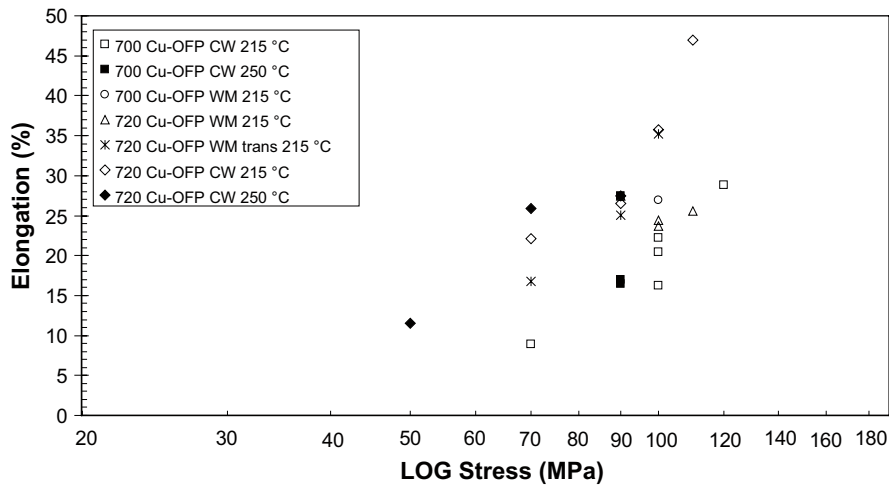


Figure 5-10. Rupture elongation the 700 and 720 creep test series /13, 14/.

5.2 Influence of grain size, sulphur and phosphorus content

A creep study was carried out for 20 mm extruded bars with different phosphorus and sulphur content to evaluate the threshold level for the effect on creep ductility /18, 19/. The effect of grain size was also investigated. The following phosphorus contents were studied 0 (P free), 30, 60, 65 and 105 ppm. Six grain sizes were covered 300, 350, 450, 800 and 2,000 μm . All test series except one had a sulphur content of 6 ppm. One series with 12 ppm S showed the same creep properties as the corresponding heat with 6 ppm S. All testing was performed at 175°C and the results from the testing can be found in Table 14-7 and in graphical form in Figure 5-11 and Figure 5-12.

As can be seen from the results they generally overlap for all material conditions, with two exceptions, the material without phosphorus and the material with the largest grain size. Both single out by having low creep ductility and short creep lives compared to the other materials, Figure 5-13. For the other series the rupture elongation is about 30% or above. The creep exponent is about 45, Figure 5-14.

The conclusions from the investigation are that very large grain sizes, >800 μm , and phosphorus content below 29 ppm should be avoided to prevent low ductility.

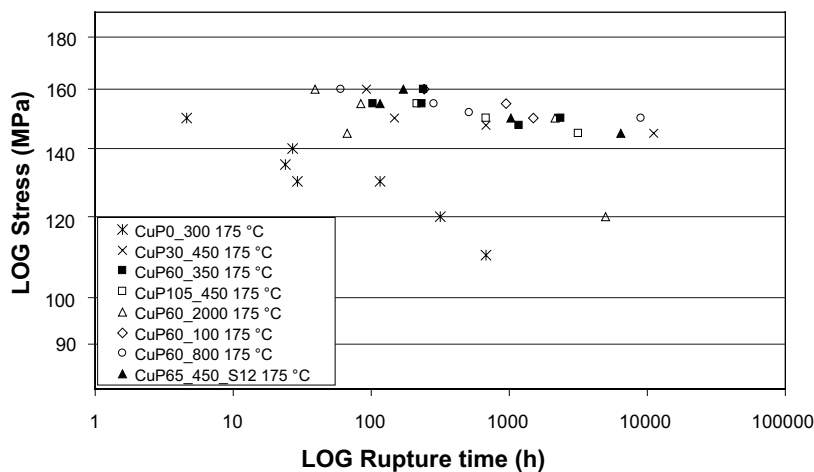


Figure 5-11. Creep rupture time plotted against applied stress for varying sulphur content, phosphorus content and grain size /18, 19/. The identifier P65_450_S12 means that the heat had 65 ppm P, a grain size of 450 μm and 12 ppm S.

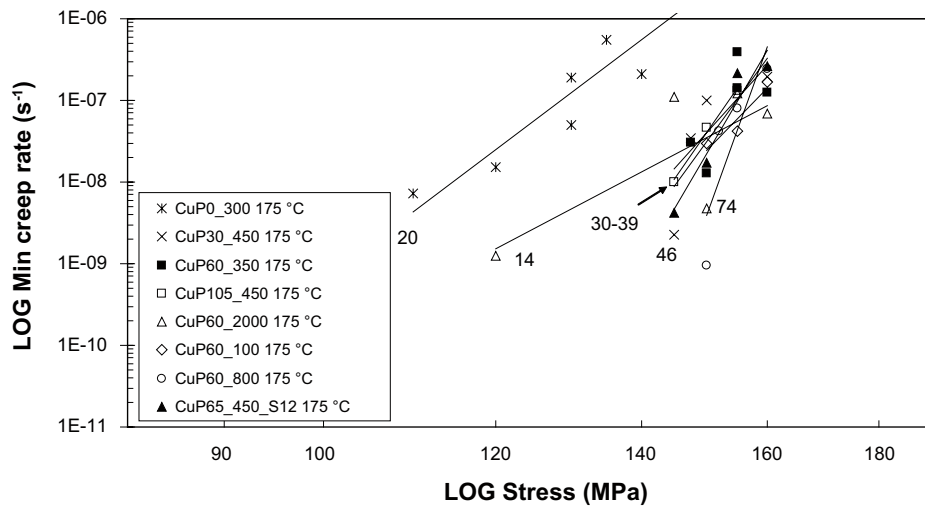


Figure 5-12. Norton plot for the results in Figure 5-11 where sulphur content, phosphorus content and grain size were varied /18, 19/. The Norton exponents are marked in the graph.

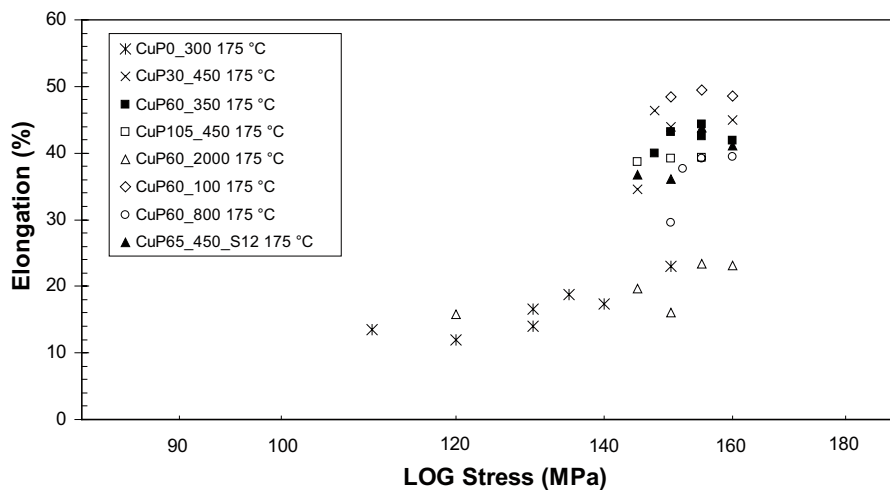


Figure 5-13. Rupture elongation for the results in Figure 5-11 where sulphur content, phosphorus content and grain size were varied /18, 19/.

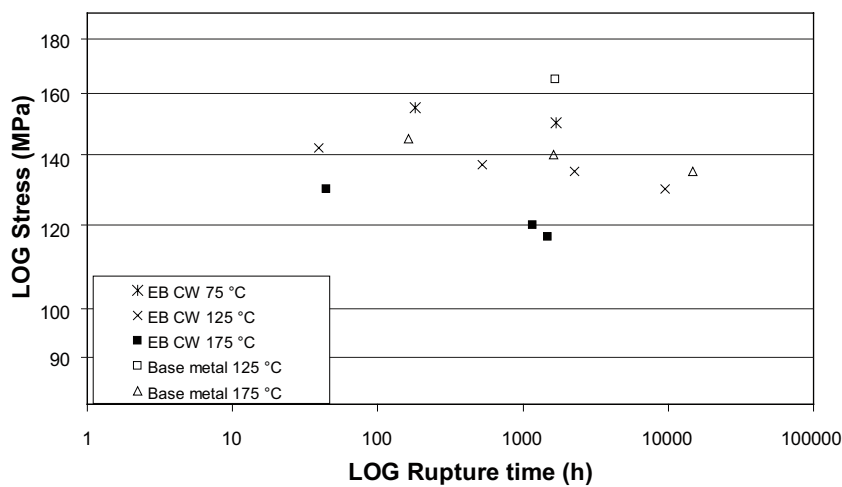


Figure 5-14. Creep rupture time plotted against applied stress for base metal and electron beam weld specimens /21, 22/.

5.3 Creep testing at low stresses

Ho has performed creep tests for Cu-OFP at low stresses 20–60 MPa at 95, 125, and 150°C /38, 39/. At these low stresses the specimens never reached secondary creep and they did not rupture. Only the initial part of primary creep can be recorded. The results are analysed and discussed in Chapter 9.4 on primary creep.

5.4 Electron beam and friction stir welds

Previously all testing had been performed on electron beam welds and base material. Now friction stir welds (FSW) were included as well /21, 22/. Creep test results are given in Table 14-8 and in graphical form in Figure 5-14 to Figure 5-19.

All tests in this work show over 20% ductility but the appearance of the specimens are different. The electron beam welds exhibit sufficient ductility at a glance, but the deformation is localised to the narrow weld metal, where the ductility is much higher locally. The friction stir welds on the other hand strain evenly over the whole gauge length, and only in the last part of the creep test does necking appear in the middle of the specimen. This even creep deformation should in service provide better protection against cracking. The FSW welds show a creep ductility of 30% or more that is quite satisfactory.

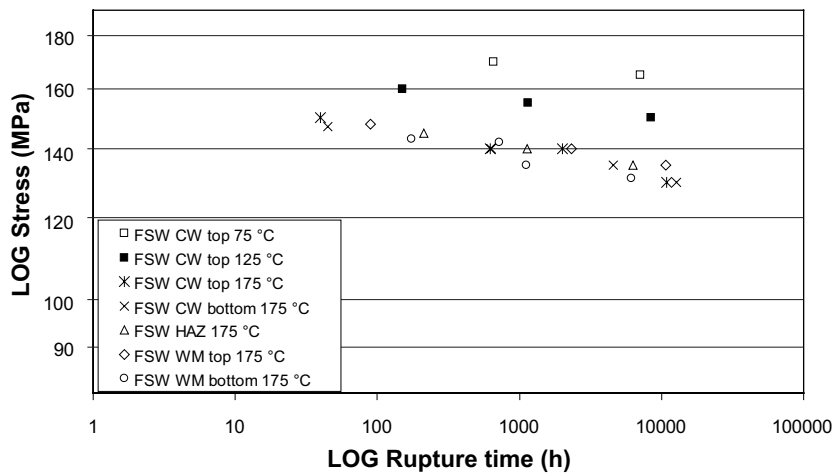


Figure 5-15. Creep rupture time plotted against applied stress for friction stir weld specimens /21, 22/.

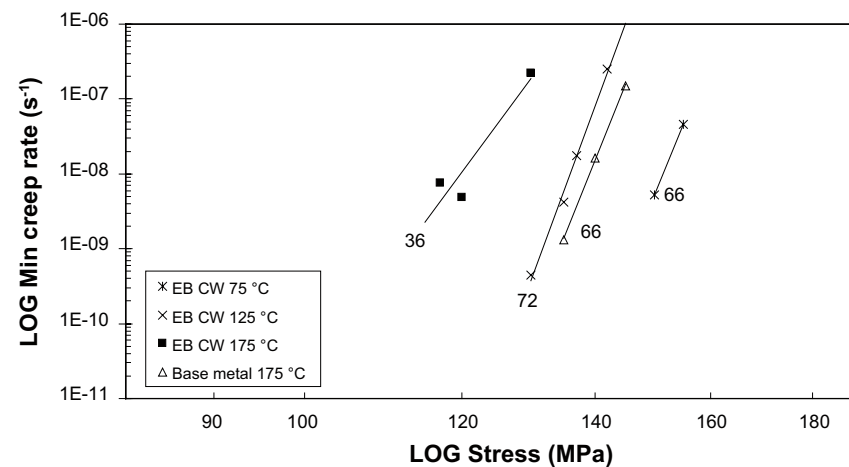


Figure 5-16. Norton plot for electron beam welds. Comparison to parent metal is made /21, 22/. The Norton exponents are marked in the graph.

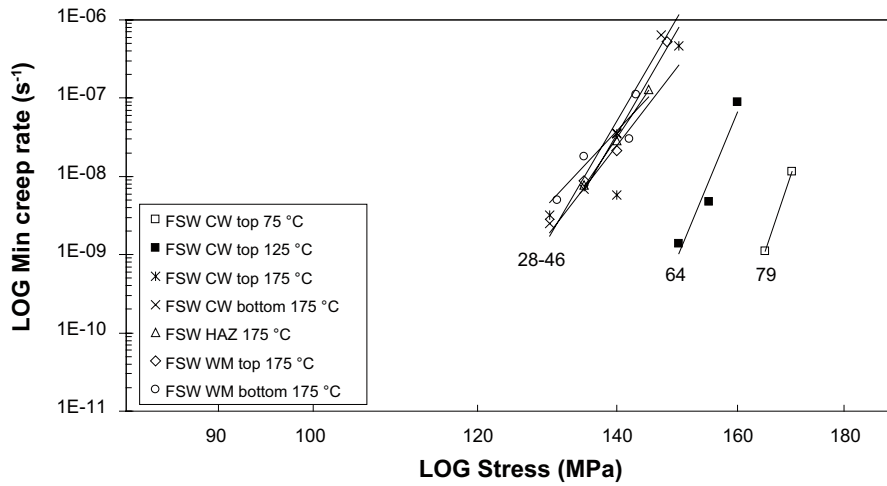


Figure 5-17. Norton plot for friction stir weld specimens /21, 22/. The Norton exponents are marked in the graph.

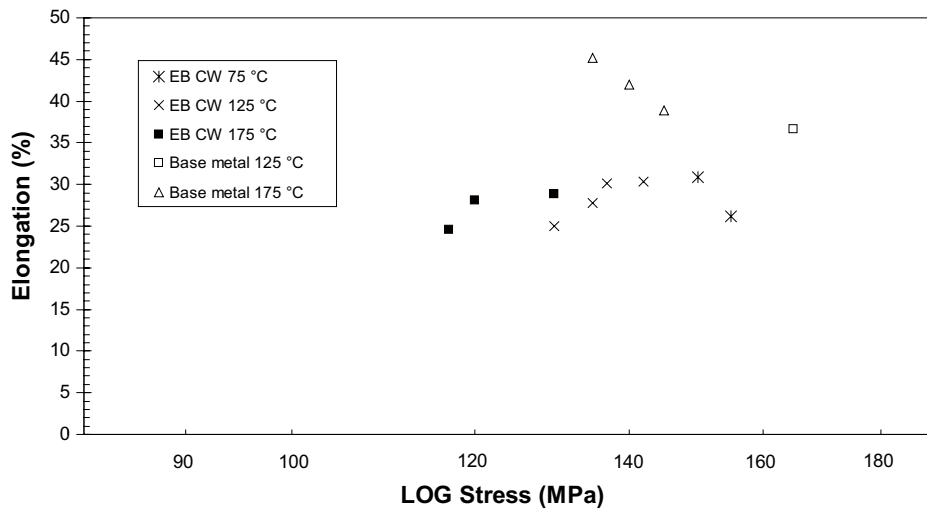


Figure 5-18. Rupture elongation for base metal and electron beam weld specimens /21, 22/.

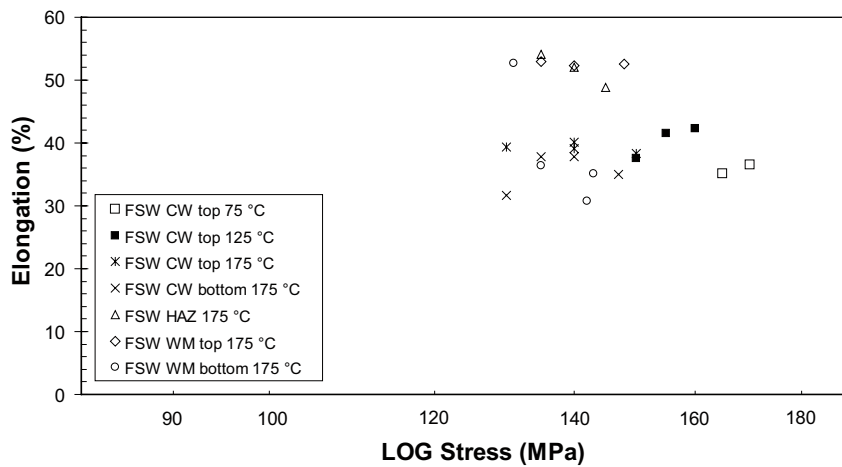


Figure 5-19. Rupture elongation for friction stir weld specimens /21, 22/.

In addition the electron beam welds have an average grain size of 2,000 μm compared to the 75 μm for the weld metal from the friction stir welds. If the low temperature is taken into account the Petch-Hall effect gives a contribution to the strength of the weld of about 15 MPa, which is in the same order of magnitude as the difference in rupture strength. Previous testing has also shown that large grain sizes are detrimental to the creep strength /18/.

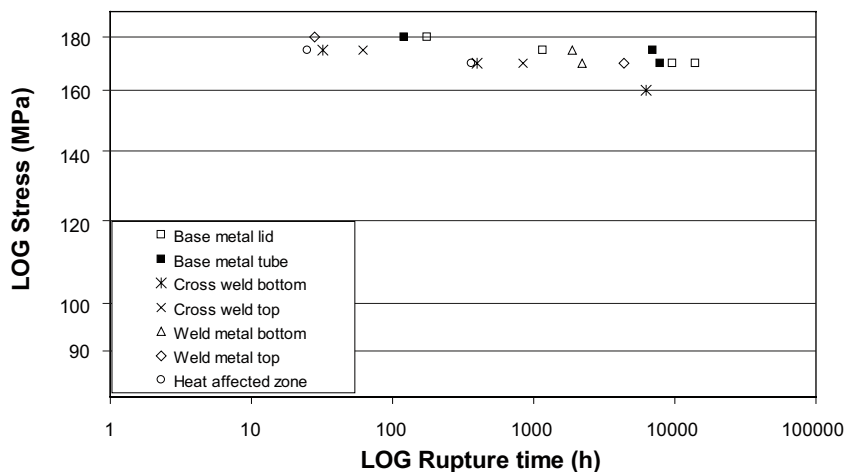
To conclude, the results from this work show that frictions stir welds are more suitable than electron beam welds for the canister weld, and the friction stir welds have adequate properties for this application.

In 2005 friction stir welding was chosen as the preferred welding method. But the previous study had used hot rolled plate which had been rolled formed as the material in which the welds was performed. Extruded material was much more likely to be used as a canister material and a new project was initiated to study the creep response of thick wall FSW welds in extruded tube. SKB had by this time also accumulated experience in using the FSW welding machine at the Oskarshamn canister laboratory and a real weld was used to extract the tested specimens /24/.

The specimen extraction diagram for the FSW welds have been presented before in Figure 3-2 and both base metal from the lid and from the tube was tested along with weld metal, heat affected zone and cross weld specimens. For the EB welds only cross weld specimens were tested.

The results in Figures 5-20 to 5-22 show that the good ductility of phosphorus alloyed copper is also present at 75°C. The creep ductility exceeds 40%. The creep tests are well within the power-law breakdown regime with Norton creep exponents in the range of 50 to 120. The way in which the load is applied to the specimens is also important to the result. The loading time was varied for a number of specimens otherwise tested at the same stress/temperature and the measured loading strains were significantly different. This prompted a follow up project where the loading was further varied.

The weakest part of the frictions stir weld was found to be the heat affected zone, or the intermixing zone, which has not received the same mixing as the weld metal but where the temperature has been almost as high as in the weld metal. In cross weld specimens which contained both base metal, weld metal and two heat affected zones, two areas of necking could be seen. The areas corresponded to the heat affected zones and one of the necking areas contained the rupture, but the other one was also on the verge of rupturing. Even so, there was no large difference between the creep results from the base metal, from the weld metal, or from the heat affected zone specimens.



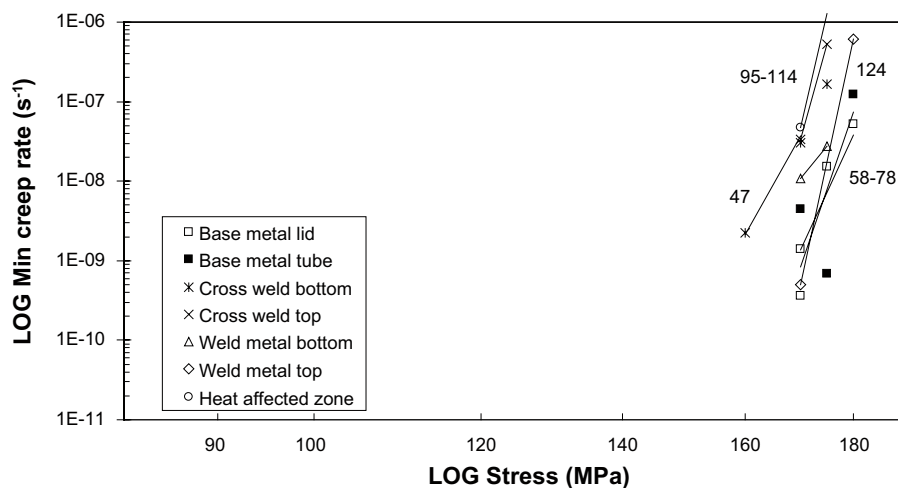


Figure 5-21. Norton plot for friction stir welds at 75°C /24/. The Norton exponents are marked in the graph.

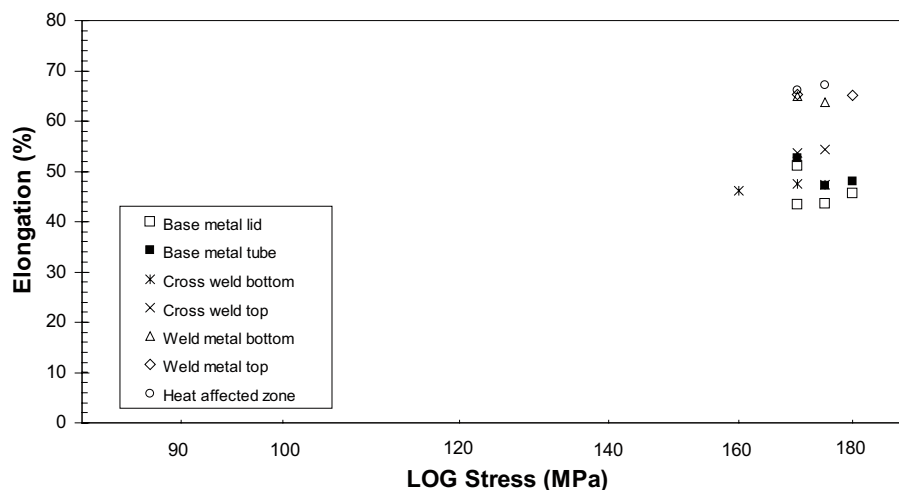


Figure 5-22. Rupture elongation friction stir welds at 75°C /24/.

5.5 Weld reduction factors

A weld is often a weak part in any construction. Therefore when designing a component a weld reduction factor must be applied. The factor is usually extracted from laboratory tests of base and weld material. The weld reduction factor is then used for calculating allowable stresses in the component along with a safety factor.

In the case of the nuclear waste canister the lid is welded to the tube to seal the canister. The bottom can also be welded but there is a way to manufacture the tube integral with the tube. It is not yet decided which of the two options that is to be used. In both cases the weld is a part of the completed canister and the design calculations have to account for the reduced strength of the weld.

Two weld methods have been considered for the canister, and specimens cut from test welds of both types have been creep tested. The temperatures for the tests have varied but the majority of the tests have been performed at 75°C or 175°C. Since the creep response is different at the two temperatures, the weld reduction factor has to be measured for each temperature. In Figure 5-23 and Figure 5-24 the weld tests have been collected in the same graphs. It can be seen that the cross-weld specimens need a lower stress to attain the same rupture time. The reduction in rupture time can be converted to a weld creep strength reduction factor using Equation 5-1 /40/.

$$SRF(t/T) = \frac{R_{u/t/T} - R_{u(w)/t/T}}{R_{u/t/T}} \quad 5-1$$

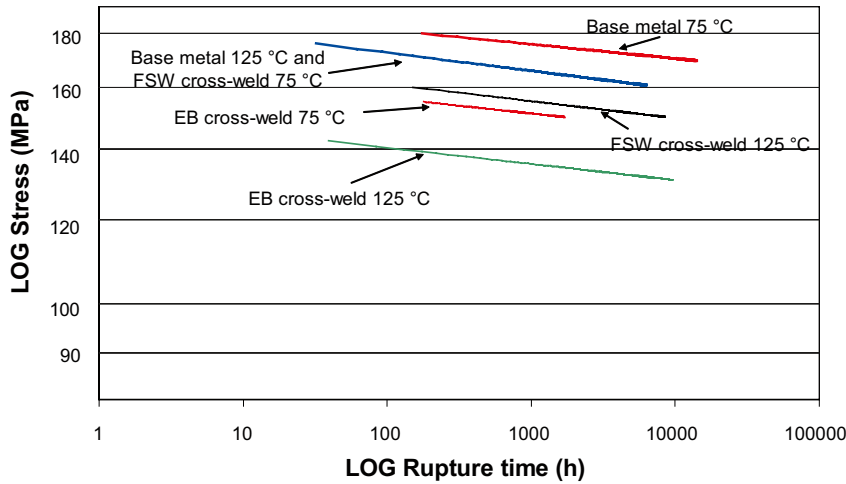


Figure 5-23. Comparison of creep tests of weld specimens performed at 75 and 125°C. Base metal tests are included in the graph.

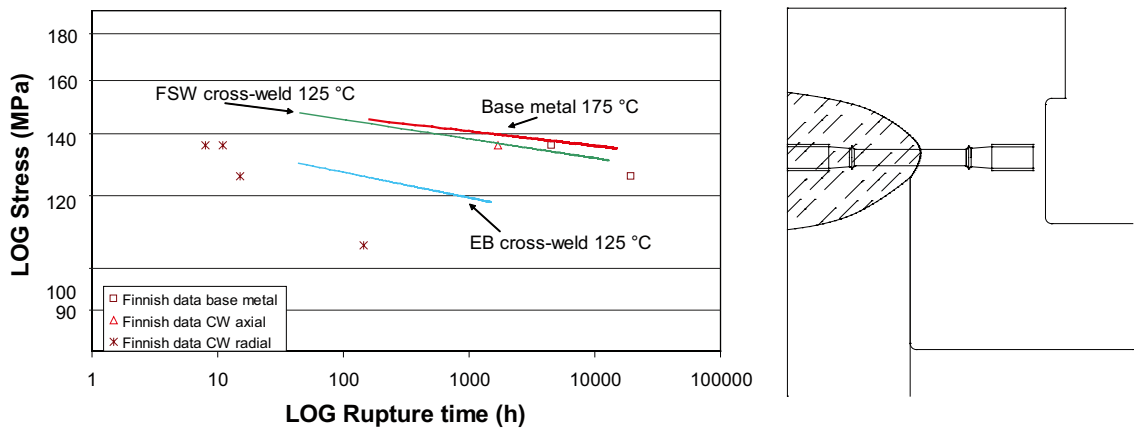


Figure 5-24. a) Comparison of creep tests of weld specimens performed at 175°C. Base metal tests are included in the graph. Included are also data from a Finnish study on FSW welds b) Specimen extraction of radial cross-weld specimens /40/.

Table 5-1. Weld creep strength reduction factors for creep rupture after 1,000 h.

Weld type	75°C	125°C	175°C
Friction stir weld	5.7%	6.1%	2.1%
Electron beam weld	14.2%	12.1%	16.3%

where $R_{w/tT}$ is the stress to achieve a given rupture time of the base metal at a given temperature, and $R_{u(w)/tT}$ is the same for a weld specimen. The results for the welds are presented in Table 5-1. Note that the given factors are for 1,000 h creep rupture, but since the curves are roughly parallel, the same factors are valid for a wider range of rupture times. As can be seen from Table 5-1, the weld reduction factors are modest, in particular for friction stir welds. For example, for creep resistant values in the interval 20 to 50% are often found /40/.

In Figure 5-24 results from a study performed in Finland /41/ are shown. In this study, which was performed on similar material as the studies in Sweden, it was found that the creep lives of base metal and cross-weld specimens taken in the axial direction are similar to the Swedish results. The Finnish study was performed at 175°C. Included in the study were also specimens taken in a radial direction, Figure 5-24. It is known that the friction stir welds can sometimes contain a feature known as oxide

trails /42/. In the Finnish study the oxide trails or other defects, had accumulated at the bottom of the weld. This was given as the reason as why radial cross-weld specimens showed reduced rupture times, Figure 5-24. The oxide trails appear in all types of FSW, not just in copper. If they have an effect on the creep properties it would show up in all cross weld specimens. This has not been observed. Furthermore, there are no other reports suggesting that the oxide trails should have a significant influence on the mechanical properties. This area needs further study.

6 Influence of cold work on creep

6.1 Background

From the manufacturing process all the way to the final deposition in the repository the copper is subjected to handling, which can introduce cold work in the material. Tools and other handling equipment can be pressed or punched into the canister material. Cold work has also been observed after forging in the lids. Machining of copper components is a potential source of cold work. The cold work may influence the creep strength and ductility and thereby jeopardise the long term safety of the canisters.

Some information on fcc-alloys can be found in the literature, but none on copper. With increasing amount of cold work, the creep strength can increase (316, 17Cr12Ni2Mo, 650°C, max 30% cold work) /43/ or decrease (304, 18Cr10Ni, 677 and 760°C, max 12% cold work) /44/. At the same time the creep ductility is reduced /42/. The ductility decreased by 75% after 20% cold work in comparison to solution heat treated material.

The effect of cold work is influenced if recovery or recrystallisation takes place during creep. Examples are studies of 314 (25Cr20Ni) at 900 and 950°C /45/. The influence of cold work disappears after long testing times and low stresses at these high temperatures. In /46/ it is demonstrated that the effect of cold work is reduced with decreasing stress for 347 (18Cr11NiNb) at 750°C.

The studies /42–45/ are all limited to test times shorter than 1,000 h, which means that the conclusions should be handled with some caution. None of the studies /42–45/ covers cold work in compression.

6.2 Creep tests

Creep tests series have been formed for four types of cold work /34, 35/.

1. 12% strain in tension
2. 24% strain in tension
3. 12% strain in compression
4. 15% strain in compression perpendicular to the creep testing direction.

The influence of the cold work on creep rupture is illustrated in Figure 6-1.

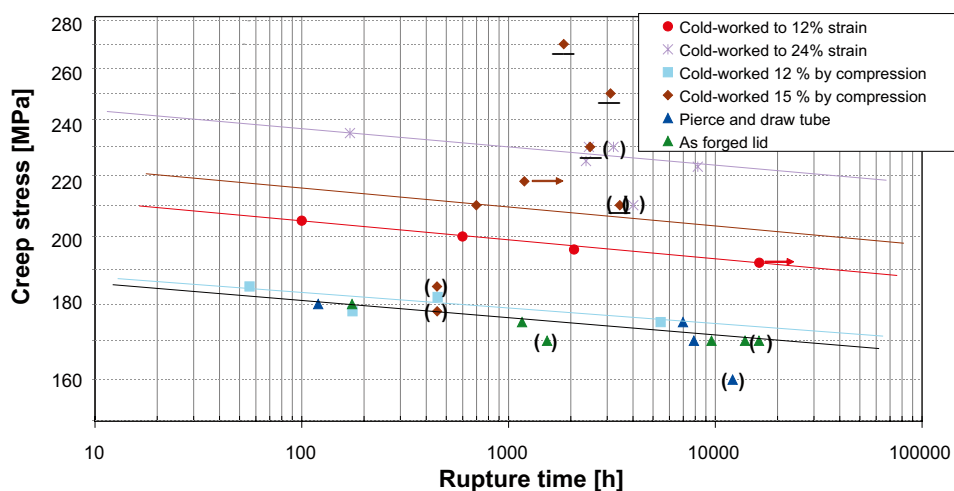


Figure 6-1. Applied creep stress versus rupture time for cold worked and reference material at 75°C. → – still in test, () – interrupted before fracture, _ – creep stress increased during testing. Four sets of cold worked copper are included. Pierce and drawn tube as well as the forged lid are reference materials without cold work /35/.

Cold work by 12% in tension gives more than 10% increase in the creep rupture strength. The corresponding increase for 24% cold work in tension is 25%. 12% cold work in compression does not influence the rupture strength at all. 15% cold work in a direction perpendicular to the test direction gives about the same increase in strength as the same strain in tension would.

For the reference materials the creep elongation is 30 to 50%, see Figure 6-2 and previous Figures in the report. The 12% cold worked copper in tension has a high ductility of 30%. For the other sets the elongation is 10 to 15%. It should also be noted that the initial strain on loading is below 2% for practically all the cold worked specimens whereas it is about 10% for the reference materials. This extra ductility margin obviously disappears for cold worked material. Surprisingly enough the cold working does not seem to influence the reduction in area. It is about 90% for both the reference and the cold worked materials. This is technically quite significant since it demonstrates that high strains can be allowed locally without immediate failure taking place.

The test results can qualitatively be understood. With increasing cold deformation an increase in creep strength can be expected as long as recovery and recrystallisation do not take place and that is not the case for copper at 75°C. If cold work in tension and compression are compared, compression would give a dislocation structure that can easily be overcome by creep strain in tension contrary to cold work in tension. Cold work perpendicular to the creep direction would only be partially removed by creep in tension.

Cold work consumes some of the available straining capacity of the material. Thus, there is no surprise that the creep ductility is reduced after cold working. It is well known that cold work increases the density of creep cavities and that gives a contribution to a reduction in the rupture ductility. The mechanisms by which the cavitation increases are not well known. One possible mechanism that has been proposed involves dislocations forming ledges at the grain boundaries that stimulates the cavity nucleation. Another possible mechanism is the increased diffusion along dislocations that gives a more rapid cavity growth.

6.3 Effect of indentations

In the manufacturing as well as during the further handling of the canisters, cold work can be introduced by accidental indentation of the copper. Both experimental and FEM-modelling of indentation with a sphere, cylinder and cone have been studied. The results are summarised by Unosson /SKBdoc 1205273/. The results show that high strains up to 50% can easily be reached. Such high cold work strains might jeopardise the canister integrity during creep.

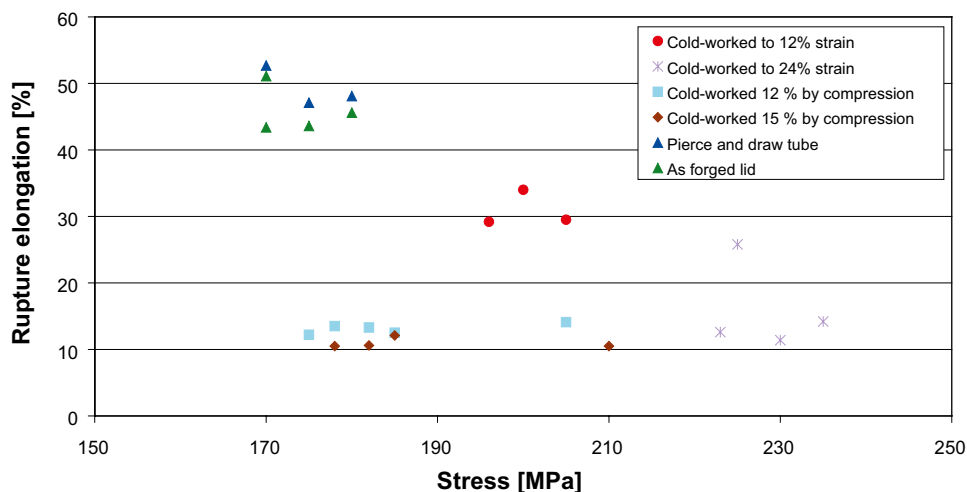


Figure 6-2. Rupture elongation versus applied creep stress for cold worked and reference material at 75°C. Four sets of cold worked copper are included. Pierce and drawn tube as well as the forged lid are reference materials without cold work /35/.

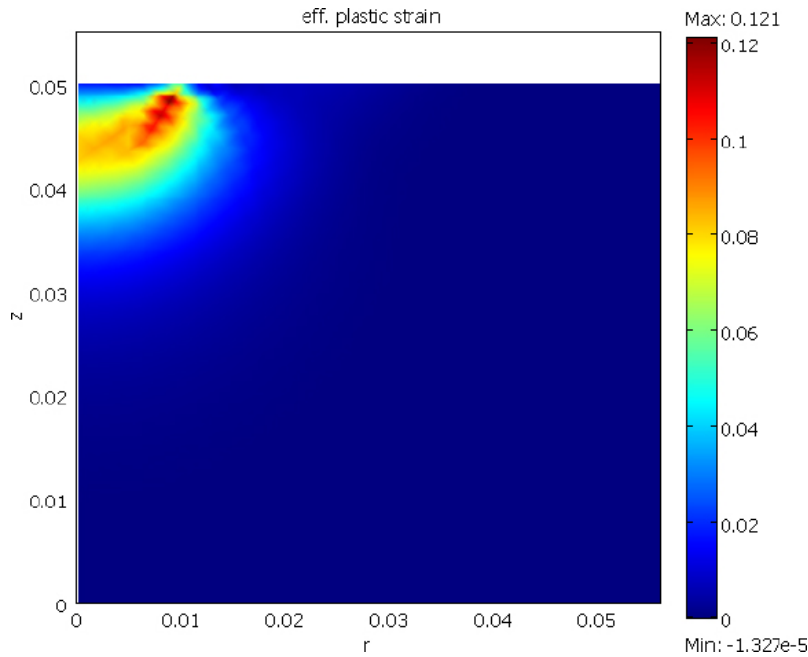


Figure 6-3. Effective plastic strain below an applied punch ϕ 20 mm with a stress 500 MPa (load 0.157 MN).

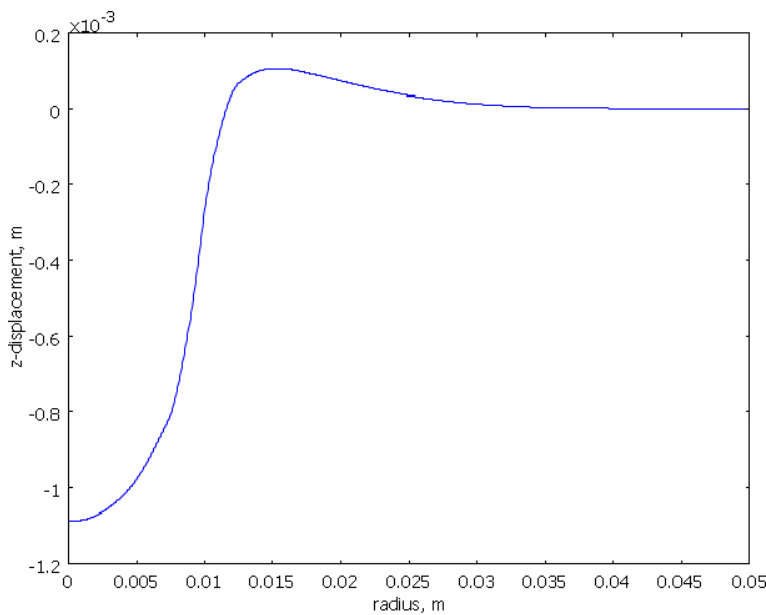


Figure 6-4. Same as Figure 6-3 but showing the displacement below the punch.

To analyse this situation and to try to find a solution, new FEM computations have been performed. The case considered is indentation with a cylindrical punch with a diameter of 20 mm. The applied stress is 500 MPa. The results are illustrated in Figure 6-3 and Figure 6-4. The maximum plastic strain is 12% and the displacement is 1.1 mm. If the stress is increased to 600 and 700 MPa and the same computations are performed again, the plastic strain is raised to 23 and 53%, respectively. At the same time the depth of the indentation is increased to 2 and 3.9 mm, respectively. It is evident that an applied stress of 500 MPa gives an acceptable plastic strain but a slightly higher stress of 700 MPa does not. To handle the canister, it is consequently essential to use so soft tool materials that a stress level of 500 MPa is not exceeded.

7 Slow strain rate tensile tests

After the deposition in the repository the copper canisters for nuclear waste will gradually be exposed to a temperature close to 100°C. The external pressure from the surrounding bentonite and the ground-water will reach around 15 MPa after a period that can take many years /47/. A slow plastic deformation will take place due to the external pressure and increased temperature and the gap between the canister and the insert will gradually be closed.

To model the deformation in the copper canisters, accurate data for creep and plastic deformation must be available. The generation of creep data has been described above in this report. In the present chapter slow strain rate tensile tests will be summarised for phosphorus alloyed pure copper. The copper must have good ductility properties to avoid crack formation during the deformation. The ductility behaviour can be studied both with traditional creep tests and slow strain rate tensile tests.

The first slow strain rate tensile tests for Cu-OFP were performed for cold worked material /48/. Tests were carried out at 20 to 175°C for strain rates between 10^{-7} and 10^{-3} . Two examples of results are shown in Figure 7-1. In terms of engineering stresses the results have a simple form. After the elastic part the curves become essentially flat. A stationary value is reached. At 20°C there is a slight work hardening that does not appear at higher temperatures. The behaviour of the curves is what would be expected at higher temperatures when the deformation is climb controlled. In terms of true stress, a linear work hardening is observed at all the investigated conditions.

The amount of cold work that the copper was exposed to is not known. The material is taken from a rolled formed canister cylinder. Roll forming for such a component should in principle give a modest cold deformation, but the actual cold deformation is quite significant, considering the appearance of the stress strain curves.

More recently annealed copper has been studied. Temperatures in the interval 20 to 175°C and strain rates between 10^{-7} and 10^{-4} 1/s were covered /33/. Two examples of curves are shown in Figure 7-2.

It is immediately apparent that the curves for annealed copper are quite different from those of the cold worked material. There is significant work hardening and the “flat” region is much less pronounced. It is still assumed though that the maximum value at the “flat” region represents a stationary value.

In Figure 7-3 the stationary values from the cold worked and the annealed materials are compared. In addition available creep data at 75 and 175°C are included. The SSR data for the cold worked material is close to the minimum strain rates in the creep tests. The strain rates for annealed material are higher. The dislocation barriers that are built up in the two types of tests can be expected to be different. It is likely that the dislocation barriers are broken down more efficiently in a strain controlled tests than in a stress controlled creep test. The difference in stationary stress level turns out to be 10%.

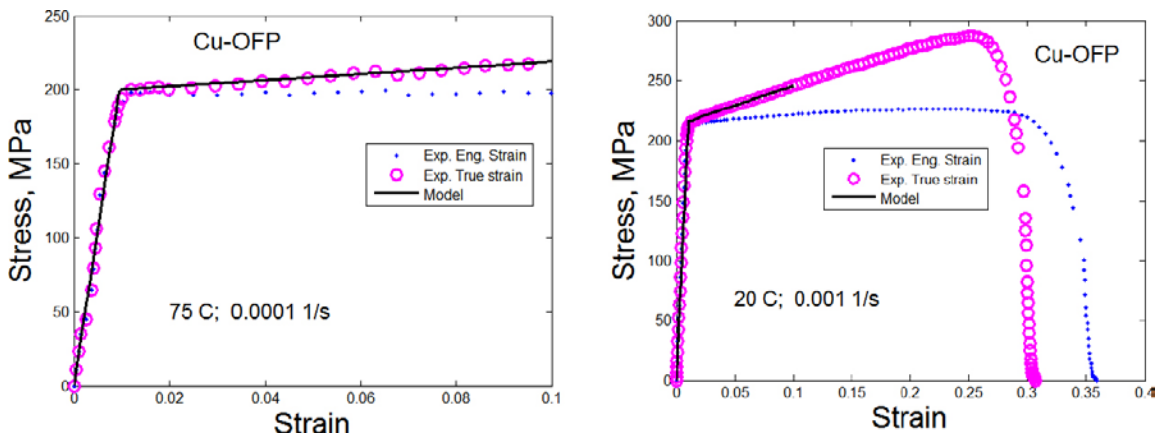


Figure 7-1. Slow rate tensile tests for cold worked Cu-OFP at 75°C, 0.0001 1/s, and 20°C, 0.001 1/s /17/.

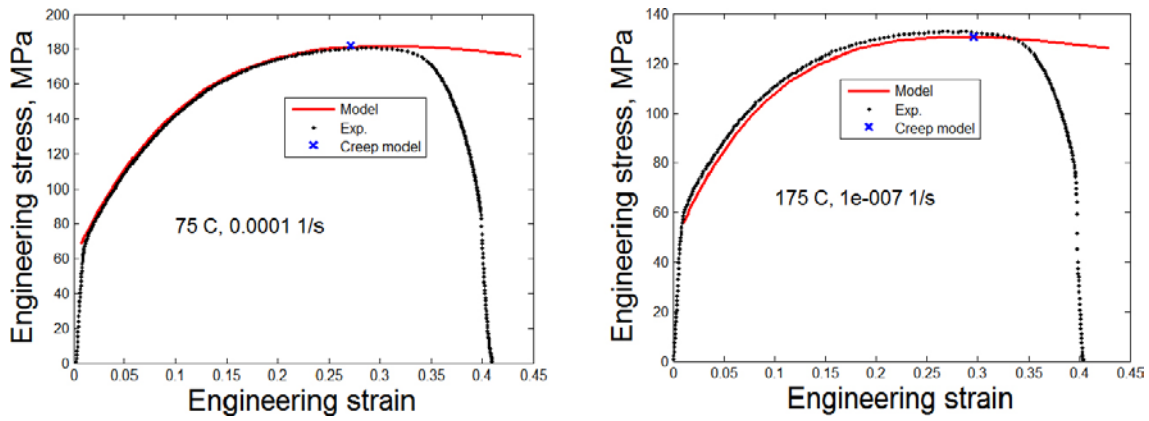


Figure 7-2. Slow rate tensile tests for annealed Cu-OFP at 75°C, 10^{-4} 1/s, and 175°C, 10^{-7} 1/s /33/.

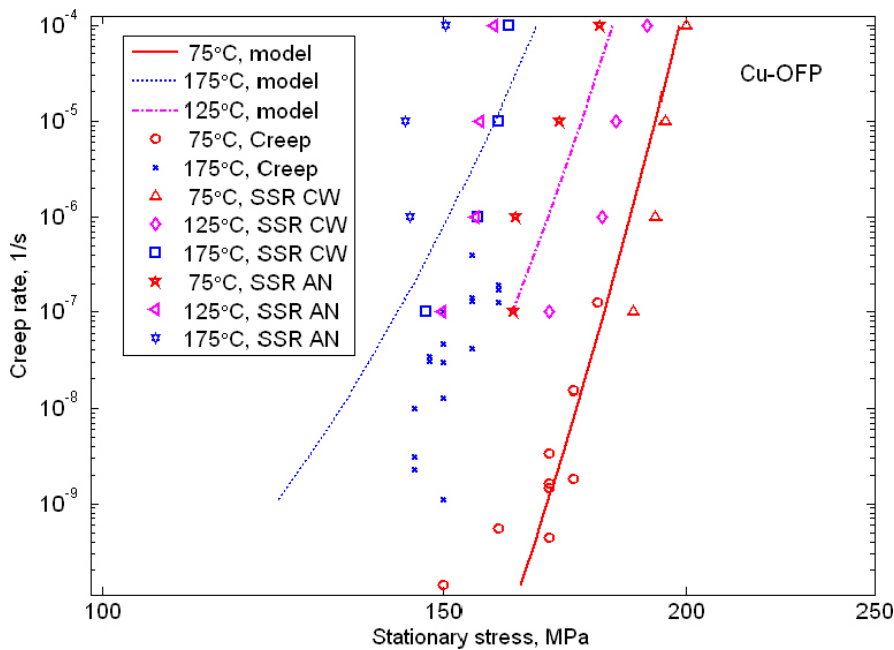


Figure 7-3. Comparison between minimum creep rates at 75 and 175°C to stationary stress in slow strain rate (SSR) tensile tests at 75, 125 and 175°C. For each temperature and strain rate, there are two SSR values. The one at the lower stress is for the annealed material (SSR AN), the one at the higher stress from the cold worked material (SSR CW). The model values for creep are discussed in Chapter 11.2.

Fundamental models for the slow strain rate (SSR) flow curves have been developed. For the cold work material, the behaviour is straightforward. We have the elastic part and the stationary flat part that is given by creep stress for the same strain rate as in the SSR tests. The creep model that is needed is described in Chapter 11. The resulting model values are illustrated in Figure 7-3.

For the annealed SSR-tests a dislocation model has been set up /33/. First a model for the temperature and strain rate dependence is formulated. In a glide controlled situation the flow stress is expected to have the same temperature dependence as the shear modulus. On the other hand under climb control, the yield strength is related to the creep strength. Above 400°C the deformation is governed by climb. At lower temperatures there is mixture between climb and glide. With the help of the creep model, which takes into account both climb and glide, the relative importance of the processes can be assessed. The resulting behaviour of the yield strength is illustrated in Figure 7-4. As can be seen both the temperature and the strain rate dependence of the yield can be represented. It should be noted that no fitting parameters are involved in Figure 7-4.

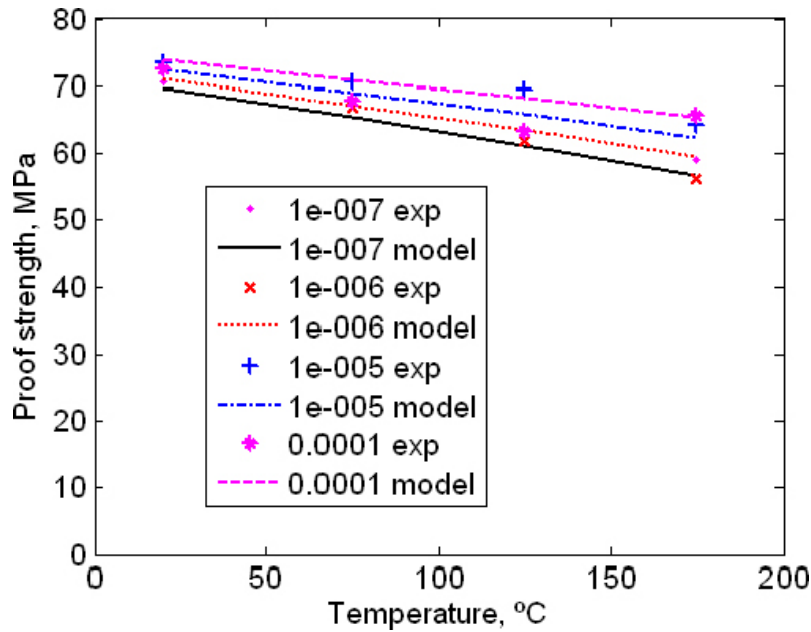


Figure 7-4. Proof strength versus temperature slow strain rate tensile tests. Values for four strain rates are shown from 1×10^{-7} to 1×10^{-4} 1/s. The lines are model values /33/.

The next step is to model the flow curve. A dislocation model originally proposed by Bergström /49/ but more frequently referred to as the Kocks-Mecking model /50/ has been taken as the starting point. This model has a sound basis and the physical meaning of all the parameters is clearly defined. Unfortunately, the model involves two parameters that have to be fitted to the experimental data. If this is done an excellent description of flow curves for FCC alloys is typically obtained.

To avoid having these fitting parameters, two basic assumptions are made. The first one is obtained by relating the part for dynamic recovery to a dislocation model developed by Roters et al. /51/. In this model it is assumed that the interaction distance is twice the core radius. This means that the dislocations have to “touch” each other before a recovery event takes place.

The second assumption is to relate the plateau level in the flow curve to the creep stress for the same strain rate. As was evident from Figure 7-3, the stationary stresses in the SSR-tests are 10% lower than in the corresponding creep stress, and this value is used in the model.

The resulting model values are compared to the experimental curves in Figure 7-1 and Figure 7-2. An excellent description of the flow curves is obtained. The relation to the creep model is illustrated in Figure 7-2 with a cross.

8 Modelling of creep ductility

8.1 Experimental background

Originally it was proposed to use pure oxygen free high conductivity copper (Cu-OF) in the canisters. However, in test series at temperatures between 75 and 145°C, it was observed that the creep elongation was below 5% in several cases /5, 6/, see Figure 4-3. Such a low value is not adequate for safe operation of the canisters. To be able to extrapolate the results to longer times, tests were also performed at 180 to 250°C. In this case disaster struck. In many of the creep tests the rupture elongation was below 1% /9, 16/, Figure 4-6. This was totally unexpected. Although pure copper had been used as material in many creep investigations, none has reported such low elongation values. These very low elongation values are now termed *extra low creep ductility* (ELCD).

It was immediately decided to abandon Cu-OF as a canister material. Since pure copper alloyed with phosphorus had been used successfully for a number years in pressure vessel applications it was decided to try such a material instead. Traditional tough pit copper contains oxygen and with the presence of phosphorus this material can be welded. To minimise the risk of hydrogen embrittlement, an oxygen free variant was chosen. The amount of phosphorus is 30 to 100 ppm. This material is designated Cu-OFP.

Two test series with the designations 400 and 500 were performed at temperatures between 200 and 450°C. These high temperatures were selected, since it was believed that the risk for encountering low creep ductility was highest at these temperatures. The lowest rupture elongations observed was 13% /10/, see Figure 5-5 and Figure 5-6. Below 300°C, all values were above 30%.

To find out the origin of the extra low ductility (ELCD) in Cu-OF, the tested materials were studied metallographically. Two of the studied batches showed low ductility values but not a third one /16/, nor did a fourth batch tested later /18, 19/. The metallography is briefly described in /16/ and further analysis is reported in /26/. All studied specimens had failed in an intercrystalline manner even at temperatures as low as 75°C. Cavitation was found in all specimens. The extent varied however, even if ELCD was found. In Auger analysis it was found that sulphur aggregated at the grain boundaries, contributing to the embrittlement.

Korzhevyy et al. /52/ have proposed a mechanism for a reduced sulphide formation in the presence of phosphorus. However, cavitation and crack formation around sulphides have been observed also for Cu-OFP.

8.2 Cavity nucleation

More recently models for nucleation of growth of cavities during creep in copper have been developed /26/. These models seem to offer an explanation of the large difference in ductility behaviour between Cu-OF and Cu-OFP. These models will be summarised here.

Experimentally it has been found for many steels and nickel base alloys that the number of creep cavities formed is approximately proportional to the creep strain. For a survey, see Wu and Sandström /53/. The nucleation rate can be expressed as

$$\frac{dn}{dt} = B\dot{\epsilon}_{cr} \quad 8-1a$$

where B is a constant and $\dot{\epsilon}_{cr}$ the creep rate. This relation has also been observed for copper by Needham et al. /54/. There is fair consensus that creep cavities are formed by grain boundary sliding. The sliding distance s_d is related to the creep strain

$$s_d = C_s \epsilon_{cr} \quad 8-1b$$

where C_s is a constant. The grain boundaries are assumed to have N_{inh} randomly distributed ledges or other inhomogeneities per unit area. These inhomogeneities can for example be subgrain boundaries.

The basic assumption in the model is that the grain boundaries consist of two closely spaced layers and that cavities are nucleated when an inhomogeneity on one layer meets one on the other layer. The model is referred to as the double ledge model. It can be shown that this gives the nucleation rate.

$$\frac{dn}{dt} = C_s N_{inh}^{3/2} \dot{\epsilon}_{cr} \quad 8-2$$

As an order of magnitude estimate for copper at low temperatures, $C_s = 0.05 \mu\text{m}$ and $N_{inh}^0 = 1 \times 10^{14} \text{1/m}^2$ have been chosen, which gives $B = 5 \times 10^{13} \text{m}^2$. N_{inh}^0 is the constant part of N_{inh} , see below. It is interesting to compare the results for B to other materials, see Figure 8-1.

According to Figure 8-1, there is a direct relation between the nucleation constant and the creep rupture strain. For pure copper the creep elongation could be as low as 0.1% as pointed above. With a B -value of $5 \times 10^{13} \text{m}^2$ this is fully consistent with the results in Figure 8-1. It should be pointed out that the estimate of the B -value to $5 \times 10^{13} \text{m}^2$ was done before Figure 8-1 appeared.

Due to the increasing diffusion around the grain boundaries with increasing temperature, one can expect that some of the inhomogeneities are gradually washed out. The smallest inhomogeneities that can prevail can be estimated with the help of Einstein's equation for diffusion.

$$B = \frac{C_s}{\left(1/N_{inh}^0 + 2\delta D_{GB} t_{diff} / d\right)^{3/2}} \quad 8-3$$

where δD_{GB} is the grain boundary diffusion const, t_{diff} the time the diffusion takes place and d the grain size. Equation 8-1a was used by Danavas and Solomon in their modelling of creep cavitation in copper /55/. They determined the value of B by fitting to data from Raj at 750°C for a test with a rupture time of 328 h /56/. Using Raj's values gives $1.1 \times 10^6 \text{1/m}^2$. The value in /57/ determined from the cavity data was $B = 1.6 \times 10^6 \text{1/m}^2$. This demonstrates that the diffusion term in Equation 8-3 can describe the temperature dependence of B approximately over a wide range of temperatures.

8.3 Cavity growth

Growth of creep cavities can be either diffusion or strain controlled. For copper the estimates show that diffusion is the dominating process. There are many variants of models for diffusion controlled growth of creep cavities. Many papers in the literature have derived expressions for the growth. Beere has written an excellent review /58/. The following equation has been used.

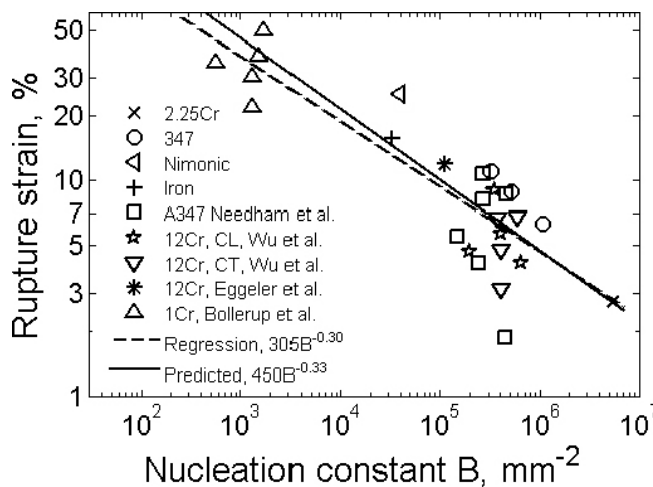


Figure 8-1. The relation between ductility and nucleation rate of cavities /57/.

$$\frac{dR}{dt} = \frac{3\delta D_{GB}\Omega}{k_B T} \frac{\sin^2 \theta}{\theta - \sin \theta \cos \theta} \frac{L^2}{R(L-2R)^3} \left(\sigma - \frac{\gamma_s \sin \theta}{R} \right) \quad 8-4$$

where δD_{GB} is the grain boundary diffusion coefficient, R the cavity radius in the grain boundary plane, Ω the atom volume, θ angle inside the cavity at the intersection with the grain boundary, L the cavity spacing, σ the applied stress, and γ_s the surface energy. Equation 8-4 has been used to model cavity growth in copper for example in /57/.

8.4 Rupture predictions

Grain boundary sliding plays an important role for both nucleation and growth of cavities. If the sliding is slowed down nucleation and growth rate will be reduced. It has been observed by electron microscopy that phosphorus can agglomerate to the grain boundaries. It is assumed that the interaction energy W between the phosphorus atoms and the grain boundary controls the concentration at the boundaries ($W < 0$).

$$c_{PGB} = c_{P0} e^{-\frac{W}{k_B T}} \quad 8-5$$

where c_{P0} is the average P-content in the copper and c_{PGB} is the concentration of P at the grain boundaries. An extra stress σ_{break} must be provided that is acting over the area b^2/c_{PGB} to move the boundary one Burgers vector b . This gives the energy balance

$$\sigma_{break} = \frac{2m}{b^3} E c_{P0} e^{-\frac{E}{k_B T}} \quad 8-6$$

where m is the Taylor factor. In the creep equations the applied stress is reduced by σ_{break} when calculating the nucleation and the growth rate for Cu-OFP.

When cavitation takes place a fraction A_{cav} of the grain boundaries area is no longer load carrying. The cavitated area fraction A_{cav} at time t can be derived approximately from the following equation.

$$\frac{dA_{cav}}{dt} = \frac{dn}{dt} \pi R^2(t) \quad 8-7$$

When the cavitated area fraction has reached a value of 25%, brittle creep rupture is assumed to take place. For ductile rupture the criterion that the creep strain is equal to 40% has been used. The type of rupture is controlled by the criterion that is met first.

The creep equations, see Chapter 9, are applied to find the stress that gives rupture after a given time. The resulting stresses for a rupture time of 10,000 h are shown in Figure 8-2 together with experimental data with a rupture time longer than 3,000 h. It can be seen that the rupture stress is predicted in a reasonable way.

Rupture elongation values at rupture have also been computed taking the failure criteria into account. The results are given in Figure 8-3. There is a minimum in the rupture elongation versus temperature for both materials. A much more pronounced minimum is observed for Cu-OF than for Cu-OFP. Furthermore, the minimum is found at lower temperatures for Cu-OF than for Cu-OFP. This is fully consistent with the experiments. For Cu-OFP the minimum is at slightly lower temperatures than in the experimental data. This demonstrates that the difference between the materials is underestimated rather than overestimated by the model.

The lowest content of phosphorus in SKB:s specification that is allowed is 30 ppm. It is therefore of interest to analyse how the rupture behaviour is affected by a reduced P-content. In Figure 8-4 the rupture elongation is given as function of temperature for 30 ppm P.

The minimum in the rupture elongation for Cu-OFP is more pronounced for 30 ppm P than for 50 ppm P. It is found at a slightly lower temperature, see Figure 8-4. It seems wise to keep the minimum content of 30 ppm P in the specification. If the P content is 80 ppm instead of 50 ppm, the ductility minimum for Cu-OFP disappears altogether.

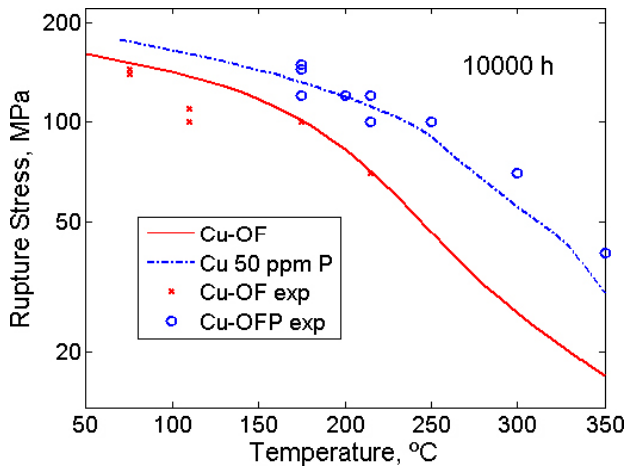


Figure 8-2. Stress that gives creep rupture after 10,000 h versus temperatures. Experimental data with rupture times exceeding 3,000 h are shown. Model values for 0 and 50 ppm P.

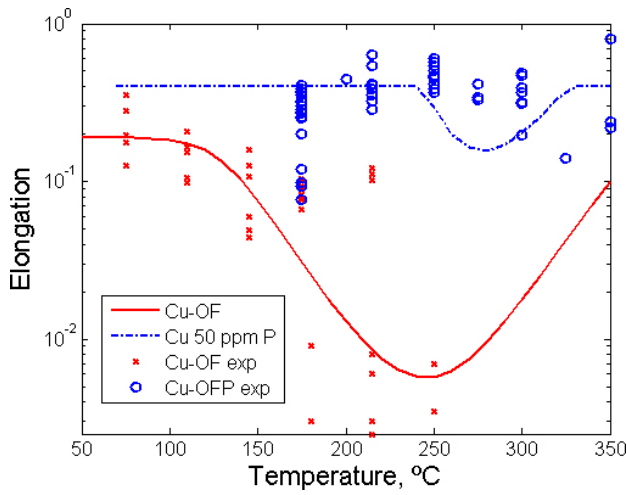


Figure 8-3. Creep elongation at rupture versus temperature for a rupture time of 10,000 h for Cu-OF and Cu-OFP. Measured creep elongation values are shown for comparison. Model values for 0 and 50 ppm P.

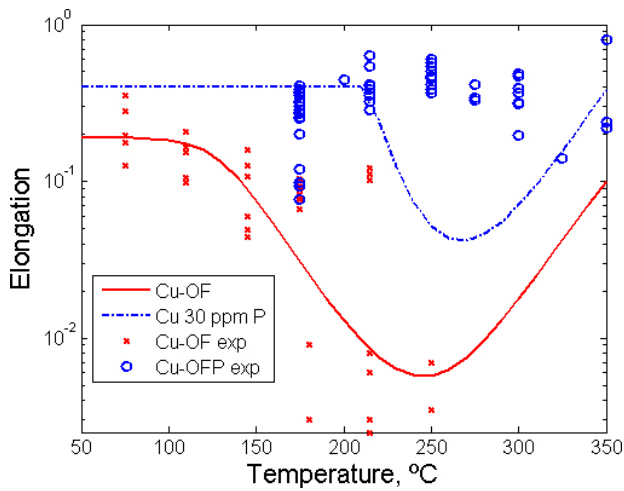


Figure 8-4. Same as Figure 8-3 with model values based on 0 and 30 ppm P.

All the calculated results above apply to a rupture time of 10,000 h, i.e. a little more than one year. In Figure 8-5 it is demonstrated how the creep elongation behaves at a very long rupture time of 1,000,000 h (114 years). Because of the extended extrapolation, Figure 8-5 should only be considered as tentative.

Comparing Figure 8-3 and Figure 8-5, the ductility minimum for Cu-OF has about the same depth but it is moved to lower temperatures. For Cu-OFP the depth of the ductility minimum is also fairly unchanged. It has also moved to lower temperatures. For even longer rupture times the ductility minimum vanishes altogether for Cu-OFP.

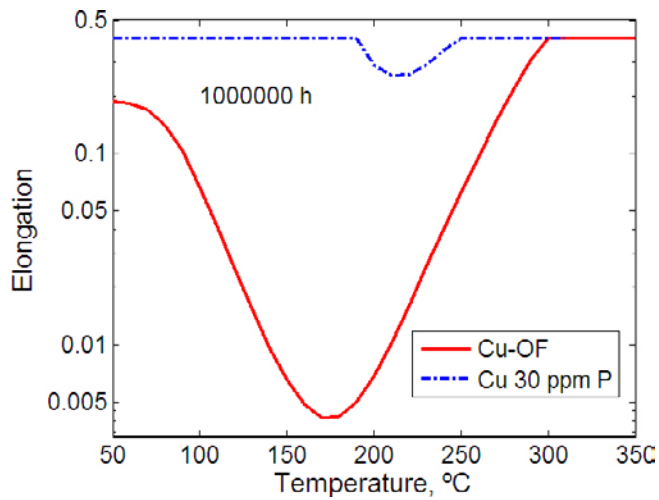


Figure 8-5. Creep elongation at rupture versus temperature for a rupture time of 1,000,000 h for Cu-OF and Cu-OFP. Model values with 30 ppm P.

9 Creep equations

9.1 Stationary state, Cu-OF

A model for the stationary creep rate has been developed /28/. This model will be summarised in the present chapter. At high temperatures above half the melting point T_m , climb is believed to controlling deformation mechanisms in many types of metals including copper. For copper $T_m/2 \approx 400^\circ\text{C}$. The climb velocity of dislocations v_{climb} can be expressed as

$$v_{\text{climb}} = M_{\text{climb}} b \sigma \quad 9-1$$

where b is Burgers vector, σ the stress, and M_{climb} the climb mobility. From the work of Hirth and Lothe, the following expression for M_{climb} can be derived /59/.

$$M_{\text{climb}} = \frac{D_s b}{k_B T} e^{\frac{\sigma b^3}{k_B T}} \quad 9-2$$

D_s is the self diffusion coefficient, k_B Boltzmann's constant, and T the absolute temperature. The change in dislocation density ρ with strain ϵ depends on work hardening, dynamic recovery, and static recovery. These contributions are represented by the right hand side of the equation below.

$$\frac{d\rho}{d\epsilon} = \frac{m}{bL} - 2\omega\rho - \frac{2}{\dot{\epsilon}} M_{\text{climb}} \tau_L \rho^2 \quad 9-3$$

τ_L is the dislocation line tension, L is the spurt distance for a released dislocation, and ω a constant. The dynamic recovery term $2\omega\rho$ is usually ignored at high temperatures. For stationary conditions, i.e. constant ρ , one finds that.

$$\dot{\epsilon} = \frac{2bc_L}{m} \frac{D_s b}{k_B T} e^{\frac{\sigma b^3}{k_B T}} \tau_L \rho^{3/2} \quad 9-4$$

In Equation 9-4 it has been assumed that L is related to the average distance between dislocations and can be expressed as where $c_L/\sqrt{\rho}$ is a constant. The dislocation density can be related to the stress

$$\sigma = \alpha G b \sqrt{\rho} \quad 9-5$$

where G is the shear modulus and α is a constant. Combining Equation 9-4 and Equation 9-5 shows that the creep rate behaves as σ^3 , i.e. the Norton exponent is 3. The exponential term has only a small influence. For copper above 400°C , Equation 9-4 gives approximately the correct creep rate.

It is believed that the deformation is glide controlled at lower temperatures. According to /60/ the strain rate due to glide of dislocations can be expressed as

$$\frac{d\epsilon}{dt} = f \sigma^2 e^{-\frac{Q}{RT} \left[1 - \left(\frac{\sigma}{\sigma_{i\text{max}}} \right)^{q_1} \right]^{q_2}} \quad 9-6$$

where Q is an activation energy, $\sigma_{i\text{max}}$ the maximum back stress, and f , q_1 and q_2 constants. $q_1 = 2$ and $q_2 = 1$ have been chosen previously in the literature for copper. A difficulty with Equation 9-6 is that the values of the other constants are not known. Equation 9-6 can hence not be used directly. However, there are some similarities between Equations 9-4 and 9-6. In /28/ the two equations are combined into a unified model.

$$\dot{\epsilon}_{OF} = \frac{2bc_L}{m} \frac{D_s b \tau_L}{k_B T} \left(\frac{\sigma}{\alpha G b} \right)^3 e^{\frac{\sigma b^3}{k_B T}} e^{-\frac{Q}{RT} \left[1 - \left(\frac{\sigma}{\sigma_{i\text{max}}} \right)^2 \right]} \quad 9-7$$

The values of all the parameters in Equation 9-7 are readily available /28/. Equation 9-7 is compared to experimental data in Figure 9-1.

Within about an order of magnitude in strain rate, there is an agreement between the model and the data. It should be noticed that there are no fitting parameters involved in the model.

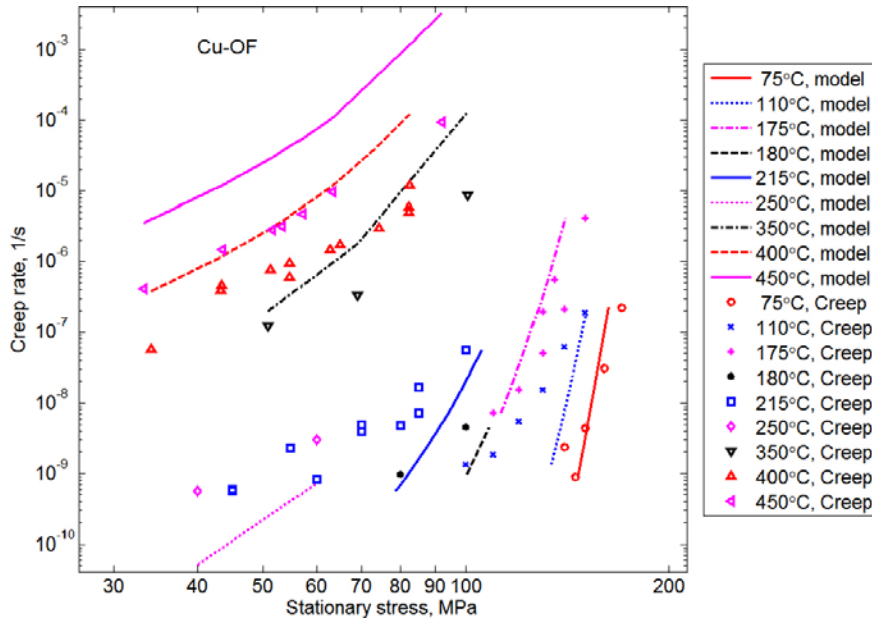


Figure 9-1. Comparison of Equation 9-7 to experimental data from /6/ and /37/ (>300°C). Cu-OF.

9.2 Stationary state, Cu-OF

In addition to improving the creep ductility, phosphorus raises the creep strength. The possible mechanisms behind this increase are analysed in /27/. It is concluded that the main mechanism is solute drag due to the agglomeration of phosphorus at the dislocations. The concentration of phosphorus at a dislocation c_{Pstat} where the effect of the motion is neglected, is given by /58/.

$$c_{Pstat} = c_{P0} e^{-\frac{W}{k_B T}} \quad 9-8$$

This is referred to as the static case. W is the interaction energy between a P-atom and the dislocation core ($W < 0$). c_{P0} is the P-content in the matrix. This equation is illustrated in Figure 9-2 for climbing and gliding dislocations.

A climbing dislocation is characterized by a trough in the solute concentration in front of the dislocation and a peak behind it, see Figure 9-2. Around a gliding dislocation there is a sharp concentration of solutes.

If the interaction between the dislocation and a solute is sufficiently large, a cloud of P atoms will follow the dislocations. It is referred to as a Cottrell atmosphere of solutes. For a moving dislocation Equation 9-8 is replaced by /58/

$$c_{Pdyn} = \frac{\nu c_{P0}}{D_P} \left(e^{-\frac{W(y)}{kT} - \frac{\nu y}{D_P}} \int_{-\infty}^y e^{\frac{W(y')}{kT} + \frac{\nu y'}{D_P}} dy' \right) \quad 9-9$$

where ν is the velocity of the dislocation. D_P is the diffusion coefficient for phosphorus. Using climb velocity in Equation 9-1, the values for P concentration c_{Pdyn} can be calculated, see Figure 9-2.

In comparison to the static solution both peaks and the troughs around the dislocations are more enhanced. The heights of the peaks are increasing with decreasing temperature.

In order that the dislocations should be able to move at a significant speed, they must break away from the solutes. The force on the dislocation segment of length $2L$ is $F = \sigma_{break} 2L b$. To move a dislocation one Burgers' vector the required energy is then $F b/2$. An energy balance gives the break away stress σ_{break}

$$\sigma_{break} L b^2 = |W| (1 - \sigma_{app} / \sigma_m) \quad 9-10$$

where L is the average distance between pinning solutes. When the tensile strength σ_m is reached, the break stress must vanish and this is taken into by the factor in brackets. The influence of L can be taken into account in the following way

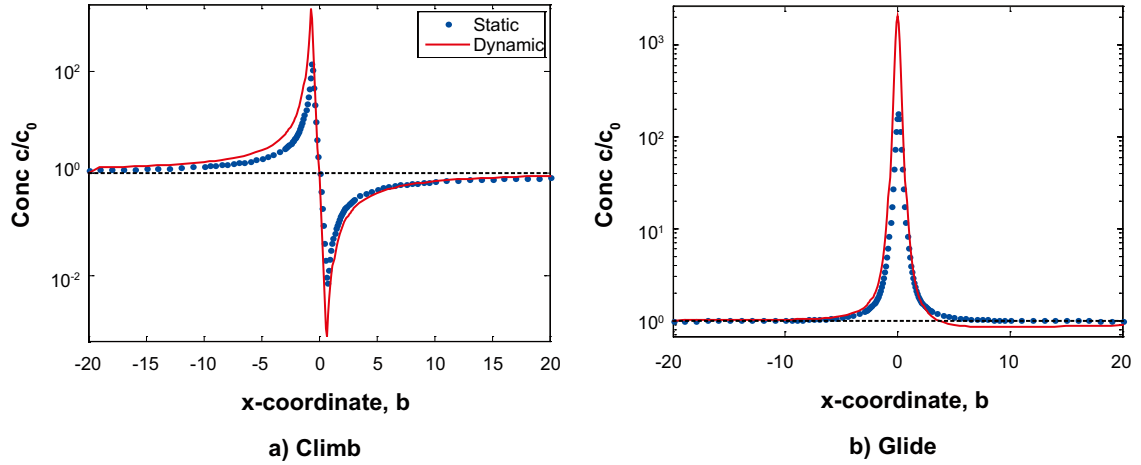


Figure 9-2. Concentration c/c_0 of P-atoms relative to the equilibrium value as a function of distance from a) a climbing dislocation moving in the horizontal direction and b) a gliding dislocation moving in the vertical direction. Static, non-moving dislocation. Dynamic, moving dislocation. 75°C.

$$\sigma_{\text{break}} = c_{P0} \frac{|W|}{b^3} (1 - \sigma_{\text{app}} / \sigma_m) \int_{y_L}^{y_R} c_{P\text{dyn}} dy \quad 9-11$$

where $c_{P\text{dyn}}$ is given by Equation 9-9. It is shown in /27/ that Equation 9-11 is consistent with experimental data and that the equation can explain the difference between Cu-OF and Cu-OFP. However, there is large scatter in the data. For computational purposes another approach has been chosen. The factor

$$\frac{-W}{e kT} \quad 9-12$$

can be assumed to be related to the ratio between the creep rates of Cu-OF and Cu-OFP. In the elastic approximation, the maximum value of W is given by /58/

$$W = -\frac{1}{2\pi} \frac{(1+\nu)}{(1-\nu)} G v_a \varepsilon_b \quad 9-13$$

where ν is Poisson's number and v_a the atomic volume. ε_b is the lattice misfit parameter which is 0.1651 for P in Cu /61/. Inserting values for Cu gives $W = -2.5 \times 10^{-20}$ J. A comparison to experimental data is made in Figure 9-3.

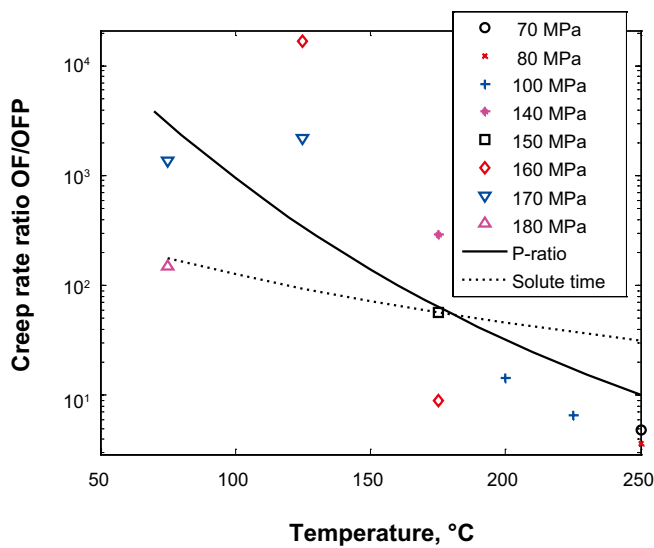


Figure 9-3. The ratio in creep rate between Cu-OF and Cu-OFP versus temperature. The experimental points are taken from /27/. The ratio marked solute time is that given by Equation 9-12. The curve marked P-ratio is the expression in Equation 9-14.

The ratio Equation 9-12 cannot fully represent the temperature dependence of the effect of phosphorus, which is an Arrhenius expression for the interaction energy between a solute and a dislocation. The temperature dependence in the model is lower than in the experiments. One reason could be that the energy W is based on elasticity, which is an approximation in the core region of the dislocation.

A fit to the observed values has also been made /27/. Since there are no data available below 75°C a cut-off is made at 75°C. The following equation was used.

$$f_P = \frac{\dot{\epsilon}_{OF}}{\dot{\epsilon}_{OFP}} = \begin{matrix} K_1 \exp(K_2 e^{-k_3 T}) & T > 348 K \\ K_0 & T \leq 348 K \end{matrix} \quad 9-14$$

where $K_0 = 3,000$, $K_1 = 0.1695$, $K_2 = 55.73$, and $k = 0.005 \text{ 1/}^\circ\text{C}$ are constants. In setting up Equation 9-14 it has also been made use of the fact that the creep rate ratio f_P is about unity at 400°C. This ratio is used together with Equation 9-7 to derive values for Cu-OFP. The computed strain rates are compared to experimental data in Figure 9-4.

A comparison at lower temperatures can also be found in Figure 7-3. In general an acceptable agreement is observed. This difficulty is in the transition between 175 and 215°C, where the experiments show a sharp transition in slope whereas the model transition is more gradual.

9.3 Primary creep, empirical model

One way of describing primary creep and creep during varying load is to replace the applied stress in Equation 9-7 with an effective stress σ_{eff} .

$$\sigma_{\text{eff}} = \sigma - \sigma_i \quad 9-15$$

where σ is the applied stress and σ_i an internal back stress. The back stress cannot be measured in an unambiguous way and has to be considered as a model quantity. The same basic model for the back stress is used as for the flow curves described in Chapter 9.

$$\sigma_i = C(1 - e^{-\omega \epsilon}) \quad 9-16$$

However, the back stress during creep is developing more slowly than the flow stress. Consequently, other parameter values have to be used. The constants C and ω have been fitted to slow strain rate data /17/. For C the value 257 MPa was obtained. For ω the following formula was used.

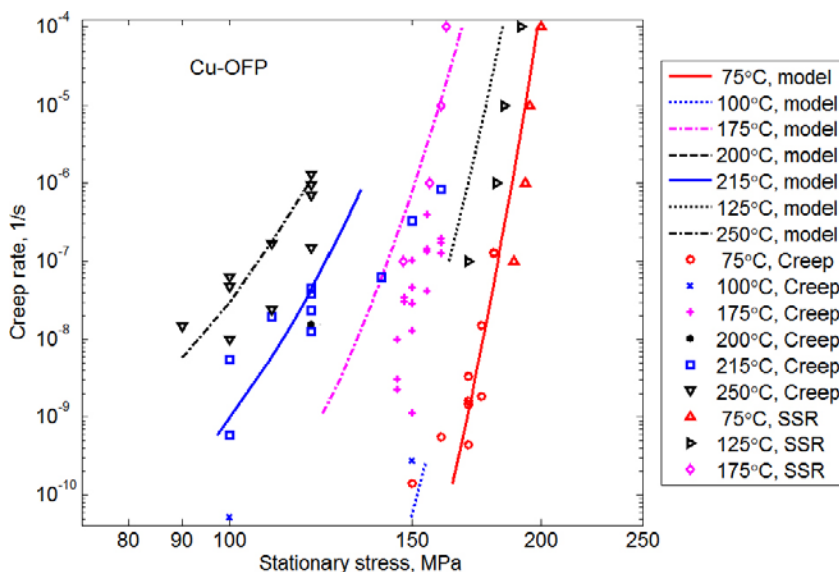


Figure 9-4. Comparison of Equation 9-7 including the ratio Equation 9-14 to creep data from /10, 18, 19/ and slow strain rate (SSR) data /17/. Cu-OFP.

$$\omega = \frac{B_b \dot{\epsilon}^{n_b}}{(T - 273)^{p_b}} \quad 9-17$$

B , n_b and p are constants that are determined by fitting to the stress strain curves. The following values were found: $B_b = 4.02$, $n_b = 0.0481$, and $p_b = 0.277$. A comparison to data is made in Figure 9-5.

Individual creep strain times curves can accurately be represented with the help of the ϕ -model /62/

$$\dot{\epsilon} = \phi_1 \epsilon_{prim}^{-\phi_2} \quad 9-18$$

$$\epsilon_{prim} = (\phi_1 (1 + \phi_2) t)^{1/(1+\phi_2)} \quad 9-19$$

where ϵ_{prim} is the primary creep strain, and ϕ_1 and ϕ_2 are constants. How the ϕ -model can be applied is illustrated in Figure 9-20.

The tertiary creep in Figure 9-20 is described with the Ω -model /64, 65/.

$$\frac{d\epsilon}{dt} = \Omega_3 e^{\Omega_4 \epsilon} \quad 9-20$$

where Ω_3 and Ω_4 are constants. For individual creep strain versus time curves for Cu-OF and Cu-OFP and many other materials can be modelled quite accurately with the ϕ and Ω -models. However, to make the ϕ -model predictive, the constants must be possible to describe with general relations. This is illustrated for ϕ_2 in Figure 9-7 /29/. The temperature dependence of this constant is shown.

There is large scatter between primary creep curves for most materials, and this also the case for Cu-OF and Cu-OFP. This is the main cause of the scatter in Figure 9-7. The ratio between the initial creep rate and the minimum creep rate $\dot{\epsilon}_{min}$ can be found from Equation 9-18.

$$g_{rate} = \frac{\dot{\epsilon}_{init}}{\dot{\epsilon}_{min}} = \left(\frac{\epsilon_{init}}{\epsilon_{min}} \right)^{-\phi_2} \quad 9-21$$

By combining the ratio in Equation 9-21 with Equation 9-7, an effective stress can be introduced in the latter equation. Using Equation 9-19 the strain ratio in Equation 9-11 can thus be formulated as.

$$\frac{\epsilon_{init}}{\epsilon_{min}} = \left(\frac{t_{init}}{t_{min}} \right)^{1/(1+\phi_2)} \quad 9-22$$

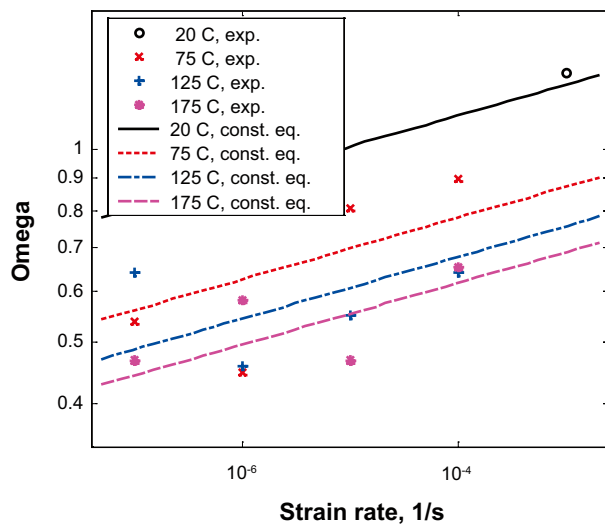


Figure 9-5. The ω -values according to Equation 9-17 versus strain rate are compared to data that have been determined for each tensile test.

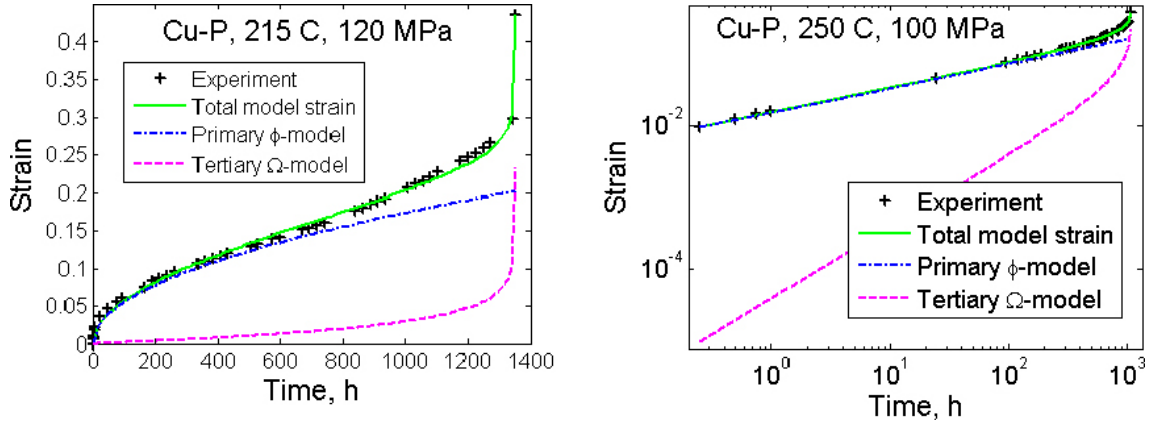


Figure 9-6. Two creep curves for Cu-OFP at 120 MPa, 215°C and 100 MPa, 250°C. The rupture times were 1,351 and 883 h. The primary creep is represented with the ϕ -model and the tertiary creep with the ϕ -model.

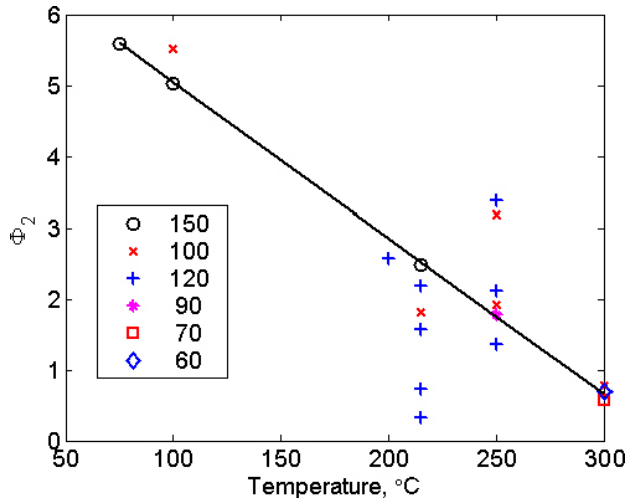


Figure 9-7. Constant ϕ_2 in Equation 9-19 versus temperature at stress levels from 60 to 150 MPa for Cu-OFP.

Inserting Equation 9-22 into Equation 9-11 gives.

$$g_{\text{rate}} = \left(\frac{t_{\text{min}}}{t_{\text{init}}} \right)^{\phi_2 / (1 + \phi_2)} \quad 9-23$$

This expression can now be combined with Equation 9-7 at the same time as σ is replaced by σ_{eff} .

$$\dot{\epsilon}_{\text{OFP}} = \frac{2bc_L}{m} \frac{D_s \phi b \tau_L}{k_B T} \left(\frac{\sigma_{\text{eff}}}{\alpha m G b} \right)^3 e^{\frac{\sigma_{\text{eff}} b^3}{k_B T}} e^{-\frac{Q_{\text{eff}}}{RT} \left[1 - \left(\frac{\sigma_{\text{eff}}}{\sigma_{\text{imax}}} \right)^2 \right]} g_{\text{rate}} / f_P \quad 9-24$$

The time ratio g_{rate} in Equation 9-23 is determined by assuming that $t_{\text{init}} \sim 1$ h and $t_{\text{min}} \sim t_R/3$ where t_R is the rupture time. Equation 9-24 has been used in the finite element modelling of copper canisters, see Chapter 12.

Equation 9-24 is the model for primary creep that together with the model in Equation 9-7 for secondary creep (including also the factor f_P) has been used in the finite element modelling of the canister, Chapters 10 and 11. If Equation 9-7 is used on its own it is referred to as the stationary model. If the sum of Equations 9-7 and 9-24 is used, it is referred to as the non-stationary model. The reason is that it can be employed to describe situations where the applied load varies with time.

9.4 Primary creep, fundamental model

In the same way as for the secondary creep rate it is of great value to have a fundamental model for primary creep in addition to the empirical one described in Chapter 9.3, where fitting to data is involved.

The starting point for the fundamental model is the model for flow stress curves presented in Chapter 7 and in /33/.

$$\sigma = \sigma_y + (\sigma_c - \sigma_y)(1 - e^{-\omega \epsilon}) \quad 9-25$$

where σ_y is the yield strength, σ_c the stress giving the same creep rate as in the tensile test and ω a constant. σ_c is computed from Equation 9-7 also taking phosphorus into account with the help of the factor f_p . For a given strain rate, σ_c is found by iteration. ω can be obtained from the following expression /33/:

$$\omega = \frac{m}{b} d_{\text{int}} \left(2 - \frac{1}{n_{\text{slip}}} \right) \quad 9-26$$

where m is the Taylor factor ($= 3.06$), d_{int} the interaction distance between dislocations ($= 2.5 b$) and n_{slip} the number of independent slip systems ($= 12$ for fcc-metals). The resulting value is $\omega = 14.66$. The creep stress σ_c is related to the strain rate $\dot{\epsilon}_c$ with the help of a Norton relation

$$\dot{\epsilon}_c = B \sigma_c^n \quad 9-27$$

where B and n are constants. The constants depend on the stress level. Combining Equations 9-25 and 9-27 gives

$$\dot{\epsilon}_c = B \left[\sigma_y e^{-\epsilon} + \frac{\sigma - \sigma_y e^{-\epsilon}}{1 - e^{-\omega \epsilon}} \right]^n \quad 9-28$$

The factor $e^{-\epsilon}$ is due to the fact that engineering stresses are assumed to be used in Equation 9-28 contrary to Equation 9-25 where true stresses are involved. Equation 9-28 can be applied to derive creep strain curves. Some features of the model are illustrated in Figure 9-8.

In fact the model gives the same rate versus time behaviour as in the ϕ -model, cf. Equation 9-22 as well as a similar rate versus strain behaviour, cf. Equation 9-21. This is precisely the desired appearance. Some examples of computed creep strain time curves are given in Figure 9-9.

As can be seen from Figure 9-9, both the fundamental and the empirical models can represent creep strain data in a reasonably accurate way.

The comparison between model and experiments is so far for specimens that have ruptured. The lowest stationary creep rate for these specimens is 3×10^{-11} 1/s. Ho has performed creep tests at much lower stresses. A comparison to some of his results can be found in Figures 9-10 to 9-13.

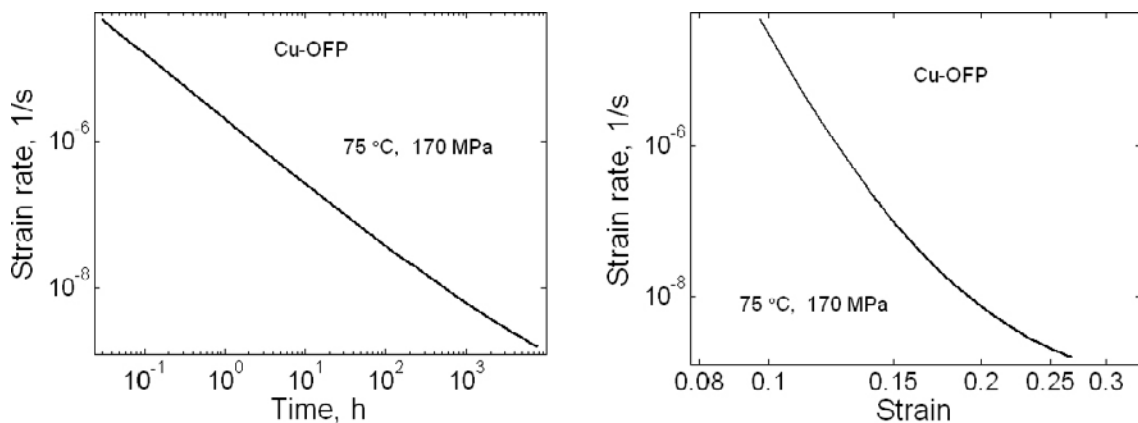


Figure 9-8. Creep strain rate versus a) time and b) strain for the model Equation 9-28.

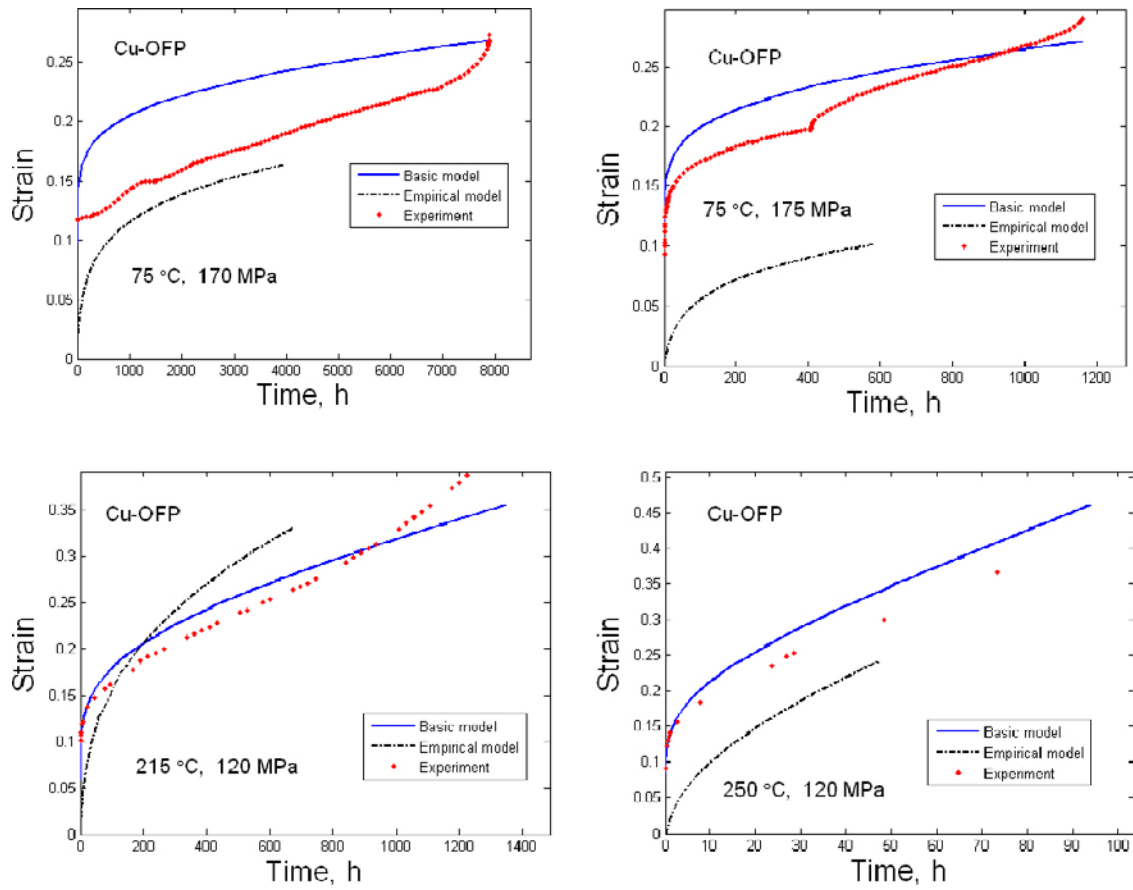


Figure 9-9. Creep strain versus time curves for Cu-OFP at 75, 215, and 250°C. The fundamental model Equation 9-28 and the empirical model Equation 9-24 are compared to experimental data.

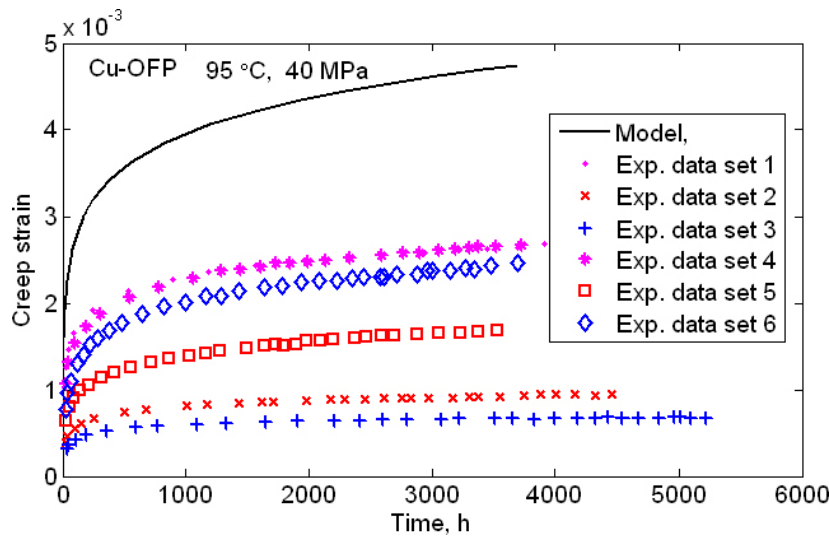


Figure 9-10. Creep strain versus time curves for Cu-OFP at 95°C, 40 MPa. The fundamental model Equation 9-28 is compared to experimental data from Ho /38/.

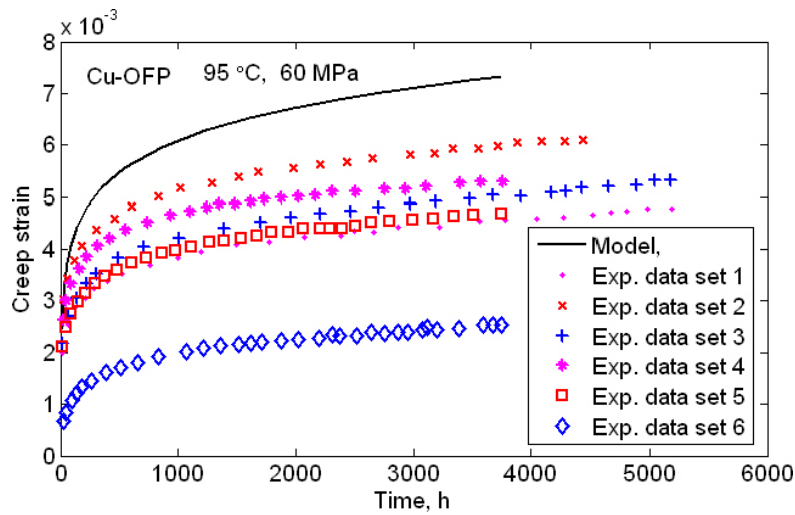


Figure 9-11. Creep strain versus time curves for Cu-OFP at 95°C, 60 MPa. The fundamental model Equation 9-28 is compared to experimental data from Ho /38/.

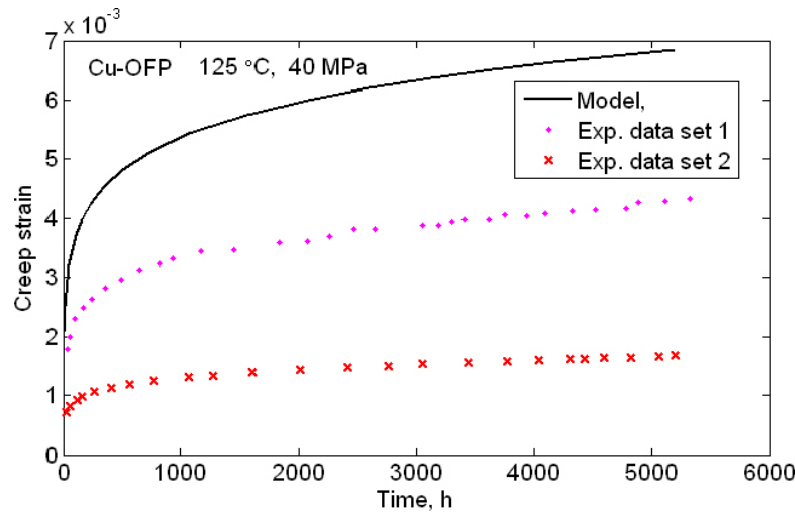


Figure 9-12. Creep strain versus time curves for Cu-OFP at 125°C, 40 MPa. The fundamental model Equation 9-28 is compared to experimental data from Ho /38/.

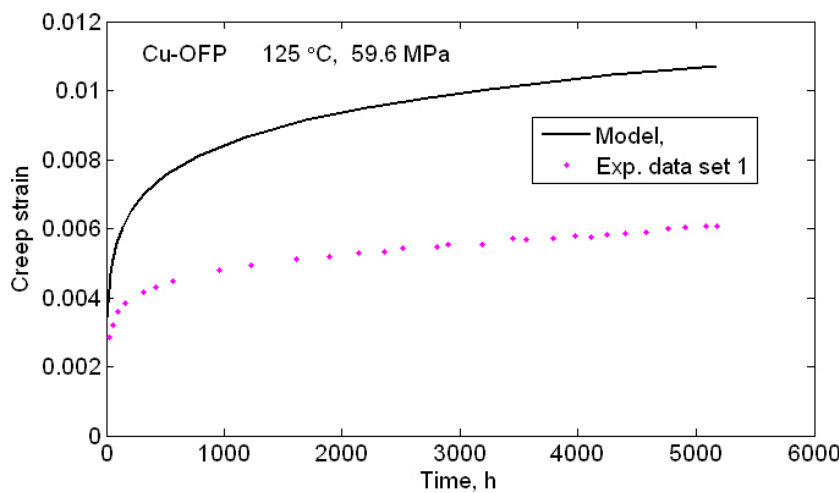


Figure 9-13. Creep strain versus time curves for Cu-OFP at 125°C, 60 MPa. The fundamental model Equation 9-28 is compared to experimental data from Ho /38/.

A distinct primary creep appears in these cases. The model gives somewhat higher strains than the experiments. All results are however within a factor of two of the experimental data.

The model results must be considered as quite satisfactory considering the wide range of stresses and strain rates involved. The estimated secondary creep rate is between 5×10^{-22} 1/s and 1.9×10^{-19} 1/s in Figures 9-10 to 9-13. This is more than ten orders of magnitude lower than for the ruptured specimens. This demonstrates that the model for primary creep is valid down to low stresses. The estimated secondary creep rates show that the creep deformation in Figures 9-10 to 9-13 is nowhere near reaching the secondary stage.

The estimated creep exponents in Figures 9-10 to 9-13 is 3 to 6. Thus, we are no longer in the power-law breakdown regime. This demonstrates again that the fundamental models presented in this survey can handle the transition from power-law breakdown to the power-law regime. The other verification was obtained by going to temperatures around 400°C. It can be concluded that the assumed climb and glide mechanisms can adequately represent the observed creep deformation.

9.5 Uncertainties in the constitutive equation for creep strain in Cu-OFP

9.5.1 Background

In /28/ and /29/ constitutive equations for creep in Cu-OFP were developed. Both a stationary and a non-stationary model have been presented above, Equations 9-7 and 9-24. The constitutive equations are unique in the sense that they cover the whole temperature range from power-law creep down to power-law breakdown. The stationary version has a fully fundamental basis except for the influence of phosphorus. Both the stationary and non-stationary models have been used to compute the creep deformation in copper canisters after emplacement in the depository, see Chapter 11. In the top and bottom of the canisters, creep is significant already at an early stage. The amount of creep is limited by the backing from the cast iron insert. With the non-stationary model the cylindrical gap is predicted to be closed in about 10 years, see Chapter 11.2.

The purpose of the present chapter is to illustrate how the uncertainties in the ingoing parameters in the model influence the primary and secondary creep rate.

9.5.2 Variation of parameters in the model

No parameters in the model Equation 9-24 are known with full certainty. The role of this uncertainty will now be analysed. It is natural to divide the parameters into three groups, see Table 9-1.

In the first category we have one fundamental constant and three physical property values that can be measured with high accuracy. In the second category there are material parameters that can be measured directly or evaluated with good precision. In the third category the values can still be determined accurately for individual experiments but there is considerable variation between tests.

The role of the parameter values in the first category will not be analysed here because the influence of uncertainties in their values is considerably smaller than for the other categories.

The ideal situation would be that the statistical variation of each parameter is known. With the possible exception of the maximum stress σ_{max} that is taken as the true tensile strength this is not the case. For the rest of the parameters the specified uncertainties in this paper are based on scientific judgment. For several of the parameters the value depends on the model used to assess the value, and in these cases the main uncertainty is in general in the choice of the evaluation models. The evaluation uncertainty is included in the specified value.

Table 9-1. Values of constants used in the model in Equation 9-24.

Category	Parameter description	Parameter	Value
Accurately known fundamental parameters	Burgers vector	b	2.56×10^{-10} m
	Taylor factor	m	3.06
	Boltzmann's constant	k_B	1.381×10^{-23} J/grad
	Shear modulus	G	$G = 4.75 \times 10^4 - 177$ MPa, T in K
Well established metallurgical parameters	Dislocation line tension	τ_L	7.94×10^{-16} MN at RT
	Coefficient for self diffusion	D_{s0}	1.31×10^{-5} m ² /s
	Activation energy for self diffusion	Q	198,000 J/mol
	Strain hardening constant	c_L	57
	Constant	α	0.19
	Max back stress	σ_{rmax}	257 MPa
Parameters that are more difficult to evaluate from experiments	Influence of phosphorus	f_P	3,000 for $T < 125^\circ\text{C}$
	Time at the start of primary creep	t_{init}	1 h
	Time at minimum creep rate	t_{min}	$t_R/3$ where t_R is the rupture time
	Parameter in g_{rate}	Φ_2	$13.26 - 0.0022T$, T in K
	Omega	ω	0.45

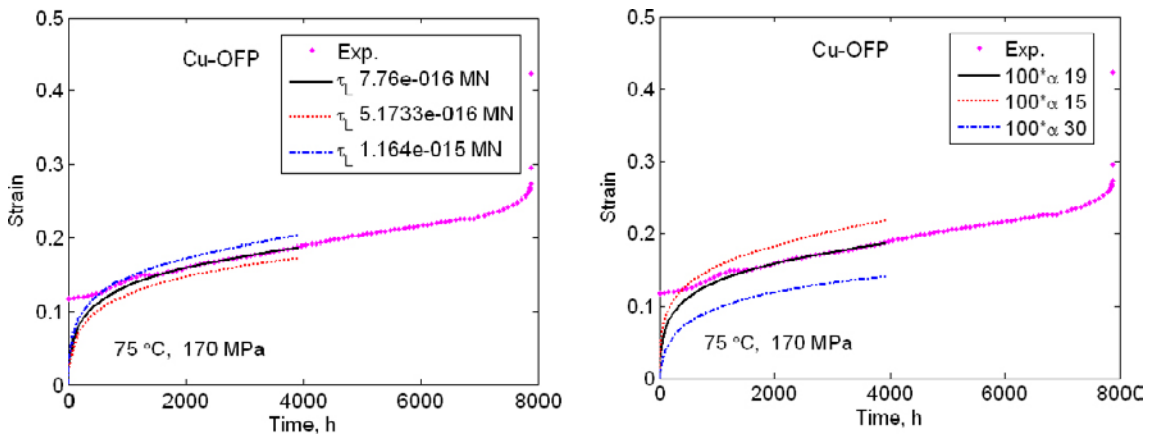


Figure 9-14. a) Influence of parameter values on a model creep curve. a) The dislocation line tension τ_L varied by a factor 1.5. b). Constant α varied from 0.15 to 0.30.

9.5.3 Parameters in the model for secondary creep

The first parameter to be studied is the dislocation line tension τ_L , see Figure 9-14a.

τ_L is given by the formula $Gb^2/3.5$. It is an average over edge and screw dislocations. It is the value in the denominator that varies between publications. The range of variation has been assumed to be a factor of 1.5. Throughout this report the effect of the variation in parameter value on a model creep curve will be illustrated. As a comparison the corresponding experimental creep curve for Cu-OFP is shown. The reference condition is 170 MPa at 75°C. It can be seen in Figure 9-14a that the influence of the uncertainty in τ_L on the creep curve is small.

The strength contribution from a dislocation network is proportional to α . The uncertainty in α is about the same as for τ_L . However, since α is raised to a power of 3, its influence is larger, see Figure 9-14b.

The creep rate in Equation 9-7 is directly proportional to the strain hardening constant c_L and the diffusion constant D_{s0} in the same way as for the dislocation line tension τ_L . Since the uncertainty in c_L and D_{s0} is estimated to be smaller than for τ_L they are not analysed further.

The role of the activation energy Q and the maximum stress $\sigma_{i\max}$ is illustrated in Figure 9-15.

$\sigma_{i\max}$ is taken as the tensile strength. Excellent measurements and ab-initio calculations of Q (and of D_{s0}) exist. The uncertainty in these parameters is thus small. However, since they appear in the exponent in Equation 4-1, they have still considerable influence on the creep rate, see Figure 9-15. The estimated uncertainties in these parameters can increase the creep strain by up to 40% or reduce it by 30%.

The influence of the phosphorus strengthening factor f_P is illustrated in Figure 9-16.

The value of the parameter f_P is somewhat uncertain since there is large scatter in the experimental data [27]. A variation by a factor of 2 has been assumed in Figure 9-16. In spite of the large variation the influence on the creep curve is limited.

9.5.4 Primary creep

The remainder of the parameters in Table 9-1 influences primary creep, i.e. the non-stationary part of the model. ω controls how fast the back stress increases with strain. The back stress is directly proportional to ω at low stress levels. In Figure 9-17a the role of ω is illustrated.

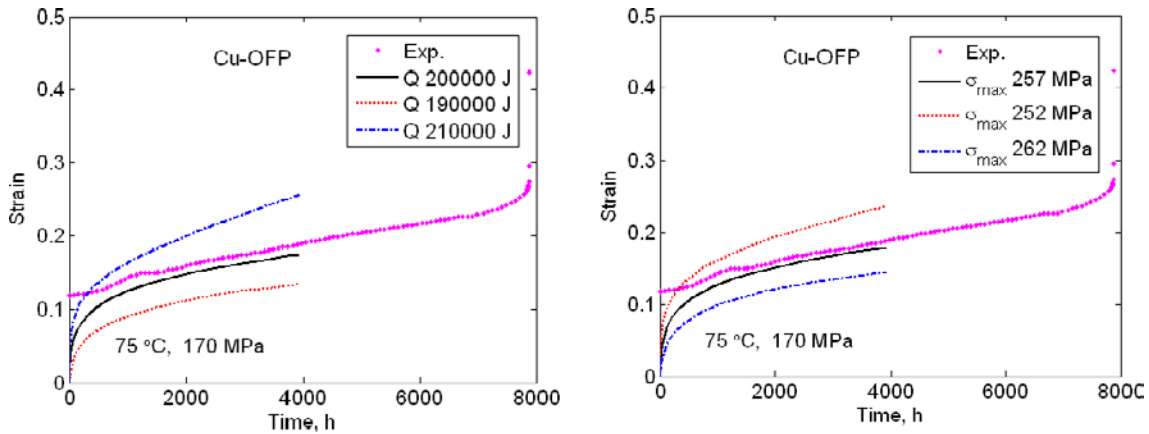


Figure 9-15. Influence of parameter values on a model creep curve. a) The activation energy Q is varied by $\pm 10,000$ J. b) The maximum stress $\sigma_{i\max}$ is varied by ± 5 MPa.

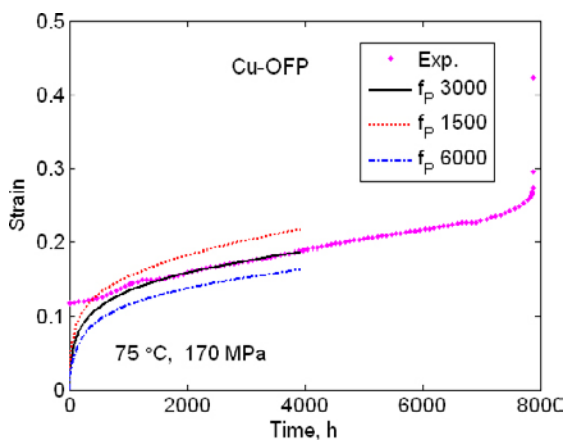


Figure 9-16. Influence of parameter values on a model creep curve. Phosphorus strengthening factor f_P is varied by a factor of 2.

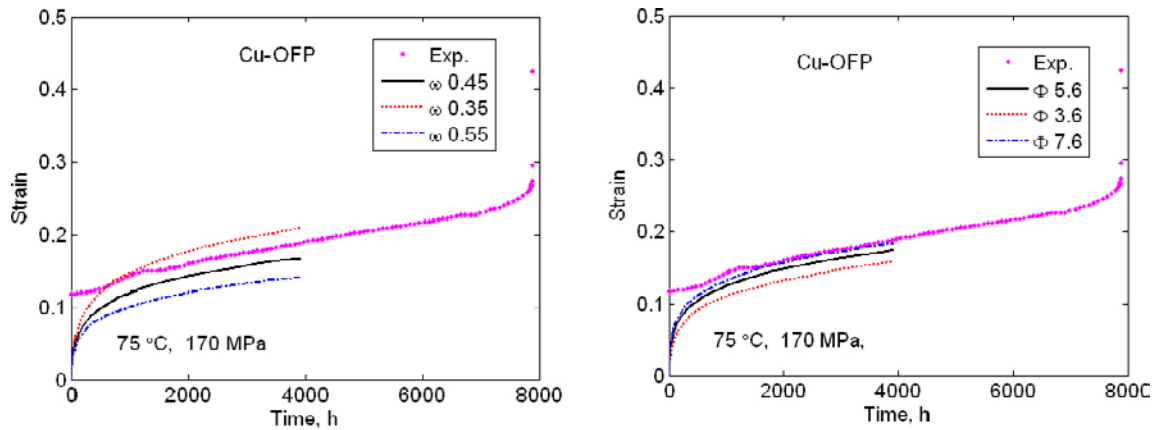


Figure 9-17. Influence of parameter values on a model creep curve. a) The constant ω is varied by ± 0.1 . b). The constant Φ_2 is varied by ± 2 .

The parameter Φ_2 and the two time constants t_{init} and t_{min} give how much faster the initial creep rate is than the minimum creep rate, see Equation 9-23. t_{init} is the time at the start of the primary creep and t_{min} the time at the minimum creep rate. In Figure 9-17b the role of Φ_2 is shown. The effect of the uncertainties in the time constants is illustrated in Figure 9-18.

Both time constants are difficult to estimate. However, their influence on the creep curve is modest.

9.5.5 Agglomerated effect

Of the analysed material parameters, the activation energy Q and the maximum stress σ_{imax} have the largest effect, in spite of the fact that the values of these parameters are well known. As pointed out above, the reason is that these two parameters appear in the exponent in Equation 9-24.

It seems that the influence of uncertainty in individual parameters is not larger than they can be accepted. What is the total effect of all the uncertainties? Since the statistical variation of the uncertainties is not known, the total effect cannot be determined directly in this way. The model gives however, an acceptable representation of creep curves at 75°C, see Chapter 9.4. The same is true for the maximum stress in slow rate tensile tests at 20 to 175°C /33/. None of these test sets were available when the model was developed.

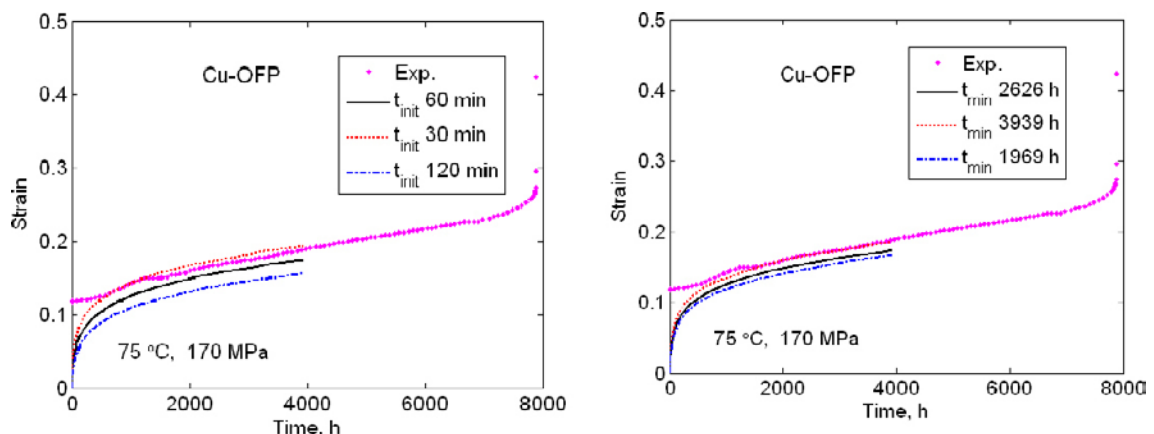


Figure 9-18. Influence of parameter values on a model creep curve. a) The time of the start of the primary creep t_{init} is varied by a factor of 2. b). The time at the minimum creep rate t_{min} is varied from about 2,000 to 4,000 h.

The total uncertainty can be estimated to a factor of five in the creep rate in the power-law breakdown regime and a factor of ten if higher temperatures are included as well [28]. This may seem to be very high values but it should be recalled that the model works in a wide range of temperatures and stress levels. The uncertainty in the fundamental model in Chapter 9.4 has not analysed yet but it is expected to be somewhat less than for Equation 9-24, in particular at higher temperatures and lower stresses.

It is also of interest to look at the influence of the external parameters, temperature T and applied stress σ . The importance of them is illustrated in Figure 9-19.

The temperature appears explicitly in Equation 9-24 but also in temperature dependent parameters such as G and τ_L . In spite of this, its influence is not dramatic. The effect of the applied stress is larger. This is not surprising since the effective creep exponent is quite high, about 65 at 75°C. The uncertainty in the creep model is about the same as the influence of the stress level in Figure 9-19b.

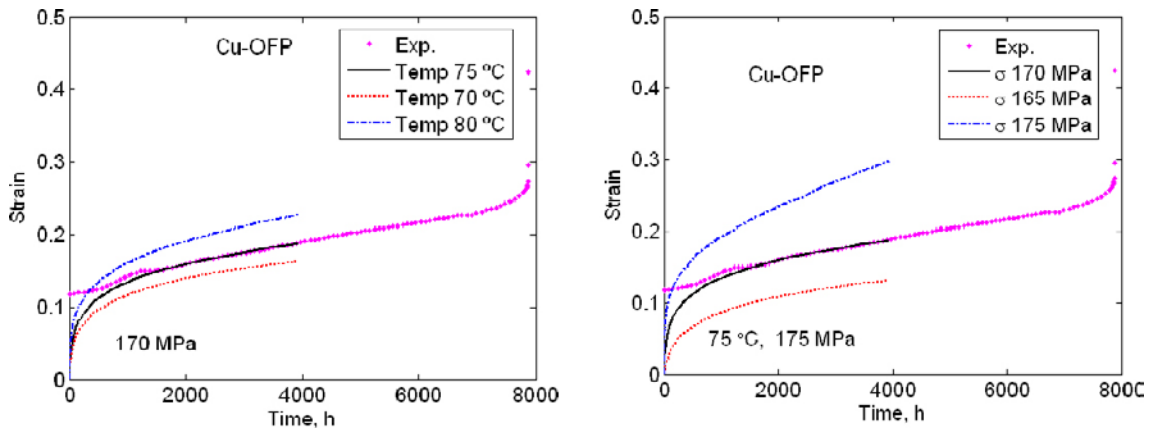


Figure 9-19. Influence of variation a) in temperature and b) in stress.

10 Constitutive equations

10.1 Background

According to the Swedish KBS-3 concept, waste from nuclear fuel elements are going to be put in packages and placed 500 m down in the bedrock. A 50 mm thick copper shell will be the outer part of the packages and provide corrosion protection. A cast iron insert inside the shell will be the load carrying part. A gap between the copper shell and the iron insert will ensure that the latter can be placed in the canister in a safe way. Pressure from the ground water and the swelling bentonite will cause the canister to creep until the gap between the canister and insert is closed.

In the repository temperatures of 75 to 100°C will be reached where creep in the canisters will take place. This is well inside the power-law breakdown regime with a creep exponent of 25 or more. Special constitutive equations for creep in Cu-OFP have been developed, Chapter 9.

10.2 Multiaxial models

The function in Equation 9-7 is the basis of the analysis. The effect of phosphorus with the help of the factor f_p is also taken into account. A simplified notation is introduced.

$$h(\sigma) = \frac{2bc_L}{m} \frac{D_{s0}b\tau_L}{k_B T} \left(\frac{\sigma}{\alpha m G b} \right)^3 e^{\frac{\sigma b^3}{k_B T}} e^{-\frac{Q}{RT} \left[1 - \left(\frac{\sigma}{\sigma_{i\max}} \right)^2 \right]} / f_p \quad 10-1$$

The stress σ in Equation 10-1 should be chosen as

$$\sigma = \sigma_{\text{true}} e^{-\varepsilon} \quad 10-2$$

where σ_{true} is the true stress and ε the effective creep strain. In slow strain rate tests at 20 to 175°C and in creep tests at the 75°C, the creep rate is governed by the technological stress, not the true stress [27, 49]. If the true stress would be used, which would seem natural, it would give an increase in the creep rate far beyond what is observed. This can be called retardation creep. It should be noticed that this is a substantial effect. All considered experimental data are in agreement with the effect. Thus the equation to be used in the stationary case is.

$$\dot{\varepsilon}_{\text{OFPstat}} = h(\sigma_{\text{true}} e^{-\varepsilon}) \quad 10-3$$

In the non-stationary case when the applied stress is allowed to vary, an effective stress is introduced, Chapter 9.3

$$\sigma_{\text{eff}} = (\sigma - \sigma_i) e^{-\varepsilon} \quad 10-4$$

The value of σ_i is given by Equation 9-16. The resulting expression for the strain rate is, Equation 9-24.

$$\dot{\varepsilon}_{\text{OFPinit}} = h((\sigma - \sigma_i) e^{-\varepsilon}) g_{\text{rate}} \quad 10-5$$

To represent both primary and secondary creep, Equation 10-3 for stationary creep is added.

$$\dot{\varepsilon}_{\text{OFPnon-stat}} = h((\sigma - \sigma_i) e^{-\varepsilon}) g_{\text{rate}} + h(\sigma e^{-\varepsilon}) \quad 10-6$$

The two terms in this equation take into account primary and secondary creep, respectively. To transfer the uniaxial expression Equation 10-6 to the multiaxial case, several approaches have been considered.

10.2.1 Approach A

The most straightforward approach is to replace the stress and strain in Equation 10-6 by the stress invariant and the effective strain, respectively.

$$\frac{d\varepsilon_{\text{eff}}^p}{dt} = h(J(\boldsymbol{\sigma}) e^{-\varepsilon_{\text{eff}}^p}) + h(J(\boldsymbol{\sigma} - \boldsymbol{\sigma}_i) e^{-\varepsilon_{\text{eff}}^p}) g_{\text{rate}} \quad 10-7$$

The stress invariant is given by

$$J(\boldsymbol{\sigma} - \boldsymbol{\sigma}_i) = \sqrt{\frac{3}{2}(\boldsymbol{\sigma}' - \boldsymbol{\sigma}_i') : (\boldsymbol{\sigma}' - \boldsymbol{\sigma}_i')} \quad 10-8$$

$\boldsymbol{\sigma}'$ and $\boldsymbol{\sigma}_i'$ are the deviatoric part of the stress and back stress tensor $\boldsymbol{\sigma}$ and $\boldsymbol{\sigma}_i$, respectively. The individual components of the creep rate are derived with Odqvist's equation.

$$\frac{d\boldsymbol{\varepsilon}^P}{dt} = \frac{3}{2} \frac{d\varepsilon_{\text{eff}}^P}{dt} \frac{\boldsymbol{\sigma}' - \boldsymbol{\sigma}_i'}{J(\boldsymbol{\sigma} - \boldsymbol{\sigma}_i)} \quad 10-9$$

Earlier the back stress was derived by Armstrong-Frederick equation /63/.

$$\frac{d\boldsymbol{\sigma}_i}{dt} = \frac{2}{3} a_k \frac{d\boldsymbol{\varepsilon}^P}{dt} - c_k \boldsymbol{\sigma}_i \frac{d\varepsilon_{\text{eff}}^P}{dt} \quad 10-10$$

However, this equation does not work well even for a uniaxial tensile test /63, 31/. To solve this problem the Armstrong- Frederick's formula was replaced by the following equation where the derivatives are taken with respect to the effective strain /63, 31/.

$$\frac{d\boldsymbol{\sigma}_i'}{d\varepsilon_{\text{eff}}^P} = \frac{2}{3} a_k \frac{d\boldsymbol{\varepsilon}^P}{d\varepsilon_{\text{eff}}^P} - c_k \boldsymbol{\sigma}_i' \quad 10-11$$

In Equation 10-11 the stresses have been replaced by the stress deviators. This is the same equation as in the uniaxial case provided $a_k = \omega C$ and $c_k = \omega$. It is possible to integrate Equation 10-11 in approximate way since a_k and c_k are constant and $\frac{d\boldsymbol{\varepsilon}^P}{d\varepsilon_{\text{eff}}^P}$ varies slowly with strain. The result is:

$$\boldsymbol{\sigma}_i' = \boldsymbol{\sigma}_i'(\varepsilon_{\text{eff}0}^P) e^{c_k(\varepsilon_{\text{eff}}^P - \varepsilon_{\text{eff}0}^P)} + \frac{2}{3} \frac{a_k}{c_k} \frac{d\boldsymbol{\varepsilon}^P}{d\varepsilon_{\text{eff}}^P} (\varepsilon_{\text{eff}}^P) (1 - e^{c_k(\varepsilon_{\text{eff}}^P - \varepsilon_{\text{eff}0}^P)}) \quad 10-12$$

10.2.2 Approach B

Another way is used to replace the expression for the effective creep rate Equation 10-7 by the following relation.

$$\frac{d\varepsilon_{\text{eff}}^P}{dt} = h(\boldsymbol{\sigma}_e e^{-\varepsilon_{\text{eff}}^P}) + h((\boldsymbol{\sigma}_e - \boldsymbol{\sigma}_i) e^{-\varepsilon_{\text{eff}}^P}) g_{\text{rate}} \quad 10-13$$

The effective stress $\boldsymbol{\sigma}_e$ is applied in Equation 10-13.

$$\boldsymbol{\sigma}_e = \sqrt{\frac{3}{2} \boldsymbol{\sigma}' : \boldsymbol{\sigma}'} \quad 10-14$$

$\boldsymbol{\sigma}'$ is the deviatoric part of the stress tensor $\boldsymbol{\sigma}$. With the help of Odqvist's equation, the individual components of the creep rate are obtained.

$$\frac{d\boldsymbol{\varepsilon}^P}{dt} = \frac{3}{2} \frac{d\varepsilon_{\text{eff}}^P}{dt} \frac{\boldsymbol{\sigma}'}{\boldsymbol{\sigma}_e} \quad 10-15$$

The back stress is now a scalar. It can be derived from the following equation, again identifying the analogue with the uniaxial case

$$\frac{d\boldsymbol{\sigma}_i}{d\varepsilon_{\text{eff}}^P} = \omega(C - \boldsymbol{\sigma}_i) \quad 10-16$$

If ω and C are constant, Equation 10-16 can be integrated

$$\boldsymbol{\sigma}_i = C(1 - e^{-\omega\varepsilon_{\text{eff}}^P}) \quad 10-17$$

The problem with the Armstrong – Frederick equation is avoided in this way.

The models in Equations 10-7, 10-12 and 10-15 have been compared with experimental uniaxial creep curves in the same way as in Figure 9-9. Identical results are obtained, which are the same as in Figure 9-9.

10.3 Notched specimens

One well known method to introduce multiaxial stresses in specimens is to use notched bars exposed to an axial tensile load. Such specimens can be investigated in the same test machines as uniaxial specimens. By changing the notch profile, various states of stress can be obtained. The test specimens used are shown in Figure 10-1 /64/.

The rupture time of the notched specimens is illustrated in Figure 10-2. The stresses are net section stresses across the notched waists.

The creep lifetime under multiaxial stresses is much longer than that for uniaxial specimens. This demonstrates notch strengthening for the Cu-OFP material. If the rupture curves are extrapolated, the notch strengthening factor in time is greater than 100. Metallography has shown that only limited number of pores and cavities are observed in ruptured specimens. This shows that the local creep ductility is high.

Comparison to finite element modelling (FEM) is illustrated in Figure 10-3. The material models in Chapters 9.3 and 9.4 are used.

Using the fundamental model (Equation 9-28) the observed strain are somewhat overestimated. In particular the initial strain is overestimated. With the climb-glide model, Equation 9-24, on the other hand the strains are underestimated by a factor of three. Considering that the time difference to the uniaxial test results is more than a factor of 100, the comparison between the experiments and the simulation must be considered as satisfactory.

Creep crack growth tests have been performed for Cu-OFP /11, 23, 40/. Creep crack growth has been observed at test temperatures of 175°C and above, but not at lower temperatures. Extensive blunting of the notch can increase the notch radius by up to a factor of 20, which prohibits crack growth. Plastic deformation of the whole specimen also outside the notch, makes it quite difficult to interpret the test results.

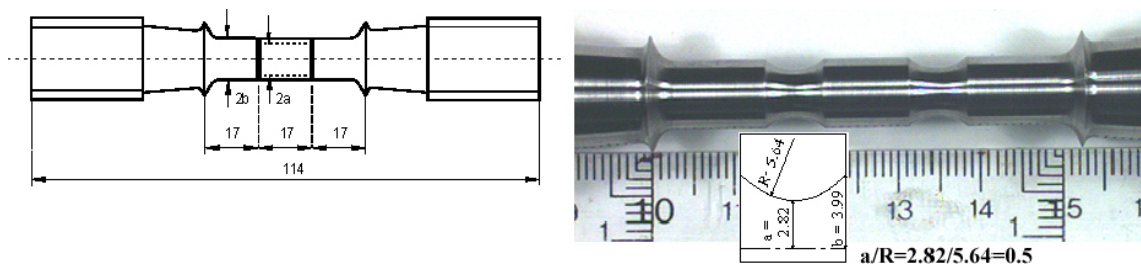


Figure 10-1. Double notched cylindrical creep specimen. a) drawing, and b) picture. The specimen has a notch acuity of 0.5. The specimen diameter is 8 mm in the gauge length and the gauge length is 51 mm.

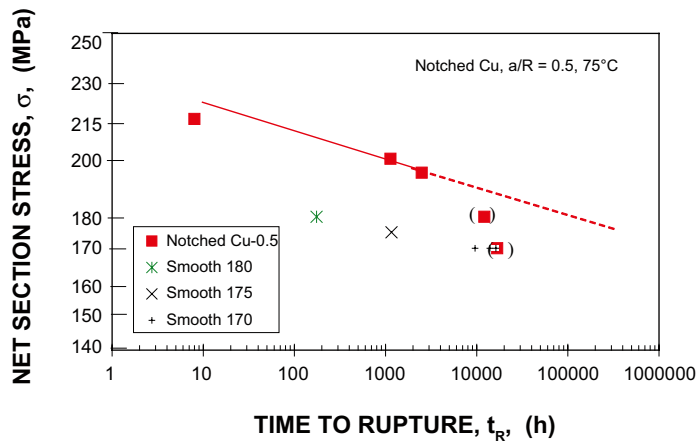


Figure 10-2. Influence of net section stress on the creep lifetime for notched specimens at 75°C. Tests at 170 MPa and 180 MPa were interrupted, which is indicated by brackets. Uniaxial results for smooth specimens are included for comparison /36/.

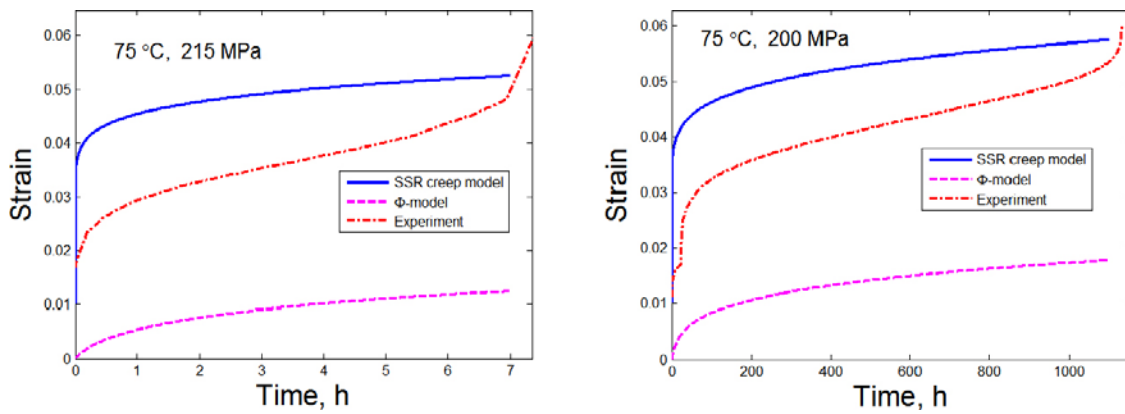


Figure 10-3. Comparison between experimental data and FEM results for a notched creep specimen under a net section stress a) 215 MPa and b) 200 MPa. For the model marked SSR creep, the fundamental model in Equation 9-28 was used for primary and secondary creep. For the curves marked Φ -model, Equation 9-24 was used. The initial strain on loading is included in the experimental data /36/.

11 Creep deformation in canister

11.1 Modelling parameters

A copper canister for the disposal of nuclear waste according to the KBS-3 concept is studied. The canister is illustrated in Figure 11-1. The canister is planned to be made of Cu-OFP. The nuclear fuel waste is placed in a cast iron insert that is put in the canister. The canister is exposed to an external pressure of 15 MPa at a temperature of about 348 K after the disposal. These conditions have been simulated with FEM-modelling. The material model used is the one given by Equation 9-24. For the translation to multiaxial stresses, Equation 10-12 was employed.

The outer dimensions of cast iron inserts are somewhat smaller than the inner dimensions of the canisters to allow for safe assembly. The differences are 5 and 3.5 mm in the axial and in the radial directions. The lid and the bottom of canister can be described as clamped disks. When the external pressure is applied, inward deflection occurs. For the cylindrical part of the canister an inward deformation will also take place except at the lid and the bottom. The canister becomes slightly hourglass shaped.

When sufficient plastic deformation has taken place the canister will get in contact with insert at the lid and bottom as well as along the cylindrical part. To represent the contact between the canister and the insert, the penalty-barrier method is used [65]. According to this method, non-linear springs connect the surfaces, giving additional stiffness. During non-contact, this stiffness is low and has little effect on the deformation. At predefined distances between the contacting surfaces the springs are activated and resist further closure. The contact stress σ_n is formulated as

$$\sigma_n = \begin{cases} \kappa_n - e_n \cdot g & g < 0 \\ \kappa_n \cdot \exp(-g \cdot e_n / \kappa_n) & g \geq 0 \end{cases} \quad 11-1$$

where k_n is the input estimate of the normal stress, e_n the penalty stiffness, and g the gap between the canister and the insert. The parameters k_n and e_n for a given gap are estimated by multiple finite element static computations, and then finely adjusted with the creep model. The applied values for normal stress and penalty stiffness are given in Table 11-1.

A commercial software Comsol Multiphysics is used for the FEM-modelling. Generalised Neumann conditions are used on all free boundaries. To solve the Navier's and ordinary differential equations, a time-dependent linear solver is applied. All forces on the boundaries are raised from zero to the specified value within a time interval of 0.1 s. The mesh consisted of 4,956 Lagrange quartic elements. Small steps of displacement are used in the computation. The absolute tolerance is set to about 10^{-14} , and the relative tolerance to 10^{-10} .



Figure 11-1. Copper canister and cast iron insert. The canister is 4,835 mm long, 1,050 mm in diameter and 50 mm in wall thickness.

Table 11-1. Contact parameters.

Boundary	Inner lid	Inner bottom	Inner wall
Gap, m	2.52×10^{-3}	2.48×10^{-3}	1.75×10^{-3}
Normal stress, MPa	87.5	82.5	7.0
Penalty stiffness, GPa m ⁻¹	8,000	8,000	8,000

11.2 Deformations in the canister

The equivalent stress (von Mises stress) as a function of radius in the cylindrical wall is illustrated in Figure 11-2 at different times. Initially there is a linear elastic stress distribution. Since the stresses are much higher at the inner than at the outer radius, the creep rate is much higher at the former position, Figure 11-3. As a consequence a stress redistribution takes place. After about 1×10^8 s (about 3 years), the stress distribution is more or less horizontal. This is a result of the high creep exponent $n = 65$. For a detailed discussion, see /30/. This can be considered as a space stationary state. Once the cylindrical part of the canister is in contact with the insert, the stress drops.

Since the creep rate is primarily controlled by the effective stress, there is no surprise that the general behaviour of the strain rate is much the same as that of the stress, Figure 11-3. A horizontal strain rate distribution is reached after 1×10^8 s and the strain rate begins to drop at 3×10^8 s (10 years).

In Figure 11-4 the displacements in the radial direction along the length of the cylindrical wall are shown. Initially an elasto-plastic deformation takes place. After 10^7 s creep deformation starts to appear. Not until 1×10^8 s there is any significant displacement due to creep. After 3×10^8 s contact has occurred with the insert along most of its length and the creep deformation is essentially complete. The creep strain is then 0.27% at the inside and 0.21% at the outside of the wall.

The displacements in the lid and the bottom at different times are shown in Figure 11-5 and Figure 11-6. Elasto-plastic deformation takes place directly on loading and represents the major part of the straining. The deflection at the centres of the lid and bottom immediately get in contact with the insert, reaching the specified maximum values. Only after about 1×10^8 s some creep deformation appears. There is a slight continuous creep due to the rotation of the corners of the canisters, which will be discussed below.

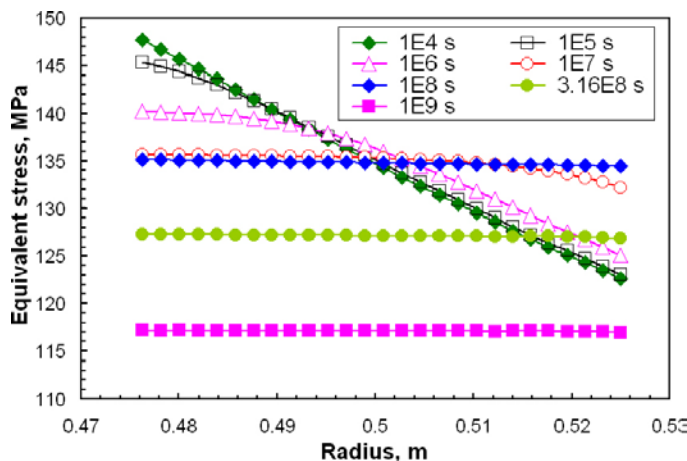


Figure 11-2. Equivalent stresses across the wall of canister shell in r direction at times between 10^4 and 10^9 s.

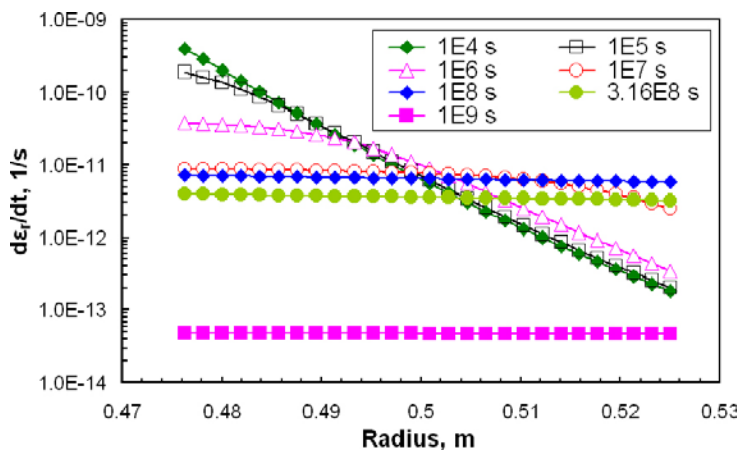


Figure 11-3. Creep rates across the wall of canister shell in r direction at times between 10^4 and 10^9 s.

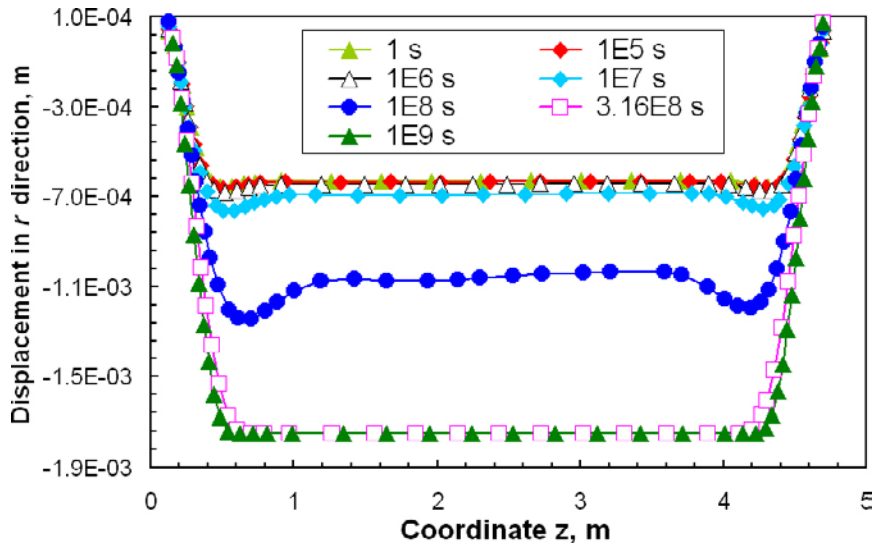


Figure 11-4. Displacements for the inner wall of canister shell in the radial direction at times between 1 and 10^9 s.

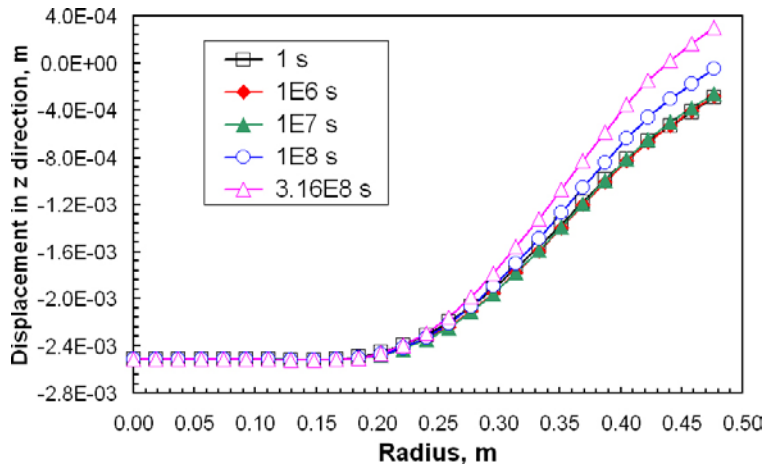


Figure 11-5. Displacements of inner side of lid in the axial direction at times between 1 and 3.16×10^8 s.

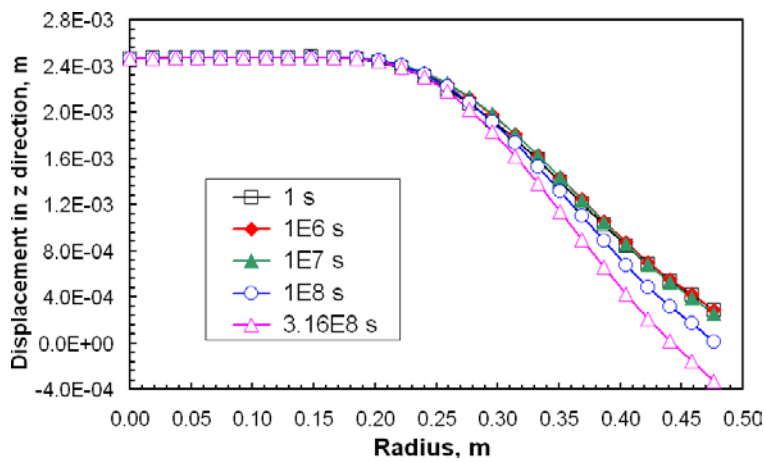


Figure 11-6. Displacements of inner side of bottom in z direction at times between 1 and s.

The magnitude of the displacements remains limited due to the contact with the cast insert at the lid and bottom and along the cylindrical wall.

In Figure 11-7 the total displacements after creep are shown. The largest displacements are observed at the centre of the lid and the bottom.

Equivalent stress distributions are illustrated in Figure 11-8. The stresses are largest at the corners. The maximum stresses are 145 MPa. In comparison to the “stationary” stress of 135 MPa in the cylindrical wall, this may seem to be a modest increase. However, the high stress exponent is of 65 has the consequence that significant creep strains are generated.

The maximum creep strains appear at the corners. These strains are given as a function of time in Figure 11-9. After 3.16×10^8 s the maximum strain is 12%.

The magnitude of the creep strain in Figure 11-9 are considerably larger than in cylindrical wall, which is 0.27% at the inside and 0.21% at the outside of the wall as mentioned above.

At the corners there are initially very large stresses, see Figure 11-10. They are due to the presence of bending moments. Consequently the creep strains are large. A rapid relaxation of these stresses takes place. The maximum stress is reduced linearly with the logarithm of time. If this behaviour continues the contribution to the strain decreases by more than a factor of 10 for each extra decade in time. The contribution for much longer times than in Figure 11-9 and Figure 11-10 can therefore be expected to be small.

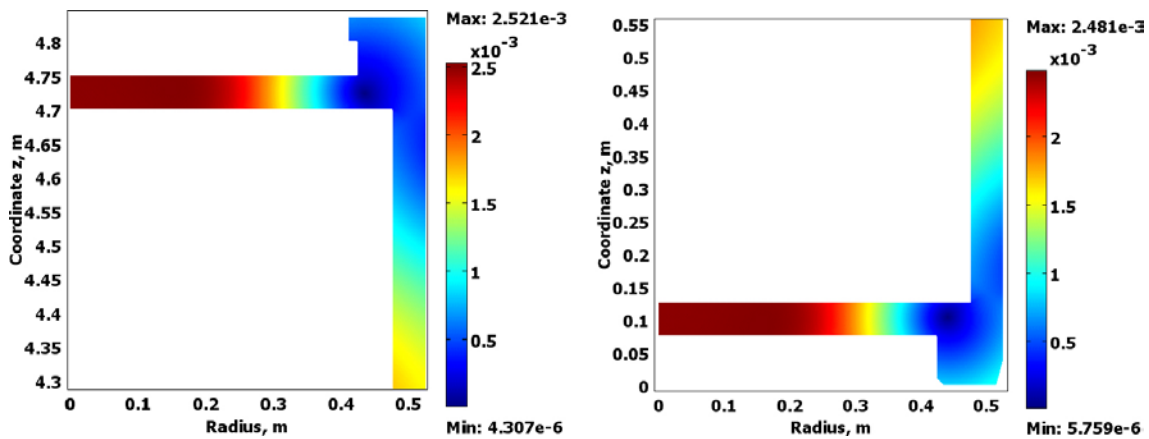


Figure 11-7. Total displacement in metre in upper and lower corners of canister shell under outer pressure of 15MPa and at time 3.16×10^8 s.

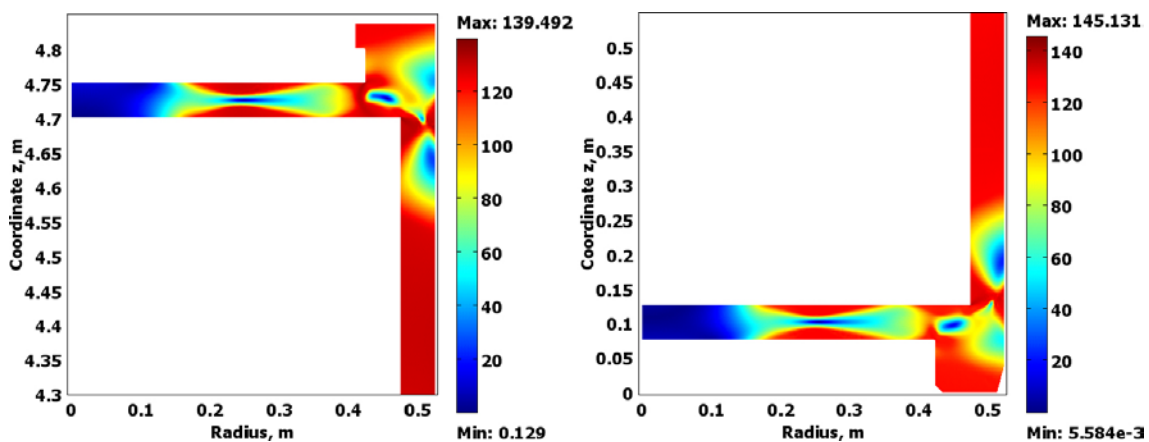


Figure 11-8. Equivalent stress distribution in MPa in upper and lower corners of canister shell under outer pressure of 15MPa and at time 3.16×10^8 s.

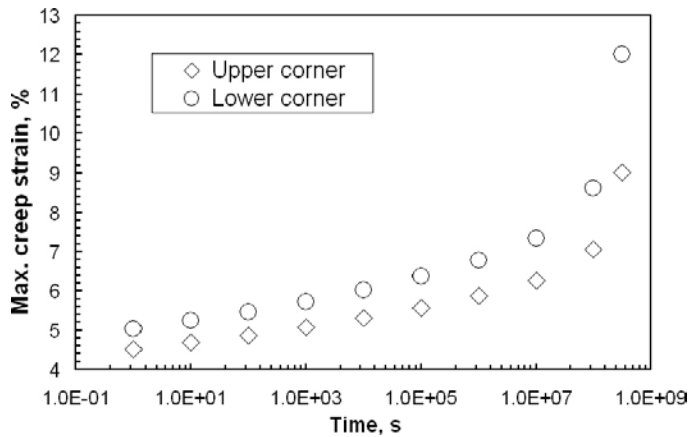


Figure 11-9. Maximum equivalent creep strain at inner corners.

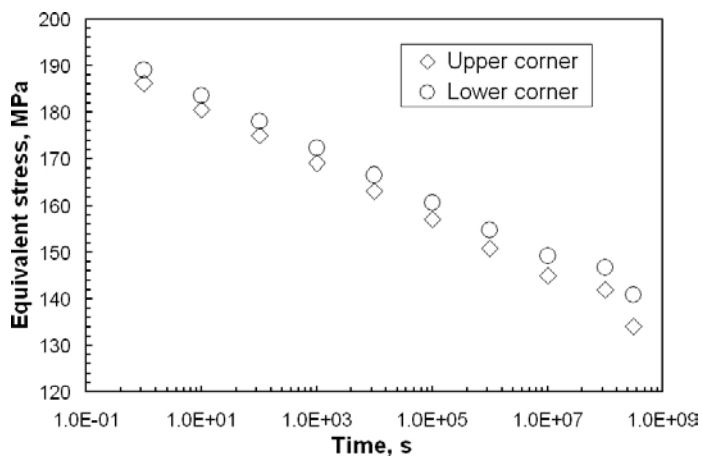


Figure 11-10. Equivalent stress at corners as a function of time.

In previous analysis the constitutive equations only took secondary creep into account /30/. In that analysis the time to close the gap between canister and insert was several order of magnitude larger than in the analysis presented here. It demonstrates that primary creep plays an important role.

For the climb-glide model, Equation 9-24, the creep rate is reduced approximately by an order of magnitude if the temperature is decreased by 10°C. Thus if the temperature in the copper is 65°C rather than 75°C, the gap along the cylindrical wall will be closed after 3×10^9 s, i.e. 100 years. On the other hand if the temperature is 85°C, the gap will be closed already after one year after full load has been applied.

11.3 Stresses and strains in slits and their role in copper canister integrity

In the copper canisters, slits exist between the cylinder and the lid as well as between the cylinder and bottom after welding. They cannot be avoided due to the manufacture tolerances. When the copper canister is loaded, these slits may contact each other and close, giving rise to stress concentrations. The slits have not been taken into account in the computations presented above. In this Chapter the stresses and strains in these slits will be analysed.

A displacement-controlled elasto-plastic model is used. The material model is the one presented in Chapter 10. The simulated geometry of the copper canister and the enlarged views of slits in the upper and lower corner inside the copper canister are illustrated in Figure 11-11. The geometry modelling for the copper canister utilises axial symmetry, and the contact modelling Equation 11-1.

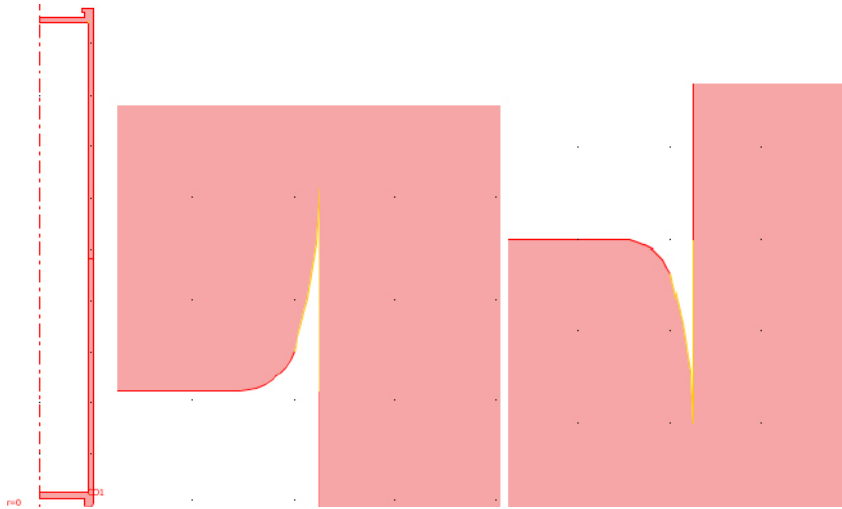


Figure 11-11. Illustrations of simulated canister and slits. The left is the simulated geometry of copper canister. The middle and the right illustration are the enlarged views of the slits at the upper and lower corner between the lid/bottom and cylinder.

When the 15 MPa pressure is applied to the outer surface of the copper canister contact occurs in the slits and some local stresses there become quite high due to the stress concentration. The small contact area cannot sustain such high stresses and will immediately undergo plastic deformation. The radius at bottom of the slits in actual canisters is not known but it cannot be smaller than 0.3 mm, which is the value used in the computations. The reason is that a smaller radius would not be stable during creep, since it would blunt. Elasto-plastic modelling is performed at 75°C, assuming isotropic strain hardening. The results are presented in Figure 11-12 and Figure 11-13. Figure 11-12 shows that the maximum equivalent stress emerges at the initial contact point, the magnitude being 198 and 207 MPa in the upper and lower corners, respectively. The corresponding maximum equivalent plastic strains become 23.4 and 30.2%, Figure 11-13.

The important technical question about the slits is whether they can give rise to failure. The slits appear as sharp notches. Brittle failure can be ruled out since the stresses across the slits are compressive.

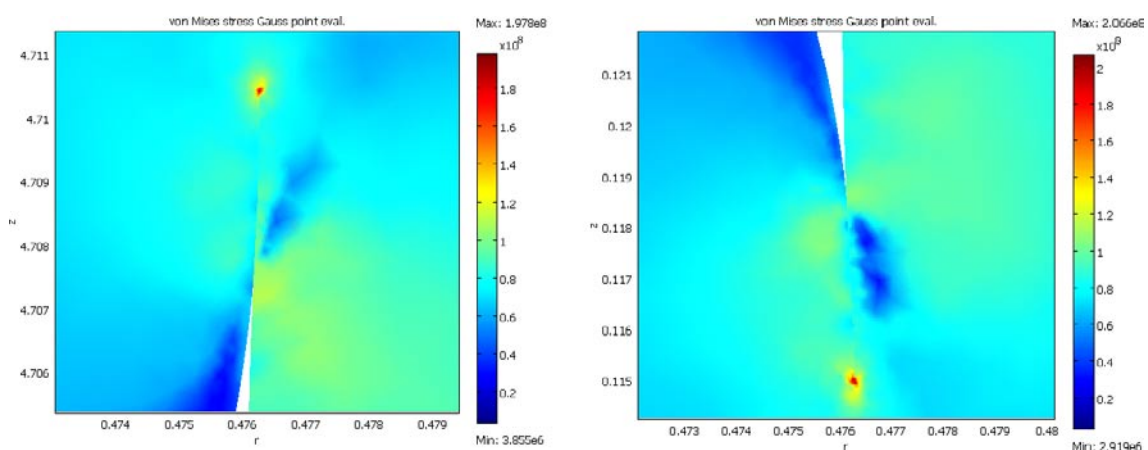


Figure 11-12. Equivalent stress distribution in the slit at the a) upper corner and b) lower corner determined with elasto-plastic modelling.

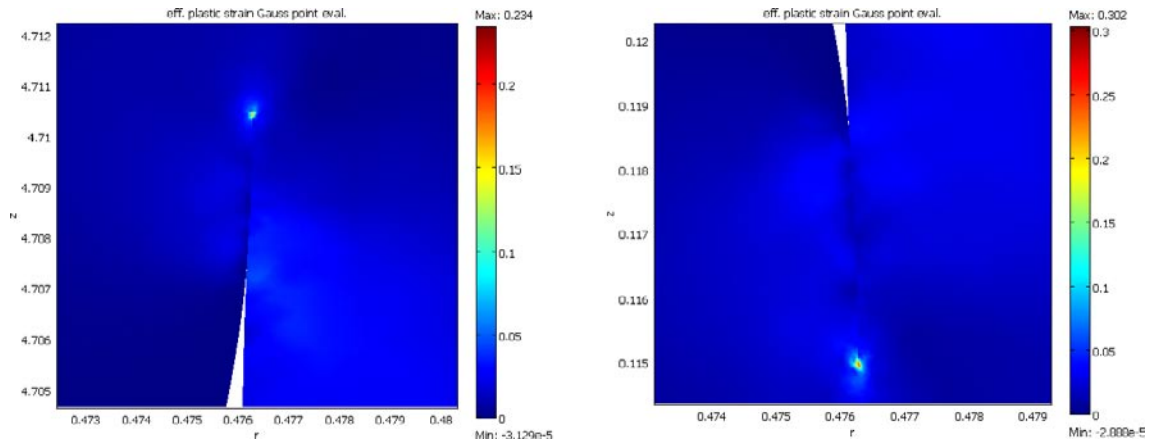


Figure 11-13. Equivalent plastic strain distribution in the slit of a) upper corner and b) lower corner determined with the help of elasto-plastic modelling.

The next possibility is ductile cracking. There are highly localised plastic strains of 20 to 30% in the slit notches. Due to the compressive stresses this type of failure is unlikely. But there is also another way to demonstrate that failure will not take place. It is possible to make a comparison to circumferentially notched creep specimens. These specimens have also highly localised strains. The notch in such a specimen is illustrated in Figure 11-14. The specimen has been tested for 9,701 h at 75°C with a net section stress of 215 MPa. For the slit notches, the von Mises stress presented in Figure 11-12 shows that after the isotropic strain hardening controlled plastic deformation, the stresses lie at a level of 190–210 MPa even with the existence of point contact. This stress level is thus comparable to the net section stress in the creep specimen.

The plastic strain of 20 to 30% that appears in the slits can be compared with the creep specimens in Figure 11-15.

The results of elasto-plastic simulations give an equivalent plastic strain of 16 to 66% at the notch root for notch acuity of 0.5 to 18.8. The strain states at the notches in both the slits and in the creep specimen consist of a tensile and a compressive component of about the same magnitude. These similarities suggest that despite the difference in the geometry and the resulting stress concentration, the strain state at the notch root radius is equivalent to that in the slits after elasto-plastic deformation.

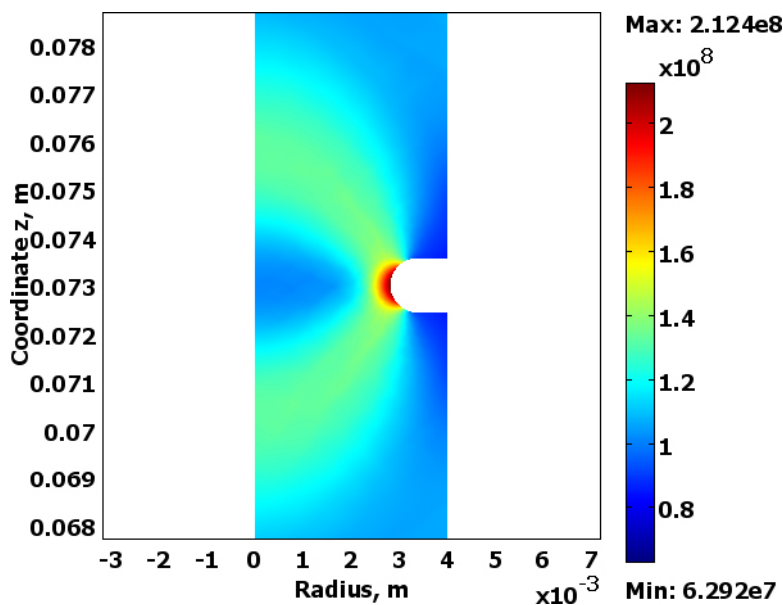


Figure 11-14. von Mises stress distribution after rigid-plastic deformation on notched specimen with acuity 5 and net section stress 215 MPa at 75°C.

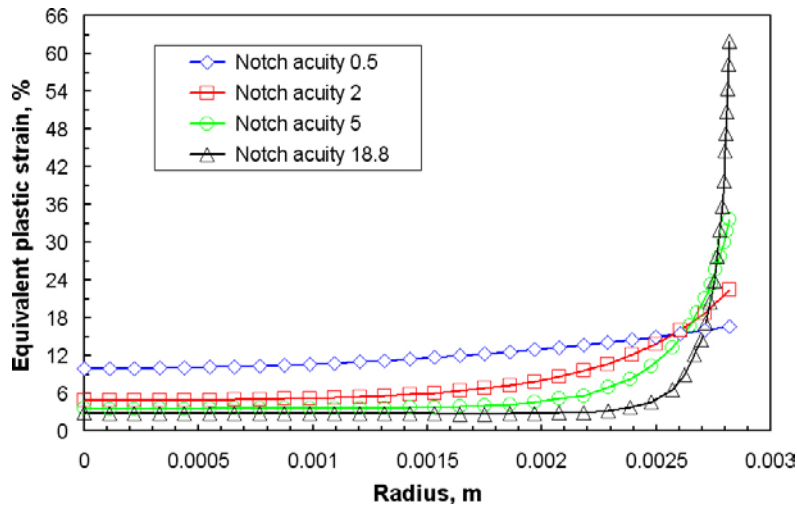


Figure 11-15. Equivalent plastic strain distribution after rigid-plastic deformation along the narrowest cross section to the notch root radius. The net section stress is 215 MPa.

The reason for choosing the specific specimen is that it has run for almost 10,000 h before cracking. The elasto-plastic effective strain at the notch root in this case is 33%. Considering that the notch in the creep specimen is exposed to tensile stresses, this represents a much more critical situation than for the slits with compressive loading. In both the slits and the notched creep specimen there will be creep deformation as well. Computations show that these creep strains are less than 3% and have a limited influence on the plastic deformation in the notches. Since the creep specimen did not fail even after long term exposure it demonstrates that failures in the slits will not take place.

An analysis has been performed for the behaviour of a slit at a higher external pressure of 45 MPa and 27°C, simulating the situation during a glaciation /66/. The investigated slit is shown in Figure 11-16. The climb-glide in Equation 9-24 was used to compute the creep deformation. All creep deformation above 3% is concentrated to one element. The creep deformation in this element is illustrated as a function of time in Figure 11-17. After an initial plastic deformation of 7%, a slow logarithmic increase in the creep strain is observed. Since the creep deformation in this case is concentrated to one element, it is difficult to draw any more general conclusions from the result, in particular since the result is sensitive to how the modelling around the notch is made.

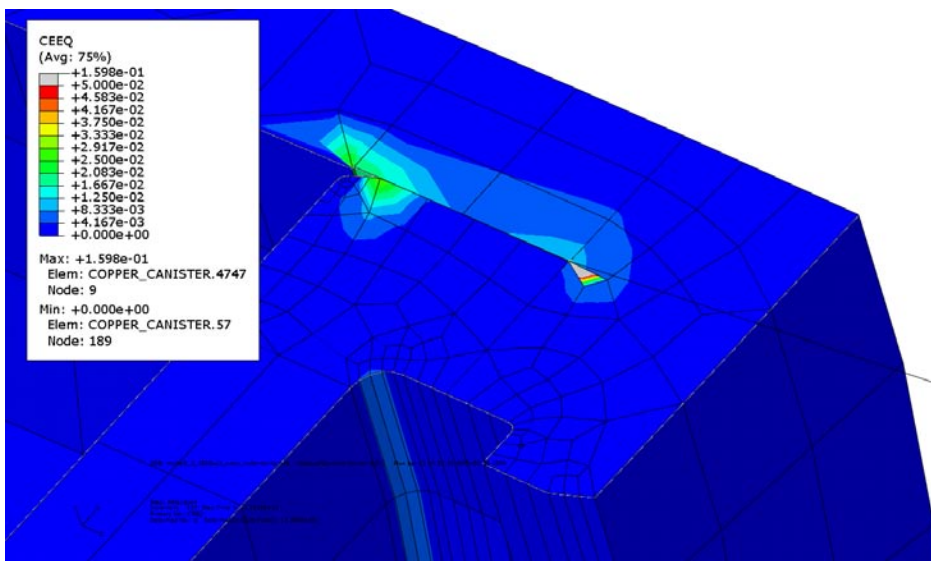


Figure 11-16. Creep deformation in the slit in the lid exposed to 45 MPa external pressure, simulation the conditions during glaciation /66/.

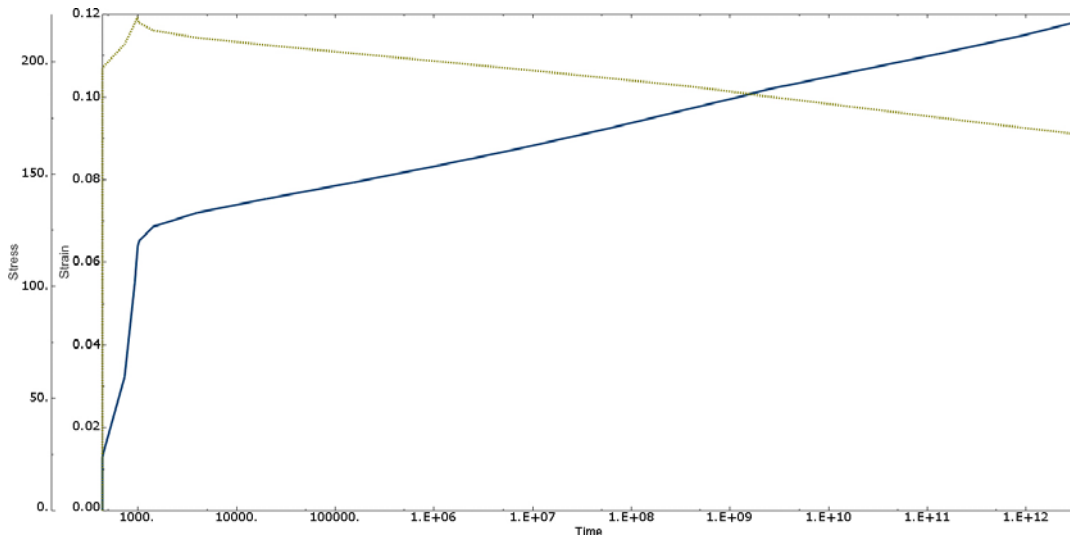


Figure 11-17. Creep deformation (blue curve) and stress (yellow curve) as a function of time for the marked element in Figure 11-16 with the highest strain /66/.

11.4 Effects of uneven swelling pressure on the canister

Due to uneven wetting, rock contours and bentonite density distribution, uneven swelling pressure on the canister can appear. Börgesson et al. have identified load cases that can be expected to have the largest impact on canister and insert /SKBdoc 1206894/. The worst case from the bending stress point of view is a freely supported beam loaded by limited pressure load areas as shown in Figure 11-18. The vectorial sum of the load is always zero under static condition. The maximum values of the pressures are $\sigma_1 = 11.2$ and $\sigma_2 = 3.4$ MPa.

The load case in Figure 11-18 is analysed in Figure 11-19.

The insert has been simplified in Figure 11-19, since the difference between a solid and a tube insert was modest. The highest stresses can be found in the middle part of the insert. These stresses are however, well below the yield strength of the material. The maximum stress in the copper canister is 76 MPa, which will not give rise to creep. The maximum plastic strain in the copper is 0.05%.

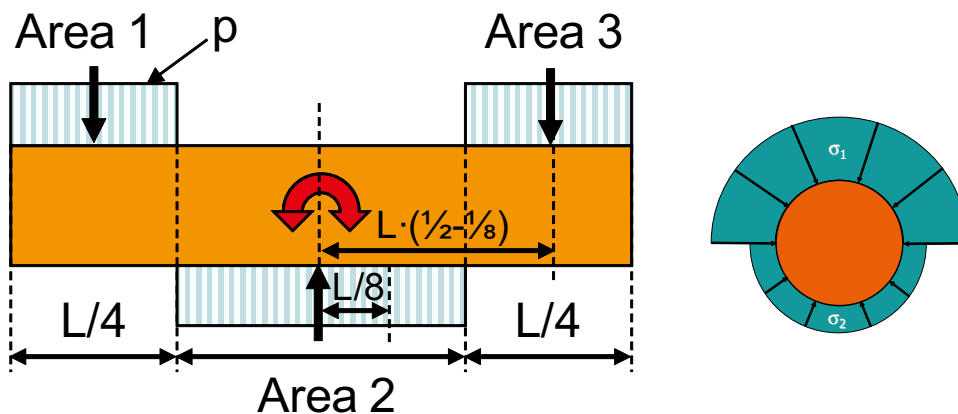


Figure 11-18. Worst load case for uneven swelling pressure on the canister. a) Axial load distribution. b) Circumferential load distribution /SKBdoc 1206894/.

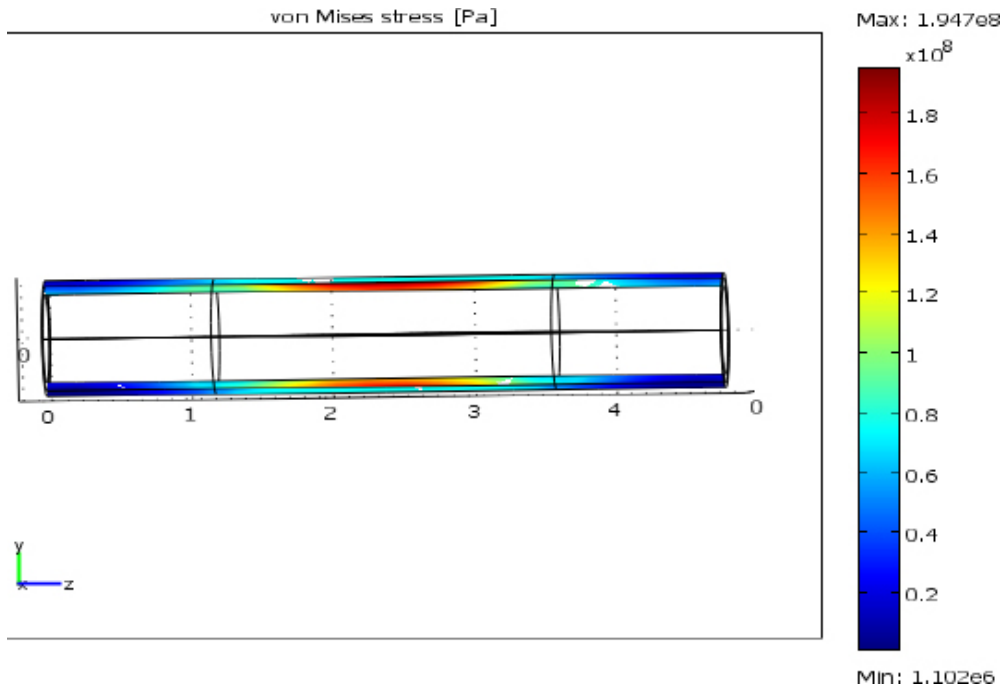


Figure 11-19. The load case in Figure 11-18 is simulated with a copper tube ($t = 50 \text{ mm}$) and cast iron tube ($t = 75 \text{ mm}$). Elasto-plastic analysis. Von Mises stress at 75°C .

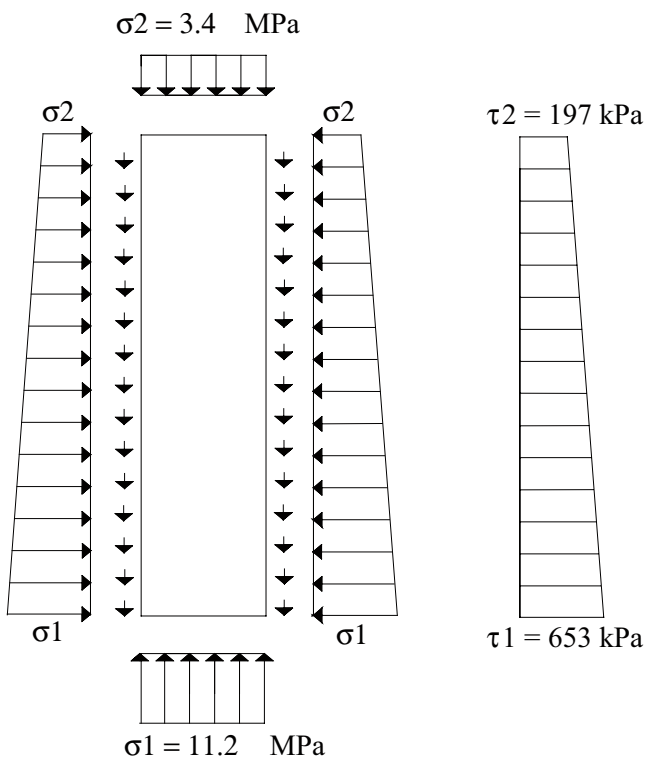


Figure 11-20. Normal stress on the canister surface and resulting shear stresses in the interface between the canister and the bentonite buffer /70/.

Another load case that may occur is that the density of the buffer at the bottom of the deposition hole just below the canister is 2,050 kg/m³ and the density at the top of the deposition hole just above the canister is 1,950 kg/m³. This case can be considered possible since there may be rock fall out in the upper parts and upwards swelling of the buffer against a dry backfill, which will cause a decrease in buffer density in the upper part. Figure 11-20 shows the stresses on the surface of the canister for this load case.

The density at saturation in the top and the bottom of the canister is 1,950 kg/m³ and 2,050 kg/m³, which results in the following swelling pressures $\sigma_1 = 11.2$ and $\sigma_2 = 3.4$ MPa. The swelling pressure and the shear stresses are assumed to vary linearly from the top of the canister to the bottom. Shear stresses must be present to balance the uneven axial forces. The load case in Figure 11-20 is analysed in Figure 11-21. The maximum stress is 167 MPa which is localised to one of the radii. The plastic strain at this position is 2%. Some creep will take place at this position, but due to relaxation of the local stress, the creep strain will be limited. In summary these load cases will not give rise to damage of the waste package.

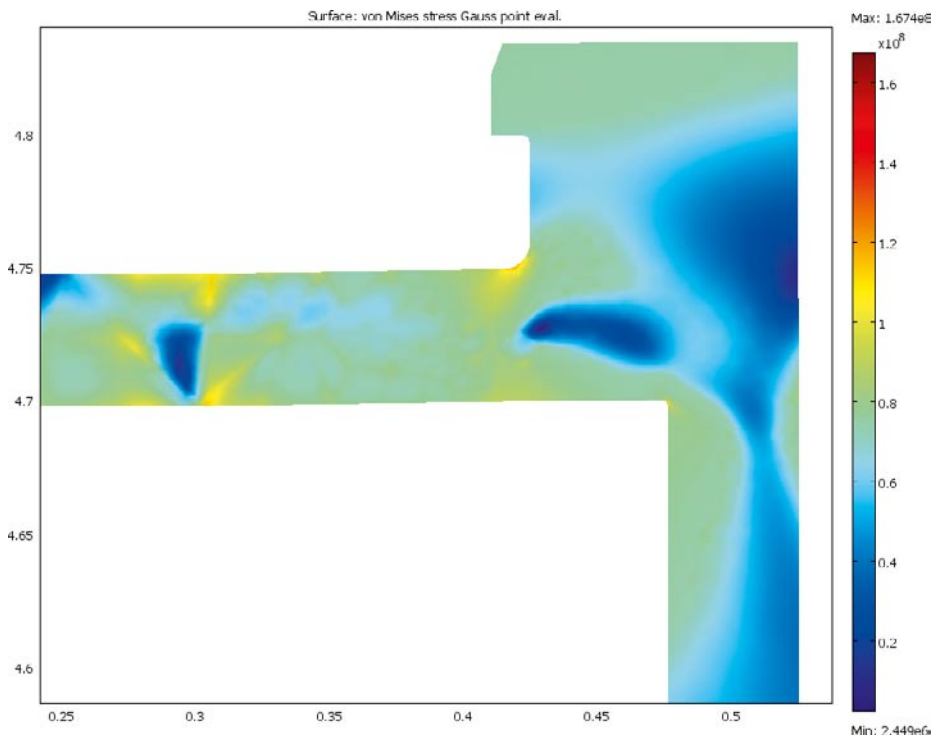


Figure 11-21. Simulation of the load case in Figure 11-20 in the top part of the canister. von Mises stress at 75°C.

12 Conclusions

- Creep testing of Cu-OF and Cu-OFP demonstrates that P-doped copper with a P content in the interval 30 to 120 ppm has higher creep strength and much better creep ductility than copper without phosphorus.
- Parent metal and friction stir welds of Cu-OFP have adequate creep ductility for application in copper canisters. All tests below 300°C have given a creep rupture elongation of at least 30%.
- Cold work reduces the creep ductility and significant cold work should be avoided in the manufacturing and handling of copper canisters.
- Slow strain rate tests can be related to the creep results. This has been utilised in the development of a fundamental model for the flow curves.
- A model for the creep ductility based on nucleation and growth of creep cavities can explain the large effect of phosphorus.
- Unified climb and glide models for the creep rate can represent creep data over a wide range of temperatures.
- New procedures for transferring uniaxial creep models to multiaxial stress states have been developed.
- Multiaxial creep test results for notched bars have successfully been reproduced with finite element modelling.
- The creep deformation in copper canisters has been simulated with FEM-modelling.

13 Acknowledgements

The authors would like to express their gratitude to the Svensk Kärnbränslehantering AB (the Swedish Nuclear Fuel and Waste Management Co) for the funding for this work.

14 Tables

Table 14-1. Chemical compositions of copper studies 1985–2009. Included are also the compositions of the materials referenced in the initial literature survey /4/.

Material	Ag	Al	As	Bi	Cd	Co	Cr	Fe	H	Hg	Mn	Ni	O	P	Pb	S	Sb	Se	Si	Sn	Te	Zn	Zr	Reference	
Ref 4-1*								<3				<5			<1							<10		/4/	
Ref 4-2*	1		<1					<1				1			<1	1	1								/4/
Ref 4-3*																									/4/
Ref 4-4*	<1		<1					4				<1	2		<1	<1		<1							/4/
Ref 4-5*	<1		<1															<1		<1					/4/
Ref 4-6*	2							<1				2	31		<1	1		<1		<1					/4/
Ref 4-7*													25	5											/4/
Ref 4-8*	<2							1				1		8											/4/
Ref 4-9*																									/4/
Ref 4-10*			<10					<10				<10		20						<1		<10			/4/
Ref 4-11*			<10									<10		20						<1		<10			/4/
Ref 4-12*								<2				<2			<1					<1					/4/
Batch 000	20	1	2	0.4	<1	<10	<3	6	0.16	<1	2	3	1.2	2	0.5	10	<3	<1	<1	<3	<3	9	<3		/9, 16/
Batch 100	16	1.5	3	0.3	<1	<10	<3	5	0.69	<1	2	3	1.6	2	0.5	10	3	<1	<1	<3	<3	<1	<3		/9, 16/
Batch 200	10	<1	<1	<1	<1	<10	<3	2	<0.10	<1	<1	<3	1.1	<1	1	6	<3	<1	<1	<3	<3	<1	<3		/9, 12, 16/
Batch 300	1,500	1	<1	<1	<1	<10	<3	2	0.1	<1	<1	3	0.9	<1	<1	6	<3	<1	<1	<3	<3	<1	<3		/9, 12, 13/
Batch 400 (IM)	9.6	9.5	1.4		<0.1	<0.1				<0.1		3.3		59	0.7		1.8				0.6	0.1	<0.1		/9, 10, 15/
Batch 500 (IM)	15	9	1.1		<0.1	<0.1				<0.1		0.8	0.9	54	0.8		1.9				0.2	<0.1	<0.1		/10, 12, 13, 14, 15/
Batch 600 weld	47	1	4	4	3		2	4			2	3	1.3	3	3	3	3	1	4	3	<10	<1			/13, 15/
Batch 700 plate left	12	<1	3	3	<1		<1	3			2	1	1.4	68	3	3	1	1	4	3	<10	<1			/13, 14, 15/
Batch 700 plate right	12	<1	3	2	2		1	4			2	<1	1.4	66	4	3	2	1	4	1	<10	<1			/13, 14, 15/
Batch 700 weld bottom	12	<1	<1	3	1		2	4			2	3	1.3	66	4	3	<1	<1	4	2	<10	<1			/13, 14, 15/
Batch 700 weld top	12	<1	4	3	2		<1	5			2	2	1.1	64	3	3	1	1	3	2	<10	<1			/13, 14, 15/
Batch 720 cylinder	13	<1	5	2	2		2					<1	1.7	58	1	2	<1	<2	2	<1	<10	<1			/13, 14, 15/
Batch 720 lid	12	<1	7	1	2		<1					<1	1.7	46	4	3	1	<2	2	1	<10	1			/13, 14, 15/

Material	Ag	Al	As	Bi	Cd	Co	Cr	Fe	H	Hg	Mn	Ni	O	P	Pb	S	Sb	Se	Si	Sn	Te	Zn	Zr	Reference	
Batch 800 cathode	12	<1	5	<1	2		<1	3			2	3	7	4	3	<1	2	1	3	<1	<10	<1		/13, 14, 15/	
Batch 820 cathode	1	<1	8	1	2		1					<1	51	<1	<1	<1	<1	<2	2	<1	<10	<1		/13, 14, 15/	
Cu65_450_S12									< 0.5				1.1	67		12									/18/
CuP0_300									< 0.5				1.1	<1		6									/18/
CuP105_450									< 0.5				1.1	106		6									/18/
CuP30_450									< 0.5				1.2	29		6									/18/
CuP60_100									< 0.5					58		6									/18/
CuP60_2000									< 0.5				1.3	62		6									/18/
CuP60_350									< 0.5				1.1	58		6									/18/
CuP60_800									< 0.5				1.6	57		6									/18/
SKB Friction stir material																									/21,22/
SKB extruded Cu tube														40–70											/24/
SKB extruded Cu lid	13		<1	<1	<1	<1	<1	2			<0.5	2		45–60	<1	5	1	<1		<0.5	<1	<1			/24/

* Chemical data from ref /4/ are from the literature survey. 1: Burghoff, Blank 1947, 2: Schwope, Smith, Jackson 1949, 3: Jenkins, Digges 1950, 4: Feltman, Meakin 1959, 5: Barrett, Sherby 1964, 6: Schwope, Smith, Jackson 1949, 7: Bowers, Lushey 1978, 8: Burghoff, Blank 1947 and 1945, 9: Kouta, Webster 1981, 10 and 11: Drefahl, Kleinau 1982, 12: Burghoff, Blank 1947.

Table 14-2. Copper type and material format for the tested materials.

Material	Copper type	As received format	Lid, weld or tube number if applicable	Grain size (µm)	Reference
Batch 000	Cu-OF	100×100 mm forged bars		60	/9, 16/
Batch 100	Cu-OF	Edge of 100×100 forged bars EB-welded together		370	/9, 16/
Batch 200	Cu-OF	10 mm diameter hot extruded (800°C) bars		45	/9, 12, 16/
Batch 300	Cu-OFS	10 mm diameter extruded bars		35	/9, 12, 16/
Batch 400 (IM)	Cu-OFP	10 mm diameter extruded bars		45	/9, 10, 15/
Batch 500 (IM)	Cu-OFP	30mm hot rolled plate		115	/10–15/
Batch 600 weld	Cu-OF	Weld	Block reference 5E1307	variable	/13, 15/
Batch 700 plate left	Cu-OFP			238	/13–15/
Batch 700 plate right	Cu-OFP			345	/13–15/
Batch 700 weld bottom	Cu-OFP	Hot-worked blocks EB-welded together to one block 115×95×165 mm		variable	/13–15/
Batch 700 weld top	Cu-OFP			variable	/13–15/
Batch 720 cylinder	Cu-OFP	Welded joint	Lid W92, 5E1585	variable	/13–15/
Batch 720 lid	Cu-OFP	Welded joint	Lid W92, 5E1585	variable	/13–15/
Batch 800 cathode	Cu-cathode	18×74×180 mm cathode		anisotropic	/13–15/
Batch 820 cathode	Cu-cathode	Cathode tube length 70 mm, 30 mm diam, 5 mm thickness		aniso-tropic	/13–15/
Cu65_450_S12	Cu-OFPS			450	/18/
CuP0_300	Cu-OF			300	/18/
CuP105_450	Cu-OFP			450	/18/
CuP30_450	Cu-OFP			450	/18/
CuP60_100	Cu-OFP	20 mm diameter hot extruded bar		100	/18/
CuP60_2000	Cu-OFP			2,000	/18/
CuP60_350	Cu-OFP			350	/18/
CuP60_800	Cu-OFP			800	/18/
SKB Friction stir material	Cu-OFP	Hot rolled plate	?		/21, 22/
SKB extruded Cu tube	Cu-OFP	pierce and drawn tube	Tube T18, ingot 248-3-1		/24/
SKB extruded Cu lid	Cu-OFP	forged lid	Lid TX 104, cast NA L760		/24/

Table 14-3. Creep test results from pilot creep study /5/.

Test ID	Copper batch	Struct.	Temp.	Stress	Rupt. time	Min creep rate	Elong	Red. in area	Dia.	Gauge length	PLM	n
			degC	MPa	h	(s ⁻¹)	%	%	(mm)	(mm)	(10 ³)	dε/dt=B*σ ⁿ
2				140	6,300	2.4E-09	20	31			8.28	
3				145	7,840	8.9E-10	18	33			8.32	
4	Cu-OF	PM	75	150	1,697	4.4E-09	13	33	5	50	8.08	27
5				160	464	3.1E-08	28	42			7.89	
6				170	110	2.2E-07	36	45			7.67	
26				60	3,866						9.03	
27				80	510						8.70	
29	Cu-OF	CW	110	100	223				5	50	8.56	
28				100	445						8.67	
30				120	36	6.1E-08					8.26	
7				100	7,000	1.3E-09	11	25			9.13	
8				110	5,890	1.9E-09	9.8	23			9.10	
9	Cu-OF	PM	110	120	1,430	5.6E-09	15	27	5	50	8.87	13
10				130	661	1.5E-08	17	36			8.74	
11				140	168	6.1E-08	21	36			8.51	
12				150	60	1.9E-07	15	36			8.34	
23				120	14,523	5.6E-10	4.4	29			9.25	
24	Cu-OF	Sim HAZ	110	135	2,105	3.9E-09	6.8	26	5	50	8.93	18
25				150	408	3.3E-08	14	31			8.66	
19				80	16,605	5.6E-11	2.7	18			9.28	
20	Cu-OF	WM	110	100	2,065	3.1E-09	5.8	25	5	50	8.93	18
21				110	456	8.6E-09	9.5	39			8.68	
22				120	30	1.1E-07	9.5	42			8.23	
13				75	5,356	7.8E-10	4.9	23			9.92	
14				85	1,775	1.4E-09	4.4	15			9.72	
15	Cu-OF	PM	145	90	735	6.4E-09	6	12	5	50	9.56	10
16				100	650	1.2E-08	11	26			9.54	
17				110	265	3.1E-08	13	21			9.37	
18				120	110	9.7E-08	16	27			9.21	

Table 14-4. Creep test results from the 1992 study of series 000, 100, 200 and 300 /9/.

Test ID	Copper batch	Struct.	Temp. degC	Stress MPa	Rupt. time h	Min creep rate (s ⁻¹)	Elong %	Dia. (mm)	Gauge length (mm)	PLM (10 ³)	n dε/dt=B*σ ⁿ
31	000 Cu-OF	PM	180	60	2,247	4.0E-10	0.9	5	50	10.58	5
32				80	373	1.2E-09	0.3			10.22	
33				100	102	4.6E-09	0.3			9.97	
41	000 Cu-OF	PM	215	40	4,623	1.5E-10	0.8	5	50	11.55	5
42				60	754	8.1E-10	0.3			11.16	
43				80	86	4.8E-09	0.3			10.70	
52	000 Cu-OF	PM	250	40	1,660	5.7E-10	0.7	5	50	12.14	4
53				60	175	3.0E-09	0.4			11.63	
102	100 Cu-OF	PM	215	55	250		0.2	5	50	10.93	4
101				45	684	5.6E-10	0.6			11.14	
103				70	84	5.0E-09	0.3			10.70	
104				85	33	7.2E-09	0.3			10.50	
203	200 Cu-OF	PM	215	70	5,058	4.0E-09	12	5	50	11.57	7
204				85	1,030	1.7E-08	11			11.23	
205				100	330	5.6E-08	10			10.99	

Table 14-5. Creep test results from the 1995 study of series 400 and 500 /10/.

Test ID	Copper batch	Struct.	Temp.	Stress	Rupt. time	Min creep rate	Plastic strain on loading	Elong	Red. in area	Dia.	Gauge length	t _{1%}	t _{2%}	t _{5%}	t _{10%}	PLM	n	
			°C	MPa	h	(s ⁻¹)	(%)	%	%	(mm)	(mm)	(h)	(h)	h	h	(10 ³)	dε/dt=B*σ ⁿ	
401	400 Cu-OFP	PM	215	120	7,848	7.7E-09	0.2	36	64			7	85	533	1,907	11.66	17	
402				140	1,447	1.4E-08	0.2	39	78	5	50	5	18	67	245	11.30		
406				160	52	8.3E-07		32	83						–	1		10.60
407				150	192	3.3E-07		41	85						0.07	2		10.87
410	400 Cu-OFP	PM	300	100	220	3.0E-07		39	76					15	55	12.80	8	
415				90	622	1.1E-07		47	42	5	50			23	103	13.06		
416				80	1,374	4.7E-08		49	54					81	315	13.26		
417				70	3,635	1.7E-08		31	48					646	1,494	13.50		
411	400 Cu-OFP	PM	450	30	195	2.5E-07		44	45	5	50			34	92	16.12		
412	400 Cu-OFP	PM	250	100	4,796	9.9E-09		42	39					92	547	12.39	15	
413				120	656	1.5E-07		58	57	5	50			3	42	11.93		
414				110	2,768	2.4E-08		51	62					57	348	12.26		
424	400 Cu-OFP	PM	350	70	194	3.6E-07		80	90					7	35	13.89	7	
426				40	4,704	8.1E-09		24	39	5	50	299		1,597	2,894	14.75		
427	400 Cu-OFP	PM	400	40	469	9.7E-08		23	4.2					110	222	15.26	6	
428				30	1,558	1.9E-08		17	19	5	50			674	1,189	15.61		
514	500 Cu-OFP	PM	200	120	3,272	1.6E-08		44	40	5	50			0.05	17	11.12		
501	500 Cu-OFP	PM	215	120	2,133	2.3E-08		42	56	5				–	11	11.38	9	
509				110	2,646	2.0E-08		39	49	5				0.02	55	11.43		
510				100	5,125	5.4E-09		29	64	5	50			7	401	11.57		
523				120	1,350	4.4E-08		54.5	59.9	10								11.29
502	500 Cu-OFP	PM	250	120	94	6.9E-07		45	76	5				–	0.1	11.49	14	
503				110	361	1.7E-07		46	65	5					–	1		11.80
504				100	883	6.1E-08		39	50	5					–	22		12.00
505				90	2,895	1.5E-08		37	30	5	50				15	238		12.27
524				120	53.2	1.0E-06		59.9	72.7	10								11.36
525				100	1,084	5.3E-08		47.5	51.8	10								12.05

Test ID	Copper batch	Struct.	Temp. °C	Stress MPa	Rupt. time h	Min creep rate (s ⁻¹)	Plastic strain on loading (%)	Elong %	Red. in area %	Dia. (mm)	Gauge length (mm)	t _{1%} (h)	t _{2%} (h)	t _{5%} h	t _{10%} h	PLM (10 ³)	n dε/dt=B*σ ⁿ
506	500 Cu-OFP	PM	275	100	295	2.1E-07		41	54					–	6	12.31	10
507				90	714	7.2E-08		34	50	5	50			0.6	37	12.52	
508				80	2,142	2.1E-08		33	32					12	232	12.79	
512	500 Cu-OFP	PM	300	70	1,218	3.9E-08		32	35					22.6	191	13.23	6
513			300	60	2,426	1.3E-08		20	16	5	50			370	1,398	13.40	
518			300	80	683	7.8E-08		37	38					6	63	13.08	
519	500 Cu-OFP	PM	325	50	1,357	6.9E-09		14	13	5	50			983	1,345	13.83	
516	500 Cu-OFP	PM	350	50	577	6.9E-08		22	22					105	305	14.18	5
517			350	40	1,105	2.4E-08		14	19	5	50			560	1,050	14.36	
527	500 Cu-OFP	PM	600	2	25,873	1.4E-10	0.8	9.8	0.2			13,296	23,670	25,100		21.31	
528			600	3	16,769	1.4E-10	0.2	12.6			10	50	9,356	16,656	16,756	16,764	21.15
555	500 Cu-OFP	PM*	215	120	894	6.7E-08		63	60	5	50					11.20	
556	500 Cu-OFP	PM*	250	120	48.4	1.1E-06		55	74	5	50						

Table 14-6. Creep test results from the 1996 study of series 600, 700 and 800 /13, 14/.

Test ID	Copper batch	Struct.	Temp.	Stress	Rupt. time	Min creep rate	Plastic strain on loading	Elong	Red. in area	Dia.	Gauge length	t _{1%}	t _{2%}	t _{5%}	t _{10%}	PLM	
			°C	MPa	h	(s ⁻¹)	(%)	%	%	(mm)	(mm)	(h)	(h)	h	h	(10 ³)	
614 L	600 Cu-OF	WM	215	70	17			9	9	5	50					10.36	
604 T	600 Cu-OF	WM	215	70	49			4.1	13	5	50					10.58	
603 T				30	4,702	1.9E-10	2.1	1.3									11.55
605 T	600 Cu-OF	WM	250	120	0.08			7.9	37	5	50					9.89	
703 CW	700 Cu-OFP	CW bottom	215	120	7	3.1E-06	7.9	29	75	5	35					10.17	
706 CW				100	408	4.3E-08	2.0	22	65						15	192	11.03
709 CW	700 Cu-OFP	CW bottom	250	90	163	1.2E-07	0.8	28	48	5	35			28		11.62	
705 CW	700 Cu-OFP	CW middle	215	100	592	2.7E-08	3.1	20	67	5	35			2	209	11.11	
708 CW	700 Cu-OFP	CW middle	250	90	174	7.5E-08	1.8	17	53	5	35			15	125	11.63	
704 CW	700 Cu-OFP	CW top	215	100	604	1.6E-08	1.2	16	38	5	35			130	590	11.12	
701 CW				70	5,718	6.1E-10	0.2	8.9	37					2,326	4,920		
707 CW	700 Cu-OFP	CW top	250	90	191	7.4E-08	0.5	17	40	5	35			15	197	11.65	
714 L	700 Cu-OFP		215	100	1,115	2.1E-08		27	43	5	35			18	378	11.25	
720A long	720 Cu-OFP	WM top	215	100	1,192	1.8E-08	1.5	24	52	5	35			217		11.26	
720B long				110	105	1.3E-07	5.7	26	47					7	62	10.75	
720C long		WM bottom		90	2,112		1.1	28	41					158		11.38	
720E long				100	531	4.4E-08	4.2	24	45					71	346	11.09	
721 CW	720 Cu-OFP	CW	215	110	41			47	83							10.55	
723 CW				100	699	1.8E-08	2.3	36	57	5	15			29	387	11.15	
724 CW				90	1,003			27	52								11.22
726 CW				70	6,072			22	22								11.61
722 CW	720 Cu-OFP	CW	250	90	163			28	48							11.62	
725 CW				70	543			26	38	5	15					11.89	
727 CW				50	1,748			12	5.5							12.16	
731 trans	720 Cu-OFP	WM trans	215	100	122		0.0	35	70					5		10.78	
732 trans				70	3,140		0.2	17	45	5	35	7	98	1,100		11.47	
733 trans				90	678	3.8E-08	3.2	25	47						61	400	11.14
801 T	800 cathode Cu	Anisotrop	215	100	0.43			2.4	5.5							9.58	
802 T				30	1,212	3.9E-09	0.3	4.7	3.6	5	35			474		11.26	
811 L	800 cathode Cu	Anisotrop	215	100	0.85			5.5	3.2		35					9.73	
812 L				30	1,468			6.3	0.8				35			11.31	
821 L				50	0.23			1.5	1	5	30					9.45	
822 L				30	581			4.4	0.5				30			11.11	
824 L				40	18			3.5	0.1				30			10.37	

Table 14-7. Creep test results from the 1999 study of creep tests with varying sulphur and phosphorus content and different grain sizes /18, 19/.

Test ID	Copper batch	Struct.	Temp.	Stress	Rupt. time	Min creep rate	Plastic strain on loading	Elong	Red. in area	Dia.	Gauge length	t _{1%}	t _{2%}	t _{5%}	t _{10%}	PLM	n		
			°C	MPa	h	(s ⁻¹)	(%)	%	%	(mm)	(mm)	(h)	(h)	h	h	(10 ³)	dε/dt=B*σ ⁿ		
CuP0_300_1Lb	CuP0_300	PM	175	110	675	7.2E-09	4.7	14	30			7	200	8.8		10.23	20		
CuP0_300_1Jb				120	315	1.5E-08	5.3	12	36				51	223	315			10.08	
CuP0_300_1Kb				130	116	5.0E-08	6.3	14	18				20	80				9.88	
CuP0_300_1N				130	29	1.9E-07	8.8	16.6	36.0	10	75			6	29			9.62	
CuP0_300_1M				135	24	5.6E-07	9.4	19	30						18			9.58	
CuP0_300_1K				140	27	2.1E-07	9.1	17.3	35.9						27			9.60	
CuP0_300_1J				150	4.6	4.1E-06	12.6	23.0	43.4						3.7			9.26	
CuP105_450_4N				CuP105_450	PM	175	145	3,169	1.0E-08	11.2	39	69				58		408	1,497
CuP105_450_4J	150	677	4.6E-08				12.3	39.2	80.7	10	75				34	249	10.23		
CuP105_450_4L	155	215	1.3E-07				13.5	39.3	75.3						10	86	10.00		
CuP30_450_2L	CuP105_450	PM	175	145	11,086	2.3E-09	8.8	35	56				6	300	3,493	10.77	37		
CuP30_450_2N				147.5	676	3.4E-08	11.3	46	70	10	75				13	122		10.23	
CuP30_450_2J				150	147	1.0E-07	7	44.0	79.9						3	45		9.93	
CuP30_450_2K				160	92	1.9E-07	13.3	45.0	77.8						3	18		9.84	
CuP60_100_6J	CuP60_100	PM	175	150	1,486	2.9E-08	11	48.4	75.4					9	102	10.38	27		
CuP60_100_6L				155	949	4.2E-08	11.2	49.5	69.1	10	75				7	99		10.29	
CuP60_100_6K				160	242	1.7E-07	7.9	48.6	84.7						3.3	32		10.03	
CuP60_2000_8J	CuP60_2000	PM	175	120	5,012	1.2E-09	6.5	15.8	57.3			26	768	4,996		10.62	14		
CuP60_2000_8M				145	67	1.1E-07	9.8	19.7	76.6							53		9.78	
CuP60_2000_8N				150	2,138	4.8E-09	8.3	16	44	10	75			391	1,978			10.45	
CuP60_2000_8L				155	84	1.2E-07	11.4	23.4	61.9							52		84	9.82
CuP60_2000_8K				160	39	6.9E-08	13.3	23.1	49.3							39			9.67
CuP60_350_3N	CuP60_350	PM	175	147.5	1,173	3.1E-08	11.4	39.9	71.4					39	459	10.34	30		
CuP60_350_3J				150	2,351	1.3E-08	11.1	43.2	71.4							94		863	10.47
CuP60_350_3L				155	103	3.9E-07	14.3	44.3	75.6	10	75					8		34	9.86
CuP60_350_3M				155	231	1.4E-07	17.5	42.5	80.6							82		154	10.02
CuP60_350_3K				160	240	1.3E-07	5.5	41.9	94.7							53		164	10.03
CuP60_800_7J	CuP60_800	PM	175	150	8,997	9.4E-10	9.4	30	46				16	614	6,545	10.73	74		
CuP60_800_7M				152	510	4.2E-08	12.4	37.6	65.8					14	83	346		10.17	
CuP60_800_7L				155	283	8.1E-08	12.1	39.2	73.9	10	75					25		131	10.06
CuP60_800_7K				160	60	2.5E-07	14.4	39.5	95.6							7		44	9.76
CuP65_450_S12_5N	CuP65_450_S12	PM	175	145	6,414	4.2E-09	9.8	37	61				11	859	2,588	10.67	46		
CuP65_450_S12_5J				150	1,032	1.7E-08	11.7	36.1	74.5							45		527	10.31
CuP65_450_S12_5L				155	116	2.2E-07	14	43.8	84.0	10	75					7		38	9.88
CuP65_450_S12_5K				160	171	2.6E-07	11.4	41.1	83.1							11		74	9.96

Table 14-8. Creep test results from the 2004 study of creep tests on material from FSW and EB welds /21, 22/.

Test ID	Struct.	Temp. °C	Stress MPa	Rupt. time h	Min creep rate (s ⁻¹)	Plastic strain on loading (%)	Elong % %	Red. in area %	Dia . (mm)	Gauge length (mm)	t _{1%} (h)	t _{2%} (h)	t _{5%} h	t _{10%} h	PLM (10 ³)	n dε/dt=B*σ ⁿ
2-120-A	EB CW	125	130	9,514	4.4E-10	7.1	25	67	10	50				145	8,505	9.54
2-100-B			135	2,251	4.2E-09	8.5	27.8	67						97	2,150	9.29
2-005-D			137	527	1.8E-08	10.3	30.1	87						43	511	9.04
2-170-C			142	39	2.5E-07	9.9	30.3	88						6	8.59	
3-230-D	EB CW	175	117	1,474	7.5E-09	7.5	24.6	65	10	50		3	224	1,402	10.38	
3-310-C			120	1,158	4.9E-09	7.8	28.1	71						49	1,028	10.31
3-290-B			130	44	2.2E-07	9.1	28.8	84						12	9.70	
1-C-3	EB CW	75	150	1,688	5.3E-09	11.7	30.9	78	10	50				134	1,622	8.08
1-A-1			155	180	4.6E-08	10.1	26.2	81						56	7.74	66
5-1-B	FSW CW bottom	175	130	12,787	2.5E-09	4.7	31.7	41	10	80				195	1,941	10.80
5-3-C			135	4,606	6.9E-09	6.7	37.8	75						127	800	10.60
5-2-A			140	635	3.6E-08	8.3	37.8	79						10	92	10.22
5-4-D			147	45	6.4E-07	10.1	35	86						2	5	22
6-5-A	FSW CW top	125	150	8,430	1.4E-09	9.5	37.6	85	10	80				52	1,112	9.52
6-3-C			155	1,150	4.7E-09	12.4	41.5	86						5	75	9.18
6-1-D			160	150	8.9E-08	13.5	42.3	88						5	27	8.83
4-3-D	FSW CW top	175	130	10,875	3.2E-09	8.5	39.3	73	10	80		20	152	97	1,294	10.77
4-8-C			140	619	3.5E-08	10.1	39.1	81						9	100	10.21
4-2-B			140	2,016	5.8E-09	9.3	40.1	81						10	568	10.44
4-1-A			150	40	4.7E-07	12.0	38.3	88						2	20	9.68
7-2-B	FSW CW top	75	165	7,122	1.1E-09	11.0	35.1	87	10	80		1	26	67	1,168	8.30
7-3-C			170	660	1.2E-08	11.7	36.5	87						26	790	7.94
8-2-A	FSW HAZ	175	135	6,272	7.8E-09	9.0	54.1	81	10	80				25	485	10.66
8-3-B			140	1,133	2.9E-08	10.7	52.1	85						52	236	10.33
8-4-C			145	211	1.3E-07	13.1	48.9	89						5	51	10.00
10-3-B	FSW WM bottom	175	131	6,106	5.0E-09	8.9	52.7	69	10	80		2	1	40	361	10.66
10-2-A			135	1,113	1.8E-08	10.0	36.4	49						22	250	10.32
10-4-C			142	719	3.0E-08	9.0	30.8	53						17	207	10.24
10-5-B			143	174	1.1E-07	11.2	35.1	54						2	24	9.96
9-2-A	FSW WM top	175	135	10,754	8.9E-09	10	52.9	80	10	80				70	953	10.77
9-3-B			140	2,311	2.1E-08	10.1	52.3	75						20	145	10.47
9-4-C			148	90	5.3E-07	13.2	52.6	84						2	22	9.84
11-1-D	PM	125	165	1,657	2.8E-09	7.5	36.6	90	10	80				1,459	1,596	9.24
12-3-B	PM	175	135	14,681	1.3E-09	1.5	45.2	80	10	80		2	31	2,650	10,393	10.83
12-1-D			140	1,622	1.6E-08	2.7	42	83						13	120	10.40
12-4-C			145	162	1.5E-07	5.1	38.9	86						4	31	9.95

Table 14-9. Creep test results from the 2007 creep test study on friction stir welds /24/.

Test ID	Copper batch	Struct.	Temp.	Stress	Rupt. time	Min creep rate	Plastic strain on loading	Elong	Red. in area	Dia.	Gauge length	t _{2%}	t _{5%}	t _{10%}	PLM	n		
			°C	MPa	h	(s ⁻¹)	(%)	%	%	(mm)	(mm)	(h)	h	h	(10 ³)	dc/dt=B*σ ⁿ		
LID75_1	TX104	PM lid	75	175	1,162	1.5E-08	9.3	43.6	90.2	10	80	1,500	1,850	3,980	6	145	78	
LID75_2				170	13925	1.4E-09	10.3	43.4	91.0						2	2,840		6.59
LID75_3				180	175	5.3E-08	11.2	45.6	92.2						3	56		6.07
LID75_5				170	9,585	3.6E-10	8.3	51.1	90.9						8.35			
TUB75_2	T18	PM tube	75	170	7,877	4.4E-09	10.1	52.7	91.6	10	80				971	3,570	6.52	
TUB75_1				175	6,974	6.9E-10	14.3	47.1	90.6						100	2,266	6.51	58
TUB75_4				180	120	1.3E-07	14.4	48.1	92.1						9	7.68		
WINR75_1	L21	CW inner	75	175	32	1.7E-07	10.7	47.4	89.1	10	60				25		5.87	
WINR75_2				170	398	3.1E-08	10.8	47.5	86.2						7	149	6.17	47
WINR75_3				160	6,271	2.3E-09	9.9	46.2	84.7						10	858	8.28	
WMI75_1	L21	WM inner	75	175	1,868	2.8E-08	13.8	63.8	89.6	10	50				1,565	1,605	6.35	
WMI75_2				170	2,207	1.1E-08	10.7	64.9	87.4						73	117	8.12	32
WMY75_2	L21	WM outer	75	170	4,378	5.0E-10	14.2	65.3	82.9	10	50				30	560	6.45	
WMY75_3				180	28	6.1E-07	15.2	65.1	90.1						83	7.46	124	
WYTT75_1	L21	CW outer	75	175	62	5.3E-07	13.5	54.3	92.8	10	60					20	5.95	
WYTT75_2				170	835	3.3E-08	15.7	53.7	88.0						8	159	7.98	95
HAZ75_1	L21	HAZ weld	75	175	25	1.3E-06	10.7	67.2	91.1	10	50					3	5.84	
HAZ75_2				170	360	4.7E-08	16.4	66.2	90.8						5	27	179	7.85

15 References

SKB's (Svensk Kärnbränslehantering AB) publications can be found at www.skb.se/publications.
References to SKB's unpublished documents are listed separately at the end of the reference list.
Unpublished documents will be submitted upon request to document@skb.se.

- /1/ **Gifkins R C, 1994.** Grain-boundary participation in high-temperature deformation: an historical review, *Materials Characterization* 32, pp 59–77.
- /2/ **Frost H F, Ashby M F, 1983.** *Deformation Mechanism Maps*, p.21, Pergamon Press, Oxford.
- /3/ **Ivarsson B, Sandstrom R, 1980.** Creep deformation and rupture of butt welded tubes of cold worked AISI 316 steel, *Metals Technology*. Vol. 7, no. 11, pp. 440–448. Nov. 1980.
- /4/ **Yngrén L, 1985.** “Konstitutiva ekvationer för krypning hos renkoppar”, Swedish Institute for Metals Research, IM-1970.
- /5/ **Ivarsson B, Österberg J O, 1988.** Creep properties of welded joints in OFHC [oxygen free high conductivity] copper for nuclear waste containment. SKB TR-88-20 (DE89614655), Svensk Kärnbränslehantering AB.
- /6/ **Ivarsson B, Österberg J O, Sandström R, Werme L, 1989.** Creep Properties of Welded Joints in Copper Canisters For Nuclear Waste Containment, Paper From Scientific Basis for Nuclear Waste Management XII, Materials Research Society Symposium Proceedings, Vol 127, pp 397–402.
- /7/ **Henderson P J, Österberg J O, Ivarsson B, 1992.** ”Low Temperature Creep of Copper Intended for Nuclear Waste Containers”, Gov. Res. Announc. Index (USA) , pp. 36.
- /8/ **Lindblom J, Henderson P J, Seitisleam F, 1992.** Creep, stress relaxation and tensile testing of oxygen free phosphorous copper (Cu-OFP) intended for nuclear waste containment, Swedish Institute for Metals Research, IM-2936.
- /9/ **Henderson P J, 1994.** Creep of Copper, Paper from the KASAM/SKI International Seminar on Design and Manufacturing of Copper Canisters for Nuclear Waste, Sollentuna, Sweden, pp 8, April 27–28.
- /10/ **Lindblom J, Henderson P J, Seitisleam F, 1995.** Creep testing of oxygen-free phosphorous copper and extrapolation of the results, Swedish Institute for Metals Research, IM-3197.
- /11/ **Henderson P J, Seitisleam F, 1995.** Creep crack growth in oxygen-free phosphorous copper, Cu-OFP, Progress report for SKB, Swedish Institute for Metals Research.
- /12/ **Henderson P J, Lindblom J, 1995.** Results of Round-Robin tensile testing and effect of specimen diameter on the tensile and creep properties of high-purity copper, Progress Report 95 -2, Swedish institute for metals research, August.
- /13/ **Seitisleam F, Henderson P J, Lindblom J, 1995.** Creep of copper for nuclear waste containment – Results of creep and tensile tests on Cu-OF, Cu-OFP cathode copper and welded joints, Swedish Institute for Metals Research, IM-3327.
- /14/ **Seitisleam F, Henderson P J, 1996.** Creep of copper for nuclear waste containment – Results of testing performed in 1996, Swedish Institute for Metals Research, IM-3506.
- /15/ **Henderson P J, Werme L, 1996.** Creep testing of copper for radwaste canisters, Proc EUROMAT 96 – Materials and Nuclear Power, Bournemouth, United Kingdom, pp 227–234, October.
- /16/ **Sandstrom R, Henderson P J, 1998.** Low temperature creep ductility of OFHC copper, *Materials Science and Engineering A (Switzerland)*. Vol. 246, no. 1–2, pp. 143–150.
- /17/ **Yao X X, Sandström R, 2000.** Study of creep behaviour in P-doped copper with slow strain rate tensile tests, SKB TR-00-09, Svensk Kärnbränslehantering AB.
- /18/ **Andersson H, Seitisleam F, Sandström R, 1999.** Influence of phosphorous and sulphur as well as grain size on creep in pure copper. SKB TR-99-39, Svensk Kärnbränslehantering AB.

- /19/ **Andersson H C M, Seitisleam F, Sandström R, 2001.** Influence of Phosphorous on creep in pure copper, MRS Spring Meeting, San Francisco, 16–20 April 2001 (also SKB TR-01-25), Svensk Kärnbränslehantering AB.
- /20/ **Sandström R, 1999.** Extrapolation of creep strain data for pure copper, Journal of Testing and Evaluation, JTEVA, Vol. 27, No. 1, January 1999.
- /21/ **Andersson H C M, Seitisleam F, Sandström R, 2004.** Creep testing of thick wall copper electron beam and friction stir welds at 75, 125 and 175°C, Swedish Institute for Metals Research, IM-2004-110, (also SKB TR-05-08, Svensk Kärnbränslehantering AB).
- /22/ **Andersson H C M, Seitisleam F, Sandström R, 2004.** Creep testing of thick-wall copper electron beam and friction stir welds, MRS Spring Meeting, San Francisco, 12–16 April, Mat. Res. Soc. Symp. Proc. Vol. 824, pp 51–56.
- /23/ **Andersson H C M, 2005.** Creep crack propagation in pure copper at 75°C, Swerea KIMAB Technical Report KIMAB-2008-128 (renumbered in 2008).
- /24/ **Andersson H C M, Seitisleam F, Sandström R, 2007.** Creep testing and creep loading experiments on friction stir welds in copper at 75°C, SKB TR-07-08, Svensk Kärnbränslehantering AB.
- /25/ **Andersson-Östling H C M, Seitisleam F, Sandström R, 2010.** Influence of phosphorous, sulphur and grain size on creep in pure copper, Doctoral Thesis, Kungliga Tekniska Högskolan, Stockholm.
- /26/ **Sandström R, Wu R, 2007.** Origin of the extra low creep ductility of copper without phosphorus, SKB TR-07-02, Svensk Kärnbränslehantering AB.
- /27/ **Sandström R, Andersson H C M, 2008.** The effect of phosphorus on creep in copper, Journal of Nuclear Materials, 372, 66–75.
- /28/ **Sandström R, Andersson H C M, 2008.** Creep in phosphorus alloyed copper during power-law breakdown, Journal of Nuclear Materials 372, 76–88.
- /29/ **Sandström R, Andersson H C M, 2007.** Creep during power-law breakdown in phosphorus alloyed copper, CREEP8 Conference, San Antonio, Texas, USA, July 22–26, 2007.
- /30/ **Jin L-Z, Sandström R, 2008.** Creep of copper canisters in power-law breakdown, Computational Materials Science, 43, 403–416.
- /31/ **Jin L-Z, Sandström R, 2009.** Non-stationary creep simulation with a modified Armstrong-Frederick relation applied to copper canisters, Computational Materials Science, 42, 339–346.
- /32/ **Jin L-Z, Sandström R, 2009.** Modified Armstrong-Frederick relation for handling back stresses in FEM computations, Proceedings 2nd international ECCO conference. Creep & fracture in high temperature components – design & life assessment issues, Dübendorf, Switzerland, eds I. A. Shibli, S.R: Holdworth, pp. 836–847.
- /33/ **Sandström R, Hallgren J, Burman G, 2009.** Stress strain flow curves for Cu-OFP, SKB R-09-14, Svensk Kärnbränslehantering AB.
- /34/ **Martinsson Å, 2009.** Effect of cold work on creep properties of oxygen-free copper, Swerea KIMAB Technical Report KIMAB-2009-109.
- /35/ **Martinsson Å, Andersson-Östling H C M, 2009.** Effect of cold work on creep properties of oxygen-free copper, S:t Petersburg.
- /36/ **Wu R, Jin L-Z, Sandström R, 2009.** Influence of multiaxial stresses on creep properties of phosphorus alloyed oxygen free copper, Proceedings of PVP2009, 2009 ASME Pressure Vessels and Piping Division Conference, July 26–30, 2009, Prague, Czech Republic.
- /37/ **Raj S V, Langdon T G, 1989.** Creep behaviour of copper at intermediate temperatures-I. Mechanical characteristics, Acta Metall. 37, 843.
- /38/ **Ho E T C, 2000.** A study of creep behaviour of oxygen-free phosphorus-doped copper under low-temperature and low-stress test conditions, Ontario Power Technologies report, Unpublished data.

- /39/ **Ho E T C , 2002.** Creep behaviour of oxygen-free phosphorus-doped copper at 95°C in a standard Canadian shield saline solution environment, Ontario Power Technologies report, Unpublished data.
- /40/ **European creep collaborative committee, 2001.** ECCC recommendations, volume 2 part IIb (issue 2), Brite-Euram thematic network BET2-0509 Weld-Creep.
- /41/ **Auerkari P, Rantala J, Salonen J, Laukkanen A, Holmström S, Kinnunen T, 2009.** Effect of defects on low temperature creep of OFP copper, ECCC Creep Conference, pp 287–297, 21–23 April 2009, Zürich, Switzerland.
- /42/ **Savolainen K, Saukkonen, Mononen J, Hänninen H, 2008.** Entrapped oxide particles in friction stir welds of copper, Material Flow during Friction Stir Welding of Copper, 7th Int. Symp. on Friction Stir Welding, Awaji Island, Japan.
- /43/ **Furuta T, Kawasaki S, Nagasaki R, 1973.** The effect of cold working on creep rupture properties for helium-injected austenitic stainless steel, Journal of Nuclear Materials, Volume 47, Issue 1, May 1973, Pages 65–71.
- /44/ **Ajaja O, Ardell A J, 1977.** Microstructural parameters and steady-state creep, Scripta Metallurgica, Volume 11, Issue 12, December 1977, Pages 1089–1093.
- /45/ **Adelus J L, Guttman V, Scott V.D, 1980.** Effect of prior cold working on the creep of 314 alloy steel, Materials Science and Engineering, Volume 44, Issue 2, July 1980, Pages 195–204.
- /46/ **Pilloni G, Quadrini E, Spigarelli S, 2000.** Interpretation of the role of forest dislocations and precipitates in high-temperature creep in a Nb-stabilised austenitic stainless steel, Materials Science and Engineering A, Volume 279, Issues 1–2, 29 February 2000, Pages 52–60.
- /47/ **Hökmark H, Fälth B, 2003.** Thermal dimensioning of the deep repository, SKB TR-03-09, Svensk Kärnbränslehantering AB.
- /48/ **Yao X X, Sandström R, 2000.** Study of creep behaviour in P-doped copper with slow strain rate tensile tests, SKB TR-00-09, Svensk Kärnbränslehantering AB.
- /49/ **Roberts W, Bergström Y, 1973.** The stress-strain behaviour of single crystals and polycrystals of face-centered cubic metals—a new dislocation treatment, Acta Metallurgica, 21, 457–469.
- /50/ **Kocks U F, Mecking H, 2003.** Physics and phenomenology of strain hardening: the FCC case, Progress in Materials Science, 48, 171–273.
- /51/ **Roters F, Raabe D, Gottstein G, 2000.** Work hardening in heterogeneous alloys – a microstructural approach based on three internal state variables, Acta mater. 48, 4181–4189.
- /52/ **Korzhavyi P A, Abrikosov I A, Johansson B, 1999.** Theoretical investigation of sulphur solubility in pure copper and dilute copper-based alloys, Acta mater. Vol. 47, No. 5, pp. 1417–1424.
- /53/ **Wu R, Sandström R, 1996.** Strain dependence of creep cavity nucleation in low alloy and 12% Cr steels, Mater. Science Techn. 12, pp 405–415.
- /54/ **Needham N G, Wheatley J E, Greenwood G W, 1975.** The creep fracture of copper and magnesium, Acta Metallurgica Vol. 23, pp 23–27.
- /55/ **Davanas K, Solomon A A, 1990.** Theory of intergranular creep cavity nucleation, growth and interaction, Acta metall. mater. Vol. 38, No. 10, pp. 1905–1916.
- /56/ **Raj R, 1978.** Intergranular fracture in bicrystals, Acta metall. 26, pp 341–349.
- /57/ **Magnusson H, Sandström R, 2009.** Growth of Creep Cavities in 12% Cr Steels, ECCC Creep Conference, 21–23 April 2009, Zurich.
- /58/ **Beere W, 1981.** Cavities and Cracks in Creep and Fatigue, edited by J. Gittus, Applied Science, New York.
- /59/ **Hirth J P, Lothe J, 1968.** Theory of Dislocations, McGraw-Hill, New York.
- /60/ **Kocks U F, Argon A S, Ashby M F, 1975.** Thermodynamics and kinetics of slip, Prog. Mater. Sci. 19, 1.

- /61/ **King H W, 1966.** Quantitative size-factors for metallic solid solutions, *Journal of materials science* 1, pp. 79–90.
- /62/ **Wu R, Seitisleam F, Sandström R, 2004.** Influence of extra coarse grain size on the creep properties of 9% CrMoV (P91) steel weldment, *Journal of Engineering Materials and Technology*, 126, 87–94.
- /63/ **Armstrong P J, Frederick C O, 1966.** A mathematical representation of the multiaxial Bauschinger effect, C.E.G.B. Report RD/B/N 731.
- /64/ **Wu R, Jin L-Z, Sandström R, 2009.** Influence of multiaxial stresses on creep properties of phosphorus alloyed oxygen free copper, *Proceedings of PVP2009, 2009 ASME Pressure Vessels and Piping Division Conference*, July 26–30, Prague, Czech Republic.
- /65/ **Crisfield M A, 1997.** *Non-linear finite element analysis of solids and structures, volume 2, Advanced Topics*, John Wiley & Sons Ltd., England.
- /66/ **Hernelind J, 2009.** Modelling and analysis of canister and buffer for earthquake induced rock and glacial load. SKB TR-10-34, Svensk Kärnbränslehantering AB.

Unpublished documents

SKBdoc id	Title	Issuer, year
1205273 ver 2.0	Intryck i koppar	SKB, 2009
1206894 ver 1.0	Uneven swelling pressure on the canister. Simplified load cases derived from uneven wetting, rock contours and buffer density distribution.	SKB, 2009

